ABSTRACT

Title of dissertation: SIFTING FOR SAPPHIRES IN THE TRANSIENT SKY: THE SEARCH FOR TIDAL DISRUPTION EVENTS IN THE OPTICAL TIME DOMAIN

TZU-YU HUNG
Doctor of Philosophy, 2018

Dissertation directed by: Professor Suvi Gezari
Department of Astronomy

Tidal disruption events (TDEs) refer to the scenario where a star passes within the tidal disruption sphere of a supermassive black hole (SMBH) and becomes torn apart by tidal stresses. In the classical picture, a thermal flare is expected once the bound stellar debris circularize to form an accretion disk that feeds onto the black hole. This flare of radiation provides a unique window to study the demographics of black holes within distant and quiescent galaxies that cannot be probed by other means. In addition, TDEs serve as a powerful probe of the accretion process, where the mass fallback rate can be super-Eddington for $M_{\rm BH} <$ a few $\times\ 10^7\ M_\odot$. In recent years, ground-based wide-field optical surveys have successfully detected about a dozen of TDEs. Yet our knowledge of these events is still limited due to their low occurrence rate ($\approx 10^{-4}$–10^{-5} gal^{-1} yr^{-1}).

In the first part of this thesis, we present results from a systematic selection of TDEs in the Intermediate Palomar Transient Factory (iPTF). Our selection targets

typical optically-selected TDEs: blue transients ($g - r < 0$ mag) residing in the center of resolved red galaxies that are absent of previous nuclear activity. Our photometric selection has led to discoveries of two TDEs in ∼4 months, iPTF16axa and iPTF16fnl, in 2016. With the most stringent criteria, we significantly reduced the contamination rate from SN Ia and AGN from 200:1 to 4.5:1. We derived a TDE rate of $1.7^{+2.9}_{-1.3} \times 10^{-4}$ gal^{-1} yr^{-1} and forecast a discovery rate of 32^{+41}_{-25} TDEs per year for ZTF.

The second part of this thesis features a detailed analysis of the photometric and spectroscopic observations on iPTF16axa. We compared iPTF16axa with 11 other TDEs in the literature with well-sampled optical light curves. We concluded that most of these TDE candidates have peak luminosities confined between log(L [erg s^{-1}]) = 43.4–44.4, with constant temperatures of a few $\times$ 10^4 K during their power-law declines, implying blackbody radii on the order of ten times the tidal disruption radius, that decrease monotonically with time. For TDE candidates with hydrogen and helium emission, the high helium-to-hydrogen ratios suggest that the emission arises from high-density gas, where nebular arguments break down.

In the last part of this thesis, I present statistical analyses on the Zwicky Transient Facility (ZTF) data and comments on the TDE rate from the first few months of the survey. Finally, I close this chapter with an analysis on the optical spectra of the first ZTF TDE – AT2018zr.

Sifting for Sapphires in the Transient Sky: The Search for Tidal Disruption Events in the Optical Time Domain

by

Tzu-Yu Hung

Dissertation submitted to the Faculty of the Graduate School of the
University of Maryland, College Park
in partial fulfillment of the requirements for the degree of
Doctor of Philosophy
2018

Advisory Committee:
Professor Suvi Gezari, Chair/Advisor
Dr. S. Bradley Cenko
Professor M. Coleman Miller
Dr. Bradley M. Peterson
Professor Abolhassan Jawahery

Preface

Chapter 2 was submitted to the *AstrophysicalJournal* as "Sifting for Sapphires: Systematic Selection of Tidal Disruption Events in iPTF" (Hung et al. 2017b). It is expected to be accepted for publication after minor revisions. Chapter 3 has been published in the *AstrophysicalJournal* as "Revisiting Optical Tidal Disruption Events with iPTF16axa" (Hung et al. 2017a). It is reproduced here with only changes to formatting and layout. Portions of Chapter 4 are intended for submission to peer-review journals this year.

Dedication

To my parents.

Acknowledgments

This thesis would not have been possible without the support from the people around me. I am very grateful to my advisor Suvi Gezari for her advice about research. Coming from an engineering background, I was back to square one when started graduate school. Suvi always encourages me to try out new ideas and would not mind to explain very basic things to me. Suvi has a cheerful personality. At times, her passion about research reminds me all the fun and excitement of Astronomy that led me to the point I am now. I would also like to thank Brad Cenko for his patience and kindness. Brad knows everyone in the time domain field and loves to introduce people to each other. Your friendly action has saved me from feeling awkward in many meetings.

Being in a big collaboration, I am very fortunate to have met so many people outside the University of Maryland. I owe thanks to many people at Caltech who helped me in the summer of 2017. I would like to thank Shri Kulkarni for his mentorship about science and life and his wise words. I thank Mansi Kasliwal for reaching out to me when I needed career advice. I thank Lin Yan and Nadia Blagorodnova for their hospitality every time I visit Caltech.

I have enjoyed my time at the UMD department of Astronomy and I owe that to the people here. I have to thank my classmates Myra, Blake, Corbin for choosing to go through the same path with me. I thank Alex and Anna for being great friends and great travel buddies. I thank Dana and Jeff for always hosting great parties. I would also like to thank Arnab and Drew for the small chats that help light up the

mood.

I would like to thank my parents for being there for me. You have been very supportive even when my decision is not a usual one. Dad, you are the reason I became interested in Astronomy. I thank my sister for being my partner in crime and providing me with laughter at all times. I want to thank my grandmother for loving me unconditionally. Thank you for standing by my side when no one else would. You did not treat me differently even when I was in the worst shape of my life.

Finally, I owe my deepest gratitude to my husband Qian. You taught me to focus only on the things that matter. Thank you for always pushing me to do my best. You have saved me from getting into troubles for countless times. It is wonderful to have you to share my laughter and tears with. Also, You cook perfect steaks. I know I can never reach this point without you.

Table of Contents

List of Tables

List of Figures

List of Abbreviations

AGN	Active Galactic Nucleus
ASASSN	All-Sky Automated Survey for Supernovae
CV	Cataclysmic Variable
DCT	Discovery Channel Telescope
FOV	Field of View
FWHM	Full Width at Half Maximum
GALEX	Galaxy Evolution Explorer
iPTF	intermediate Palomar Transient Factory
LSST	Large Synoptic Survey Telescope
$M_{\rm BH}$	Black hole mass
MSIP	Mid-Scale Innovations Program
PS1	Pan-STARRS1
PSF	Point Spread Function
QSO	Quasar
ROSAT	the ROentgen SATellite
SDSS	Sloan Digital Sky Survey
SED	Spectral energy distribution
SEDm	SED machine
SFR	Star Formation Rate
SMBH	Supermassive Black Hole
SN	Supernova
SN Ia	Type Ia Supernova
TDE	Tidal Disruption Event
UV	Ultraviolet
UVOT	Ultraviolet-Optical Telescope
XRT	X-ray Telescope
ZTF	Zwicky Transient Facility

Chapter 1: Introduction

Tidal disruption events (TDEs) are transient phenomena that occur when a star is torn apart under the tidal stress of a black hole. In this thesis, I focus on the TDEs discovered in optical time domain surveys, whose emission is dominated by a thermal spectrum. A brief history of TDEs and the current status of the field are outlined in this chapter.

1.1 Short History

The tidal disruption of stars is an inevitable consequence of supermassive black holes (SMBHs) being at the hearts of most, if not all, bulge galaxies. However, it was not until the mid 70s that the theoretical foundation of TDEs had been laid out (Hills 1975; Rees 1988; Phinney 1989; Evans & Kochanek 1989). In the following section, I will summarize the details in the early theoretical development of TDEs. As it will appear more clear, observations of TDEs have two unique applications in galaxy evolution: probing distant and inactive SMBHs and finding lower mass black holes ($M_{\rm BH} \lesssim 10^8 M_\odot$).

1.2 Theory

In the classical framework of a TDE outlined by Rees (1988), a star of mass $M_\star$ and $R_\star$ on a parabolic orbit can be tidally disrupted by a black hole of mass $M_{\rm BH}$ when its pericenter distance (R_p) is less than the tidal radius R_T

$$\begin{aligned} R_p < R_T &= R_\star (M_{\rm BH}/M_\star)^{1/3} \\ &\approx 47.1 M_6^{-2/3} \frac{R_\star}{R_\odot} \left(\frac{M_\star}{M_\odot}\right)^{-1/3} r_g, \end{aligned} \tag{1.1}$$

where r_g is the gravitational radius defined as $GM_{\rm BH}/c^2$. We choose $M_{\rm BH} = 10^6 M_{\rm BH}$ as the fiducial black hole mass, where M_6 denotes $M_{\rm BH}/10^6\ M_\odot$.

Since the event horizon grows linearly with the black hole mass ($r_H = (1 + \sqrt{1-\hat{a}^2}) r_g$, where $\hat{a}$=0 for a nonrotating black hole and $\hat{a}$=1 for a maximally rotating hole), it will eventually overfill the tidal radius at $M_{\rm BH} \gtrsim 10^8\ M_\odot$ for a solar mass star. In such a case, the star will be directly captured instead of being disrupted by the black hole. For a spinning black hole, this upper limit on $M_{\rm BH}$ of a black hole capable of tidally disrupting a star is higher (up to $\sim 7{\times}10^8\ M_\odot$ depending on how fast the hole rotates).

The energy required for the disruption of a star is supplied by the orbital energy. Before disruption, the orbital energy of a star on a parabolic orbit was zero. However, the specific energy (energy per unit mass) of each fluid element is determined by its distance to the black hole. The change in black hole potential across a stellar radius causes a spread $\Delta\epsilon$ in the specific energy ϵ of the gas

$$\Delta\epsilon \simeq \frac{GM_{\rm BH}}{R_p^2} R_\star. \tag{1.2}$$

This spread can easily exceed the binding energy of the star, $\frac{GM_\star}{R_\star}$, by a factor of $\beta^2(M_{\rm BH}/M_\star)^{1/3}$, where β is the penetration factor defined as

$$\beta \equiv \frac{R_T}{R_p}. \tag{1.3}$$

In Rees (1988), the specific energy is a flat energy distribution centered around zero from $-\Delta\epsilon$ to $+\Delta\epsilon$. The implication of this energy spread is that half of the mass of the disrupted stellar debris will be ejected from the system ($\epsilon >0$) while the other half remains bound to the black hole ($\epsilon <0$), as shown in Figure 1.1.

The bound debris then settle in a highly eccentric elliptical orbits. For the most bound orbit, the semimajor axis (a_{mb}) and the eccentricity (e_{mb}) are

$$a_{mb} = R_T^2/2R_\star \approx 3.5\times10^{14}\frac{R_\star}{R_\odot}\left(\frac{M_6}{M_\star/M_\odot}\right)^{2/3}\ {\rm cm} \tag{1.4}$$

and

$$e_{mb} = 1 - R_p/a_{mb} \approx 1 - \frac{2}{\beta}\left(\frac{M_\star}{M_{\rm BH}}\right)^{1/3} \tag{1.5}$$

The most bound material returns to the pericenter after a time

$$\begin{aligned} t_{min} &= \frac{2\pi G M_{\rm BH}}{(2\Delta\epsilon)^{3/2}} \\ &= 41 M_6^{1/2}\beta^{-3}\left(\frac{M_\star}{M_\odot}\right)^{-1}\left(\frac{R_\star}{R_\odot}\right)^{3/2}\ {\rm days}. \end{aligned} \tag{1.6}$$

Following the assumption of a flat energy distribution ($dm/d\epsilon$ = constant), the debris continue to return at a mass fallback rate (Phinney 1989)

$$\begin{aligned} \dot{M}_{fb} &= \frac{dm}{d\epsilon}\frac{d\epsilon}{dt} \\ &= \frac{dm}{d\epsilon}\frac{1}{3}(2\pi G M_{\rm BH})^{2/3}t^{-5/3}. \end{aligned} \tag{1.7}$$

The $t^{-5/3}$ decay has been considered a signature of TDEs. TDEs are expected to produce luminous flares since its peak fallback rate $\dot{M}_{peak} = \frac{1}{3}M_\star/t_{min}$ is on the

order of ∼100 times the Eddington accretion rate

$$\dot{M}_{Edd} = 1.3 \times 10^{24} M_6 \left(\frac{\eta}{0.1}\right)^{-1} \text{g s}^{-1}. \tag{1.8}$$

The Eddington ratio $\dot{M}_p/\dot{M}_{Edd}$, however, drops quickly with black hole mass ($\propto M_{\rm BH}^{-3/2}$). As a result, the fallback rate will never exceed the Eddington rate when $M_{\rm BH} \gtrsim 2{\times}10^7\ M_\odot$.

In the process of circularization, the debris stream must lose its orbital energy by at least a factor of $(M_{\rm BH}/M_\star)^{1/3}$ to join a disk at r$\sim R_p$. Rees (1988) argued that stream intersection near R_p from relativistic apsidal precession could result in strong shocks that dissipiate a large fraction of the streams' orbital energy. Assuming a large fraction of the debris can be circularized in a time of (2-10)$\times t_{min}$ and that the dynamic time at R_T is small relative to the mass return time, rapid onset of accretion in the disk produces a luminous flare. Suppose the radiation is a blackbody at Eddington luminosity emitted from a sphere of radius R_T, the effective temperature can be expressed as

$$\begin{aligned} T_{\rm eff} &\approx \left(\frac{L_{Edd}}{4\pi R_T^2 \sigma}\right)^{1/4} \\ &\approx 2.5 \times 10^5 M_6^{1/12} \left(\frac{R_\star}{R_\odot}\right)^{-1/2} \left(\frac{M_\star}{M_\odot}\right)^{-1/6} \text{K}, \end{aligned} \tag{1.9}$$

or from the inner most stable circular orbit for a non-spinning black hole ($R_{\rm ISCO} = 6\ r_g$)

$$\begin{aligned} T_{\rm eff} \approx \left(\frac{L_{Edd}}{4\pi (6r_g)^2 \sigma}\right)^{1/4} &\approx 6.5 \times 10^5 M_6^{-1/4}\ \text{K} \\ &\approx 0.06 M_6^{-1/4}\ \text{keV}. \end{aligned} \tag{1.10}$$

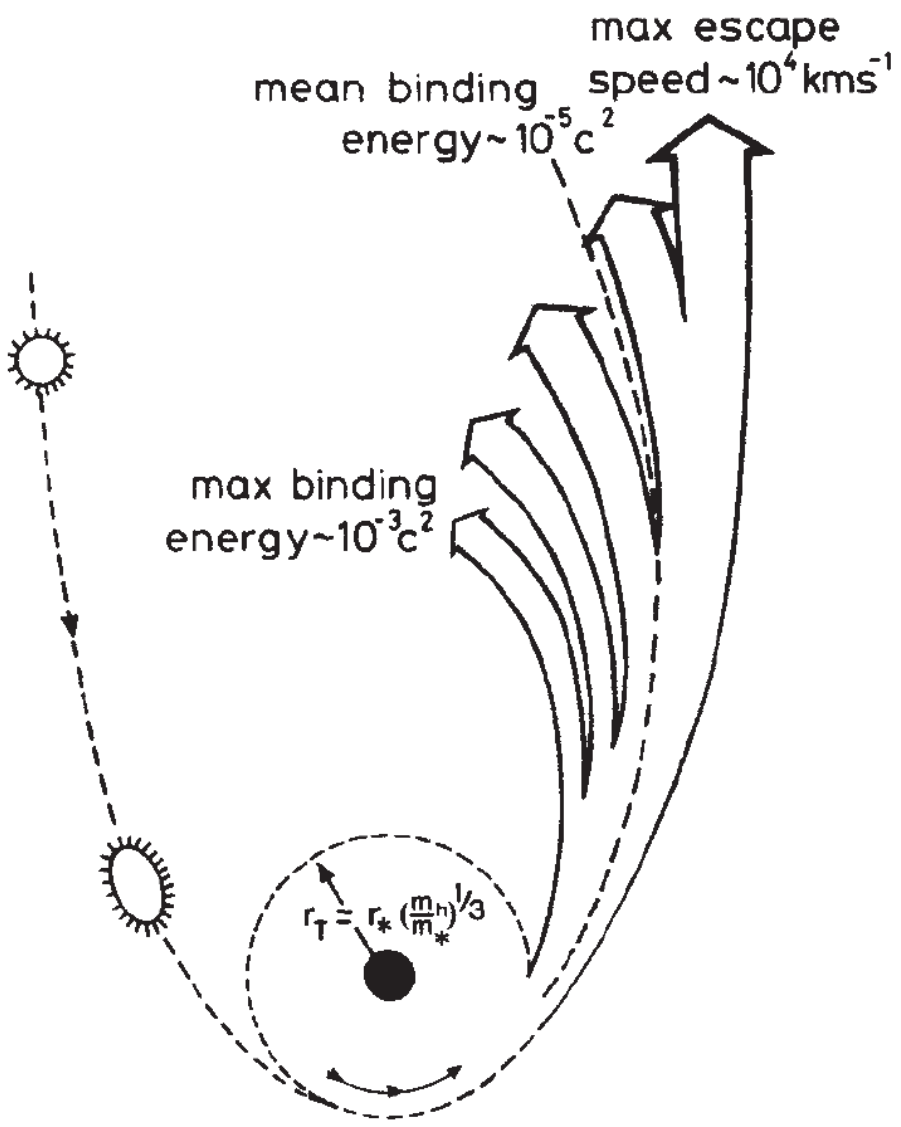

Figure 1.1: Schematic of a tidal disruption event illustrated in Rees (1988). Stars that approach a black hole within a distance R_T will be disrupted by tidal stresses. The energy spread within the star causes half of the mass to escape the gravitational potential of the black hole while the other half remains bound to the black hole. The maximal escape velocity of the stellar debris can reach ≈ 0.1c.

1.3 Two-body relaxation

The collective behavior of stars in the vicinity of a black hole can be described by a distribution function over a six dimensional phase space $f(\vec{x}, \vec{v})$. This distribution function is delepted within the loss cone, which is defined in terms of specific angular momentum

$$J < J_{\rm lc} \approx (2GM_{\rm BH}R_T)^{1/2}. \tag{1.11}$$

In a collisionless stellar system, the loss cone would be emptied in one orbital period. However, in the regime of high stellar density, the loss cone can be replenished with fresh stars by two-body relaxation (Magorrian & Tremaine 1999; Wang & Merritt 2004). This relaxational repopulation occurs in two regimes: the diffusive regime and the "pinhole" regime, which can be differentiated with the parameter $q(\epsilon)$

$$q(\epsilon) = \frac{P(\epsilon)\bar{\mu}(\epsilon)}{R_{lc}}, \tag{1.12}$$

where $P(\epsilon)$ is the orbital period of energy ϵ, $\bar{\mu}$ is the orbita-averaged diffusion coefficient, and $R_{lc} = J_{lc}^2/J_c(\epsilon)^2$ with J_c being the angular momentum of a circular orbit. When $q \ll 1$, the stars diffuse into the loss cone over many orbits. TDEs produced in this diffusion regime have $\beta \approx 1$. TDEs produced in the pinhole regime, where loss cone is replenished faster than depleted ($q \gg 1$), can have a large range of β value (Stone & Metzger 2016).

TDE rates from two-body relaxation have been estimated in realistic galaxies

with $M_{\rm BH}$ and stellar mass density profiles measured from observations. Typically, TDEs occur on a frequency of 10^{-4} – 10^{-5} per year (Magorrian & Tremaine 1999; Wang & Merritt 2004). Furthermore, TDE rate is dominated by low mass galaxies with a cuspy stellar density profile and the rate increases with decreasing $M_{\rm BH}$.

1.4 Observations

In the classical picture where a tidal disruption flare is mainly powered by accretion, its radiation can be characterized by a thermal spectrum peaking in the soft X-ray. The first few TDE candidates discovered in the form of soft X-ray outbursts were observed by the ROSAT all-sky survey. These TDE candidates were detected in NGC5905 (Bade et al. 1996; Komossa & Bade 1999), IC3599 (Brandt et al. 1995; Grupe et al. 1995), RX J1242-1119 (Komossa & Greiner 1999), and RX J1420+5334 (Greiner et al. 2000). These ROSAT events are hosted by optically inactive galaxies with black holes in the mass range of 10^6–10^8 $M_\odot$. At maximum light, their spectra are characterized by a soft X-ray spectrum ($kT < 0.1$keV) with a peak luminosity of a few 10^{44} erg s^{-1}. These flares usually decline on a timescale of months to years roughly following the mass fallback rate t$^{-5/3}$ (see Komossa 2015, for a detailed review).

The capability to discover as well as follow up TDEs have significantly improved with the successful launch of several space observatories, including Chandra, XMM-Newton, and Swift. In particular, serendipitous discoveries of TDEs based on comparison with ROSAT were made with the XMM-Newton slew survey (Esquej

et al. 2007, 2008; Saxton et al. 2012). By far, the discovery of *Swift* J1644+57, a high energy jetted TDE, is second to none in its unique properties. This transient radiated γ-ray emission for days and X-ray emission brighter than 10^{45} erg s^{-1} for over a year (Burrows et al. 2011; Levan et al. 2011). A bright, variable radio synchrotron source was coincident with the nucleus of the host galaxy at z=0.353 (Zauderer et al. 2011). Given the peak luminosity of this source is at least by a factor of 100 above Eddington limit, the most favored explanation is the direct viewing into a relativistic jet (Bloom et al. 2011).

The study of TDEs has turned a new page with the advent of ground-based optical sky surveys. The wide FOV of optical surveys allows a sampling rate on the order of 100 times higher than X-ray surveys, which makes them more cost efficient in finding low space density transients like TDEs. The number of TDEs discovered from the low energy tail of their emission in various surveys (SDSS, PS1, PTF, and ASASSN...etc) has amounted to roughly a dozen since 2011 (e.g. van Velzen et al. 2011; Gezari et al. 2012; Arcavi et al. 2014; Holoien et al. 2014, 2016b; Hung et al. 2017a; Blagorodnova et al. 2017a; Wyrzykowski et al. 2016). In the section below, I will describe the ensemble properties of the optically selected TDEs and where they diverge.

1.5 Properties of Optically Detected TDEs

Here I use PS1-10jh (Gezari et al. 2012), a TDE with multi-band, well-sampled light curves (Figure 1.2), to describe the emission properties of optical TDEs. This

source was observed with GALEX NUV and Pan-STARRS1 *griz* filters. PS1-10jh is one of a handful TDEs that have a rising light curve with the peak resolved. The rise time to peak for PS1-10jh is ∼40 days, which is slow compared to supernovae (∼2 weeks). The decline of the UV and optical light curves are roughly consistent with the mass fallback rate $t^{-5/3}$.

The SEDs of PS1-10jh can be well-fitted by a blackbody with a constant temperature of 3×10^4 K over the timespan of a year. A constant blackbody temperature on the order of $\times10^4$ K has also been seen in ASASSN-14ae (Holoien et al. 2014), ASASSN-14li (Holoien et al. 2016b), iPTF16axa (Hung et al. 2017a), and iPTF16fnl (Blagorodnova et al. 2017b).

Although the optical spectra of these TDEs are dominated by a blue continuum, they appear to have a combination of helium and hydrogen emission lines that vary from source to source. A broad (10^4 km s^{-1}) HeIIλ4686 line is present in the optical spectrum of PS1-10jh while there is no trace of hydrogen. On the other hand, both Hα and HeIIλ4686 are seen in the optical spectra of ASASSN-14li and iPTF16axa. The luminosity and shape of these broad lines are also variable on the timescale of weeks (Figure 1.3).

1.5.1 Outstanding issues

The properties of optically bright TDEs are challenging to the classical picture. While the X-ray TDEs generally fit in the classical prediction of accretion-powered radiation, the optical emission expected from this model ($< 10^{41}$ erg s^{-1}) is at least

two orders of magnitude lower than the observed optical luminosity ($\sim 10^{43}$ erg s^{-1}). There also seems to be a dichotomy between the properties of X-ray and opticall selected TDEs. All of the optical TDEs, except ASASSN-14li (Holoien et al. 2016b) and ASASSN-15oi (Holoien et al. 2016a; Gezari et al. 2017a), shows little or no X-ray emission.

In addition, the temperature of optical TDEs are at least an order of magnitude lower than the effective temperature expected for the debris disk. This possibility has been addressed in Loeb & Ulmer (1997), where the presence of a gaseous envelope formed around the disk may reprocess the radiation with an effective temperature on the order of 10^4 K (Guillochon et al. 2014; Roth et al. 2016). This reprocessing layer may be formed from a radiatively driven wind (Miller 2015; Strubbe & Murray 2015) or the circularization of material at a radius $\gg R_T$. As pointed out by Shiokawa et al. (2015), shocks caused by stream intersection near the stellar pericenter and apocenter alone do not dissipate orbital energy efficiently enough to form a disk at $\sim R_T$. This delay in circularization may cause the luminosity and disk temperature to be lower than expected in the standard picture (Dai et al. 2015). It has also been suggested that the optical emission is produced by stream-stream collisions during the formation of the accretion disk (Piran et al. 2015; Shiokawa et al. 2015; Jiang et al. 2016).

The explanation for the perplexing hydrogen-free optical spectrum of PS1-10jh is still debated. Gezari et al. (2012) attributed the absence of hydrogen to the disruption of a He-rich stellar core, where chemical composition of the star imprints on the line ratio. After the disruption, the star's hydrogen envelope returns to pericenter

before the helium core and potentially results in a temporal evolution in the spectrum that transitions from hydrogen-dominated to helium-dominated (Law-Smith et al. 2017a). On the other hand, Roth et al. (2016) modeled the optical spectrum of TDEs by propagating the radiation generated by accretion through an extended, optically thick envelope formed from stellar debris. They demonstrated with radiative transfer calculations that optical depth effects are capable of suppressing the hydrogen line to a helium-to-hydrogen ratio of at least 5:1.

It is also unclear why the luminosities of these optical TDEs follow the power-law decline $t^{-5/3}$, which implies the direct translation between luminosity and the mass fallback rate $t^{-5/3}$. In particular, the $t^{-5/3}$ evolution should be true only after several months post disruption (Lodato et al. 2009). Besides, under the disk assumption, the optical and UV light curves should follow a flatter $t^{-5/12}$ light curve even if the bolometric light curve is evolving as $t^{-5/3}$ (Lodato & Rossi 2011).

1.6 Selection Strategies

The discovery rate of optical TDEs over the years has remained as low as $\sim$2 per year. Not only because they are rarer by occurence frequency, but also because they tend to be coincident with regions of high surface brightness, which are harder to recover by image differencing in transient surveys. van Velzen et al. (2011) and Arcavi et al. (2014) have successfully identified a number of TDEs by performing a systematic search in archival SDSS Stripe 82 and PTF data. The major problem to tackle in the search of TDEs in transient surveys is to get rid of the supernovae and

variable AGNs that outnumber TDEs by two orders of magnitude.

While these interlopers are easy to separate retrospectively, their light curves bear little distinction to that of TDEs when the transient is young. Anticipating the number of transients to scale up by order(s) of magnitude with the operation of next generation surveys, our selection strategies must be examined and honed to maximize early and complete TDE discoveries with limited spectropic follow-up resources. Only through the discovery and detailed observations of more TDEs will we be able to conduct a systematic study and understand the processes govering their emission. This knowledge is essential before we can utilize TDEs to infer the demographics of black holes in the context of galaxy evolution.

1.7 Scope of the Dissertation

This thesis sets out to search for TDEs in ground-based optical surveys by assuming a minimal number of properties to get rid of common interlopers: SNIa and AGNs. In Chapter 2, I present the details of the iPTF experiment with its implication for ZTF. Two TDEs were discovered by iPTF during this experiment: iPTF16axa and iPTF16fnl. In Chapter 3, I present a 3-months long photometric and spectroscopic observations of iPTF16axa and comparison with UV and optically discovered TDEs including iPTF16fnl. In Chapter 4, I examine the selection criteria for TDEs with ZTF data and present spectroscopic observations on the first ZTF TDE — AT2018zr.

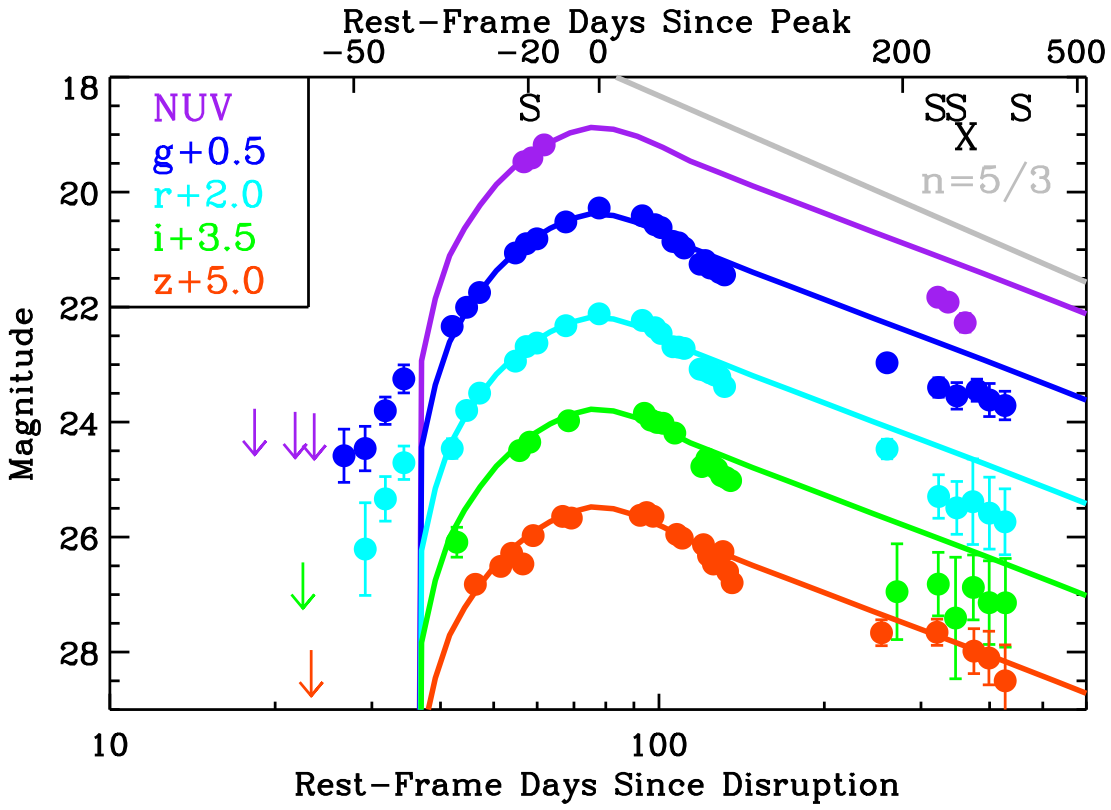

Figure 1.2: Light curves of PS1-10jh taken from Gezari et al. (2012).

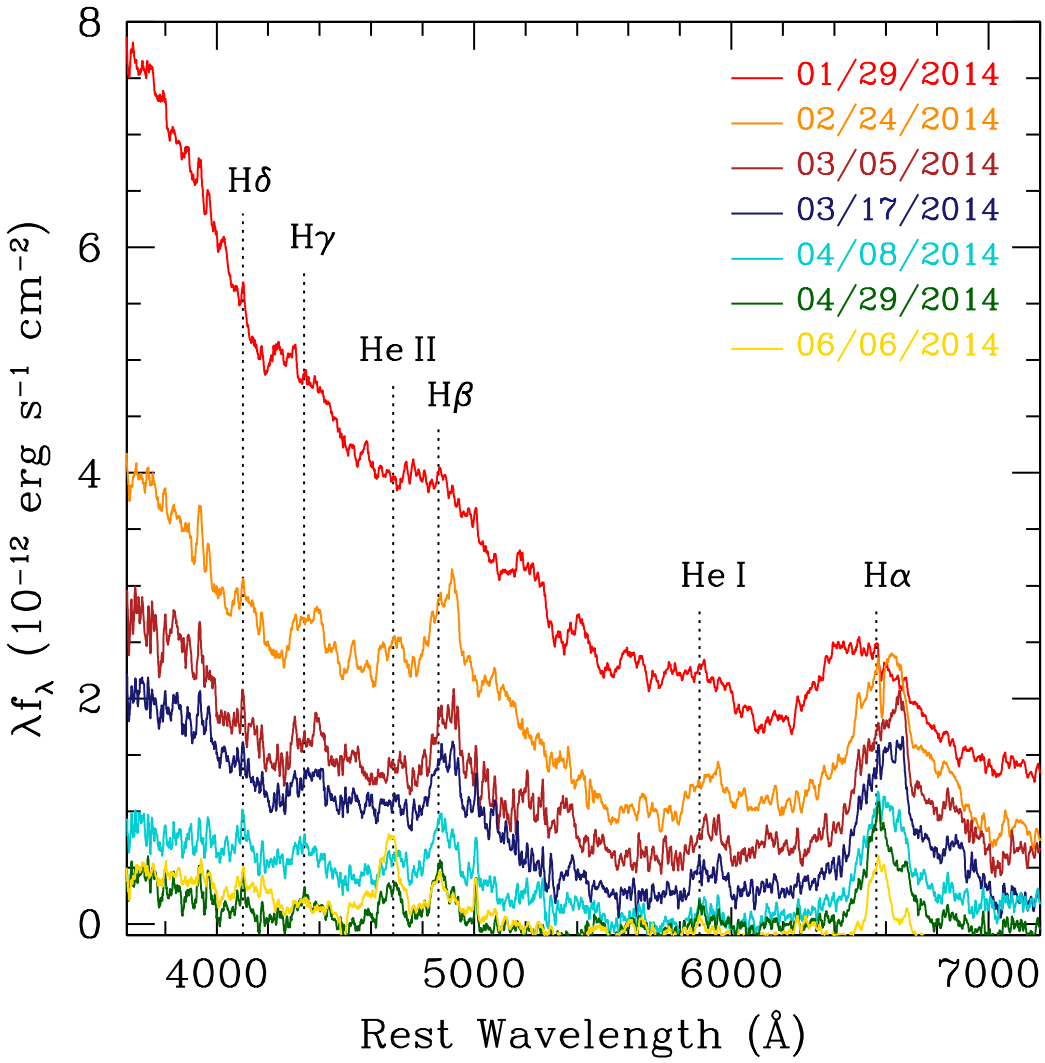

Figure 1.3: Evolution of the host subtracted spectra of ASASSN-14ae (Holoien et al. 2014). These spectra have properties typical of a TDE: a blue continuum with broad Balmer emission lines. The He IIλ4686 line was also detected in later epochs. The Hα line was blueshifted in the earliest epoch but grew narrow with time.

Chapter 2: Systematic Selection of Tidal Disruption Events in iPTF

2.1 Introduction

A stellar tidal disruption event (TDE) refers to the phenomenon of a star being scattered into the Roche radius of a supermassive black hole. For a star approaching on a parabolic orbit, about half of the stellar debris remains bound to the black hole after the disruption. In the paradigm of TDEs, the circularized bound debris will form an accretion disk and emit thermally (Rees 1988; Ulmer 1999) as it accretes onto the black hole. Alternatively, some studies have argued that the energy dissipated during the circularization process itself may be the main powering source of the emission in TDEs (Piran et al. 2015; Shiokawa et al. 2015; Dai et al. 2015; Bonnerot et al. 2017).

With the advent of a number of wide-field time domain surveys, about a dozen of convincing optically bright TDEs have been discovered. Unlike the first few TDEs discovered in the X-ray surveys (e.g. ROSAT) that have sparse light curves, the dense light curve sampling (once every few days) by ground-based optical surveys have enabled timely discoveries of these optical TDEs. The well-sampled optical light curves together with the rapid follow-up observations across the electromagnetic spectrum have provided rich data sets that allow us to study these TDEs in

more details. Although the selection criteria of these TDEs are different per survey, most of them follow a power-law decline that is loosely consistent with $t^{-5/3}$ (Phinney 1989) in their light curves while maintaining constant color over time. Most of these optically detected TDEs have a small spread in peak luminosity ($10^{43.4-44.4}$ erg s^{-1}) and blackbody temperature ((2–4)$\times10^4$ K; Hung et al. 2017a).

The first attempt of a systematic search of optically bright TDEs was made by van Velzen et al. (2011) using archival SDSS Stripe 82 imaging data, where they carefully examined the transients in the nuclei of galaxies (hereafter nuclear tranisents) and successfully recovered two TDE candidates. The search for TDEs usually excludes active host galaxies. The reason is because most AGNs exhibit variability and they outnumber TDEs by at least two orders of magnitude. Follow up on these sources is cost inefficient since a detailed spectroscopic study would be required to differentiate between AGN variability and TDE signatures. Nevertheless, there is no mechanism prohibiting stars from being disrupted by active black holes. For example, CSS100217 (Drake et al. 2011) and the recently reported PS16dtm (Blanchard et al. 2017) may have been TDEs occurring in narrow-line Seyfert 1 galaxies. Their properties, however, can be somewhat different from the TDEs observed in quiescent galaxies. For example, the light curve of PS16dtm exhibits a plateau instead of a monotonical decline following $t^{-5/3}$, even though its blackbody temperature remained constant at $T_{bb} \approx 1.7\times10^4$ K. The broad Hα component ($\approx$ 4000 km s^{-1}) in both CSS100217 and PS16dtm are considerably narrower than TDEs in inactive galaxies (10^4 km s^{-1}; Hung et al. 2017a) and they exclusively exhibit strong Fe II emission complexes. In addition, both events were radiating

near Eddington luminosity, which may suggest they are accreting more efficiently than TDEs in inactive galaxies (Blanchard et al. 2017).

Finding TDEs can also be complicated by the detection of transients in galaxy nuclei. Nuclear transient events suffer from stronger systematic and statistical errors when subtracted from the core of a galaxy. This poses a problem because large surveys like the intermediate Palomar Transient Factory (iPTF) rely on machine learning algorithms to remove image subtraction artifacts. Therefore, nuclear transients are more easily missed in this process of machine identification. Using the `realbogus` pipeline employed by iPTF as an example, the completeness drops from 1 to 0.5 when the flux contrast, defined as the ratio between the transient and the underlying host galaxy surface brightness, decreases from >10 times to 0.6 times (Frohmaier et al. 2017).

While the majority of the optically discovered TDEs reside in red early-type galaxies (see color definition in subsection 2.3.3, they seem to appear disproportionately more in a rare subset — quiescent Balmer-strong (E+A) galaxies — whose star formation history indicates they are in a post-starburst stage (Arcavi et al. 2014; French et al. 2016; Stone & van Velzen 2016). On a different study that employs a control group from SDSS, Law-Smith et al. (2017b) found that TDE host galaxies have a higher nuclear stellar density that is not owing to a recent major merger. Although the rare E+A galaxies are reported to be over-represented by at least 35 times in the current TDE sample (French et al. 2016; Graur et al. 2017), it is not known whether TDEs preferentially happen in E+A host galaxies or they just occur more frequently in centrally overdense galaxies.

The evergrowing number of TDEs discovered in optical surveys have gradually alleviated the tension between the observed and the predicted TDE rates, where the observed rate is typically an order of magnitude lower than the theoretical value predicted from two-body relaxation of stars in realistic galaxies ($\gtrsim 10^{-4}$ gal^{-1} yr^{-1}; Magorrian & Tremaine 1999; Wang & Merritt 2004; Stone & Metzger 2016). It is generally accepted that the lower observational TDE rate can be attributed to the fact that only the brighter TDEs in a steep TDE luminosity function are followed up in flux-limited surveys (van Velzen 2017). The fact that the luminosities of most optical TDEs seem to be drawn from a distribution with a small spread (Hung et al. 2017a) is also consistent with this scenario as long as the TDE luminosity is not a narrow step function. Since it is almost impossible to obtain a spectroscopically complete sample for most of the photometric surveys except for the All-Sky Automated Survey for Supernova (ASASSN has a flux limit of $r \sim 17$ mag; Shappee et al. 2014), at least some parts of this bias is introduced by human decisions on whether to trigger spectroscopic classification for a certain object. Therefore, a systematic strategy for selecting TDE candidates in real time for follow-up observations is critical for measuring TDE rates robustly.

Future surveys such as the Zwicky Transient Facility (ZTF) in 2018 and the Large Synoptic Survey Telescope (LSST) in the early 2020s are expected to boost the number of transients including TDEs by orders of magnitude. Maximizing the efficiency of follow-up resources will be even more challenging. In 2016, iPTF conducted its first experiment with simultaneous color observations. With a Cycle 12 *Swift* Key Project (PI Gezari) and observing time on several optical spectrographs,

we were able to perform a systematic follow-up of the TDE candidates that satisfy the selection of our nuclear transient pipeline. Two TDEs, iPTF16axa (z=0.108) and iPTF16fnl (z=0.016), were discovered during this 4-month experiment. In particular, iPTF16fnl is the faintest and fastest TDE discovered yet with a decay rate of $\sim$0.08 mag day^{-1} (Blagorodnova et al. 2017a).

In this paper, we report the performance of our pipeline optimized for TDEs by searching for blue ($g_{\rm PTF}$-$R_{\rm PTF}$<0 mag) nuclear flares within inactive red host galaxies and derive the TDE rate in iPTF. We first describe the design of the $g_{\rm PTF}$+$R_{\rm PTF}$ survey in section 2.2 and the selection of the nuclear candidates for *Swift* and spectroscopic follow-up in section 2.3. The photometric and spectroscopic observations are detailed in section 2.4. The classification of the final sample along with the results from *Swift* are presented in section 2.5. We discuss the performance of our pipeline and calculate the TDE rate in iPTF in section 2.6. We close with outlining the prospects of TDE discoveries with ZTF in section 2.6.

2.2 Rolling g+R Survey Design

iPTF conducted a rolling $g + R$ experiment from UT 2016 May 28 to 2016 Dec 7, observing a total of 81 nights. The Palomar 48-inch (P48) telescope uses SDSS-g' and Mould-R filters (hereafter $g_{\rm PTF}$ and $R_{\rm PTF}$) to carry out the survey. The experiment was suspended between 2016 Jun 16 and 2016 Aug 20 when the telescope time was entirely dedicated to the Hα survey and the Galactic plane survey.

The experiment took place in two stages. In the later period from 2016 Aug 20

to Nov 10, it was strictly controlled using a rolling strategy that was implemented as follows. We divided the 270 fields in total into three groups of 90 fields. At any given time, one of the groups was observed using a 1-day cadence, while the remaining 180 fields were observed using a 3-day cadence (i.e. 60 each night). As such, the total number of fields observed each night was 150. The 1-day cadence group was rotated so that every field would cycle between 1-day and 3-day cadences. This rotation took place regularly every lunation. Missed nights due to weather would become gaps in the light curve. To obtain the color, each field was observed with one $g_{\rm PTF}$ and one $R_{\rm PTF}$ filter typically separated by $\sim$0.5 hr. This experiment was called the *Color Me Intrigued* experiment when it was proposed (see Miller et al. 2017, for more details).

In the earlier stage from 2016 May 28 to Jun 16, fewer fields (58 fields on average) were targeted in a night. Each field was observed three times in $g_{\rm PTF}$ and $R_{\rm PTF}$ filters per night with two observations in the same filter. All of the targeted fields were scheduled to have a 4-day cadence. This change in cadence from the latter rolling cadence strategy did not significantly impact the outcome of our TDE search, since early science is not our main goal. Both TDEs iPTF16axa and iPTF16fnl were discovered in the low cadence fields.

We present the sky coverage of the $g + R$ experiment in Figure 2.1, with color bars indicating the number of exposures. The fields were selected to be overhead and have low airmass at the Palomar observatory during the observing period. We show the number of fields observed per night throughout the operation in the left panel of Figure 2.2. Given the 7.26 deg^2 field of view of the telescope, this corresponds

to an average areal coverage of 771 deg^2 per night. The right panel of Figure 2.2 shows the distribution of the longest baseline in each field excluding the summer gap. In Figure 2.3, the cadence distribution of the experiment is split by stages and by filters. In the early stage shown in the upper panel of Figure 2.3, most of the targeted fields were observed twice in $g_{\rm PTF}$ band per night and have a 4-day cadence. The later stage shown in the lower panel peaks at 1, 3, 6 days as intended by the experiment strategy. In summary, The experiment monitored 660 unique fields, which corresponds to a total of 4792 deg^2 of the sky.

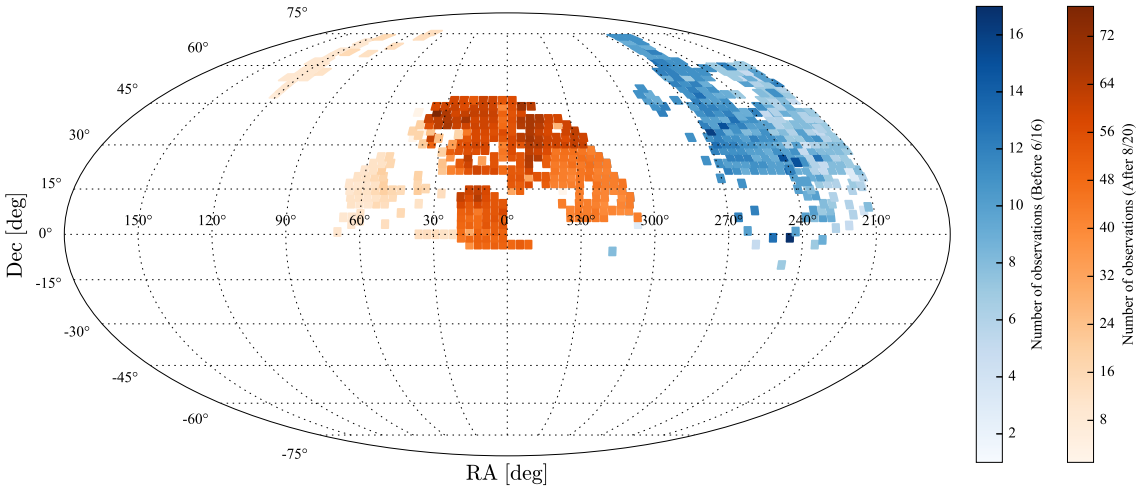

Figure 2.1: Sky coverage of the iPTF color experiment in Equatorial coordinates. The plot is broken down by the stage of the survey (before and after the summer hiatus). Each tile represents a unique pointing and the color reflects the number of observations in that field. Around 77% of the fields were also observed by SDSS.

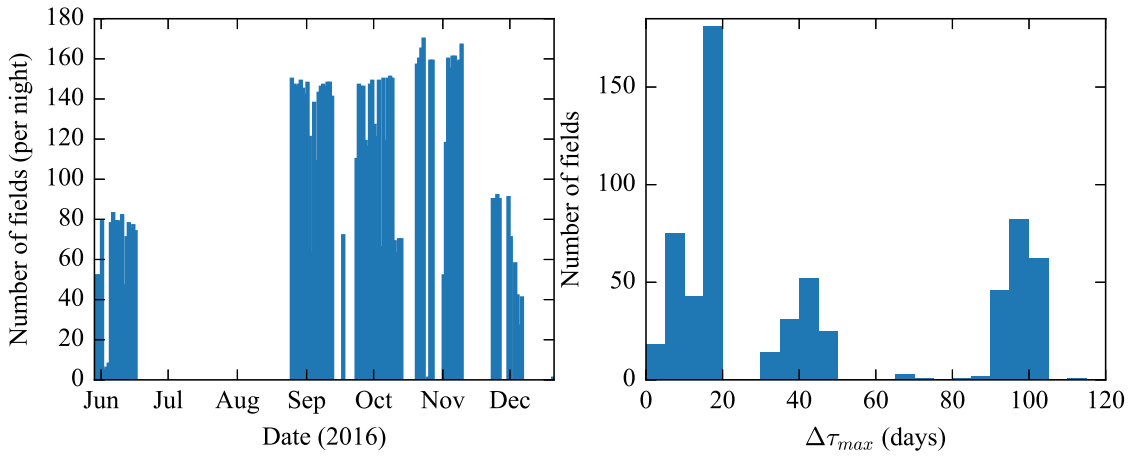

Figure 2.2: Left: Number of unique fields observed per night during the $g_{\rm PTF}$+$R_{\rm PTF}$ survey. Less fields were observed before Aug 2016 because each field were observed three times (usually 2 in $g_{\rm PTF}$ and 1 $R_{\rm PTF}$) per night instead of two. Right: Distribution of the longest baseline of each field in the $g_{\rm PTF}$+$R_{\rm PTF}$ experiment.

2.3 Selection of Candidates

During the $g_{\rm PTF}$+$R_{\rm PTF}$ experiment, the survey data was processed by the real-time image subtraction pipelines at the Infrared Processing and Analysis Center (IPAC) (Masci et al. 2017) and the National Energy Research Scientific Computing Center (NERSC) (Cao et al. 2016). We rely on machine learning classification – the probability based real-bogus (RB) score – to determine the likelihood of the detection being a real astrophysical transient as opposed to a false detection caused by image subtraction artifacts (Masci et al. 2017). Sources that have a S/N $>$ 5, a high RB score ($>$0.6), and at least 2 co-spatial detections within one night that are not cataloged as a variable star or a quasar are visually inspected by a human. Since

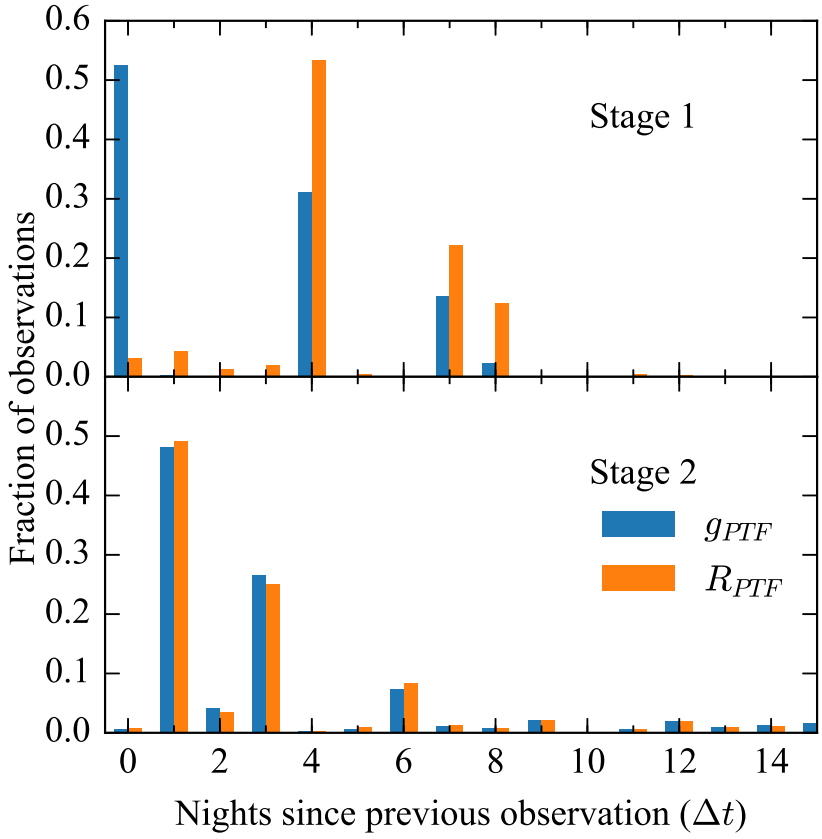

Figure 2.3: Cadence of the $g_{\rm PTF}$+$R_{\rm PTF}$ experiment in two stages. Figure shows the fraction of Δt between any two adjacent epochs for all the unique fields observed during this period in $g_{\rm PTF}$ (blue) and $R_{\rm PTF}$ (orange) bands. Intra-night observations (Δt=0) are dominated by the observations made before August (uppder panel), where two observations in the same filter were used to reject moving objects. The designed cadence of the later stage (bottom panel) is a rotating Δt of 1 and 3 days.The cadence for the later stage also clusters around 6 days due to weather loss.

bad subtractions normally have an irregular PSF, they can be readily recognized by eye. This process called scanning takes place on a daily basis. Only sources approved by the scanner were saved to the database for further study.

We show the stacked histogram of the number of transients saved during this experiment in Figure 2.4, where the nuclear and non-nuclear transients are shown in red and blue, respectively. A total of 1464 transients were saved in this period, averaging to 18 transients per night.

In transient surveys, the rate of SNe Ia (2.7×10^{-5} yr^{-1}Mpc^{-3}; Dilday et al. 2010) is on the order of 100 times higher than TDEs. Type 1 AGNs, which are known to be variable in the optical on timescales up to several years (Sesar et al. 2007), have a space density of $\approx 7\times10^{-6}$ Mpc^{-3} (Hao et al. 2005) that also outnumber TDEs by roughly two orders of magnitude. These two types of events are the main interlopers in the process of selecting TDE candidates. Because of their disproportionately higher occurrences, our selection criteria are focused on removing these interlopers, which we describe as follows.

The filtering has 7 steps (Figure 2.5). We first select sources that are astrometrically aligned with the center of a morphologically extended host galaxy. We make a further cut based on host galaxy color, selecting only nuclear transients in red host galaxies. We then remove sources that are known AGN by cross-matching with external catalogs or checking for flaring history in the historical PTF and iPTF database since 2009. We exclude sources with weak variability by applying a magnitude cut. Lastly, we remove red transient events and sources that are too dim for spectroscopic follow up. The composition of each intermediate sample is listed

in Table 2.1. The first column contains the description of each filtering procedure, which is detailed in the following sections.

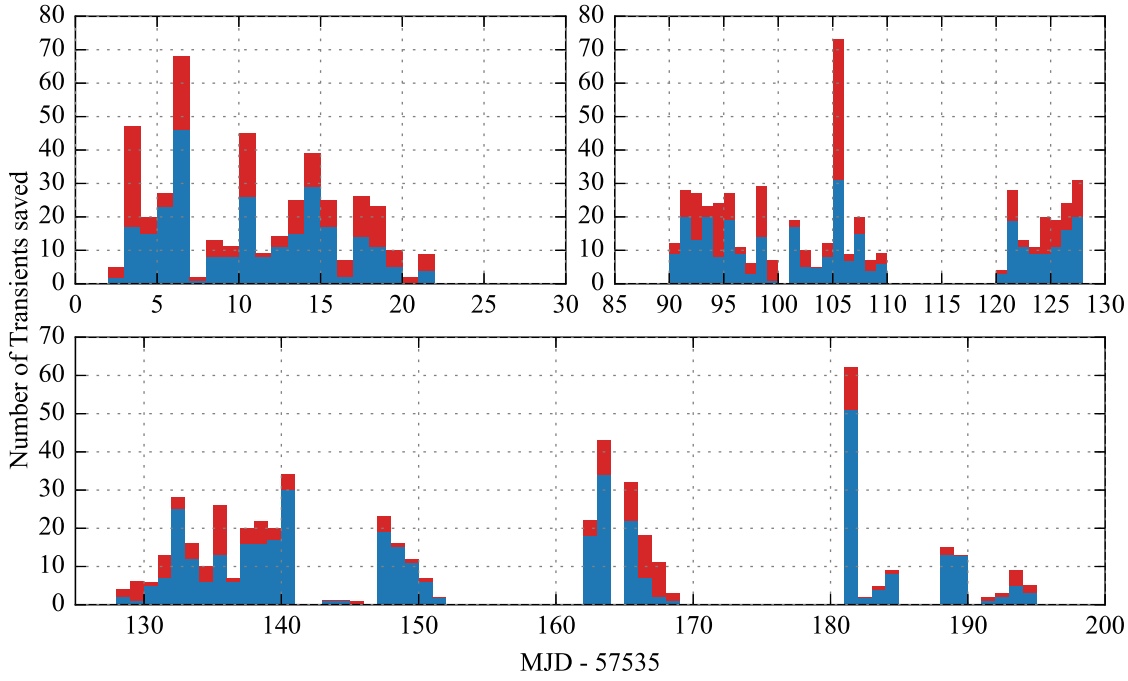

Figure 2.4: Total number of nuclear (red) on top of non-nuclear (blue) transient events saved during the period of iPTF $g_{\rm PTF}$+$R_{\rm PTF}$ experiment. Nuclear transients account for one-third of all the transients.

2.3.1 Selection of nuclear transients (step 1)

Tidal disruption of a star around a black hole occurs when the orbit of the star crosses the tidal disruption radius (R_T). For a non-spinning black hole, R_T is defined as

$$R_T = R_\star \left(\frac{M_{BH}}{M_\star}\right)^{1/3} = 0.47AU \left(\frac{R_\star}{R_\odot}\right) \left(\frac{M_{BH}}{10^6 M_\star}\right)^{1/3}, \qquad (2.1)$$

where $M_{\rm BH}$ is the black hole mass, $R_\star$ and $M_\star$ are the radius and mass of the

Figure 2.5: Flow diagram of the filtering process for TDE candidates. The composition of each intermediate step is listed in Table 2.1.

disrupted star, respectively. Since a TDE happens near the black hole, we limit our search to transients that reside in the center of a host galaxy. This tidal disruption radius corresponds to an angular separation on the nano-arcsecond scale at z=0.1 that cannot be resolved by any instrument.

We define a transient as nuclear if the separation of the transient and the centroid of the galaxy is less than 0.8″. This radial cut was empirically determined to include 80% of the PTF transients in the database associated with known AGNs (Figure 2.6). This offset distance is measured relative to the coordinates of the host centroid as output by `SExtractor` (Cao et al. 2016). While the mean position of the offset (relative right ascension $\Delta\alpha$ and declination $\Delta\delta$) over all detections should be zero, the offset distance between the transient and the host $x \approx\sqrt{\Delta\alpha^2 + \Delta\delta^2}$, should be non-zero (Figure 2.6). The offset distance distribution can provide clues to the distribution of $\Delta\alpha$ and $\Delta\delta$. For example, if both $\Delta\alpha$ and $\Delta\delta$ are independent and normally distributed with the same variance and zero means, the offset distances can be characterized by a Rayleigh distribution that has the following form:

$$f(x;\sigma) = \frac{x}{\sigma^2} e^{-x^2/2\sigma^2}, \tag{2.2}$$

where x is the offset distance and σ stands for the standard deviation of the $\Delta\alpha$ and $\Delta\delta$ distribution. The mode (0.4″ in Figure 2.6) of a Rayleigh distribution is equal to 1σ.

Cross-matching to AGNs is intended to help us quantify the tolerance for scatter in offset distance for nuclear transients. We expect some of these matched transients to be caused by unidentified supernovae instead of nuclear activity. In

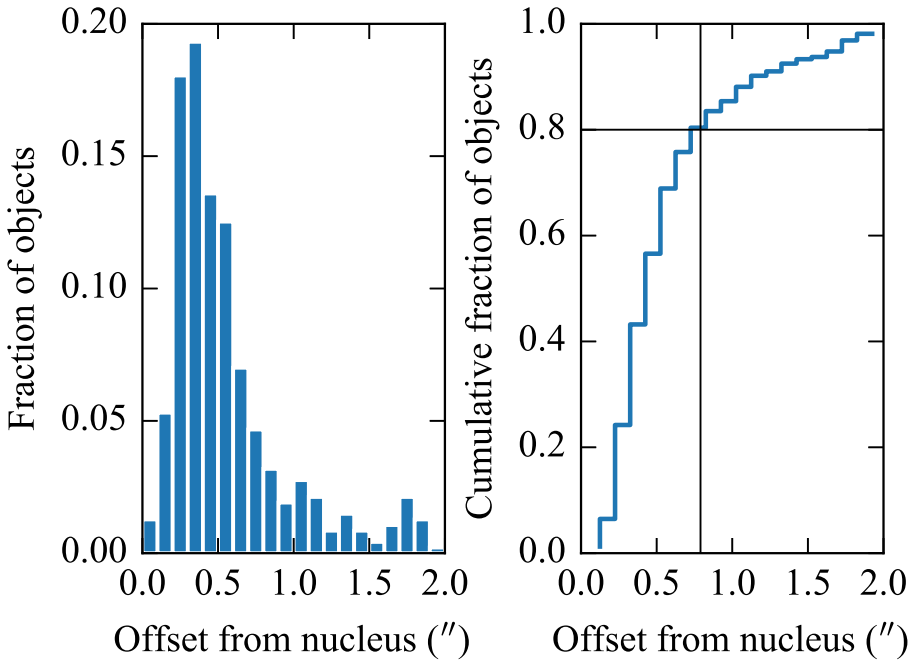

Figure 2.6: Flare-host separation for transients associated with known AGNs in PTF database (2009–2012). The spatial cut at $d < 0.8''$ includes 80% of the AGNs.

fact, the tail of the offset distance distribution should be mostly contributed by these supernovae that went off near AGNs.

For each object, we calculate the median of the separation of all detections available at the time a transient was saved and apply the separation cut to remove 971 transients that are non-nuclear. On average, P48 detected 6 new nuclear transients and 12 non-nuclear transients per night for an average nightly coverage of 771 deg^2. This corresponds to a surface density of 7.8×10^{-3} per deg^2 for nuclear transients on the sky.

2.3.2 Selection of extended hosts (step 2)

We remove transients with unresolved hosts that are classified as a star or a quasar. We searched for host galaxies within a 3″ radius of a transient using SDSS DR12 and PS1 DR1 catalogs. The SDSS star-galaxy separator comes with the `frames` pipeline and the results are stored in `type` under the `PhotoObjAll` table. In cases where a source is outside the imaging coverage of SDSS, we use measurements from PS1 3π Survey, which is available in DR1, to remove point-like sources. We define a point source as having `rMeanPSFMag` − `rMeanKronMag` < 0. This definition can segregate stars and galaxies with a 99% accuracy for galaxies brighter than 20 mag in the r band (Tachibana et al. in prep).

2.3.3 Selection of red galaxy hosts (step 3)

The major sources of contamination in the nuclear transient sample are SNe that fall inside the nuclear circle of a host galaxy and variable AGNs. While previously discovered TDEs seem to be found toward early-type galaxies, it has been well-established that core-collapse supernovae (CCSNe) are preferentially hosted by "blue" starforming galaxies (e.g. Kelly & Kirshner 2012). Therefore, we select only nuclear events hosted by red galaxies with empirically defined boundaries of $u-g>$ 1.0 mag and $g-r>0.5$ mag. This definition has worked well for previously discovered TDEs, which are shown as crosses in pink color in Figure 2.7. For transients outside of SDSS footprint, we use a looser host galaxy color cut that only requires $g-r>0.5$ mag using PS1 photometry since the u filter is absent in PS1.

The $u-g$ and $g-r$ colors of the SDSS host galaxies of the nuclear events are shown in Figure 2.7. Four CCSNe have been identified with follow up spectroscopy and the colors of their host galaxies are marked in red. As expected, the host galaxies of all four CCSNe have blue colors and are excluded by our empirical host color cut. Transients that are associated with known AGN hosts or classified with follow up spectroscopy are labeled in blue. The host galaxy color cut removes 27 out of 41 (66%) known or newly typed AGNs since a strong blue continuum is usually present in AGN spectra. In this step, we have removed iPTF16bco, which was found to be a changing-look quasar with a continuum flux increase of at least a factor of 10 over $\lesssim 1$ yr (Gezari et al. 2017b).

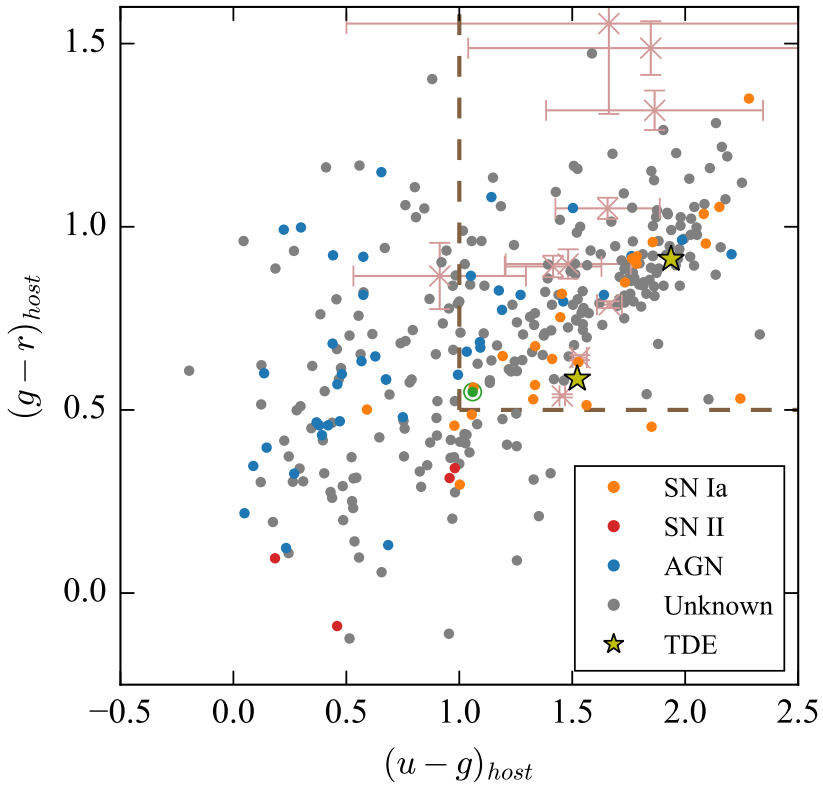

Figure 2.7: Color-color diagram of the host galaxies of iPTF nuclear transients. An empirical host galaxy color cut for red galaxies is represented by the dashed lines, where sources located in the top right corner satisfy our selection. The pink crosses show the host galaxy colors of previously reported TDEs from four optical surveys: PS1, PTF, SDSS, and ASASSN (see selection of comparison in subsection 2.6.2) that are inside SDSS footprint while the two stars mark the two TDEs (iPTF16axa and iPTF16fnl) discovered during this experiment.The only TDE located outside of this dashed box is PS1-10jh. However, a deeper imaging of PS1-10jh does show it satisfying this color selection; it is slightly outside the bounding box because of the high uncertainty in SDSS u photometry. By employing this color cut, we can filter out the CCSNe (red), which are preferentially hosted by blue starforming galaxies as well as a large fraction of AGNs. The green circle marks PS16dtm, which was reported as a TDE in a NLS1 galaxy.

2.3.4 Removal of AGN (step 4)

There is no physical process restraining TDEs from occurring in an AGN. However, AGNs are much more common (100x) than TDEs in the Universe and most of them exhibit some extent of intrinsic variability that is not of the interest of this study. To optimize the usage of follow up resources, we choose to eliminate transients that are likely due to AGN variability. We first remove known AGNs from the sample of TDE candidates. The candidate sample from step 3 is cross-matched with the 13th edition of quasars and active nuclei catalog (Véron-Cetty & Véron 2010). In addition, we also search SDSS for spectroscopic classification labels in table `SpecObj` and `galSpecInfo`. Nuclear events with host galaxies labelled as `QSO`, and `AGN` are most likely due to intrinsic variability and are removed to narrow down the sample size of candidate TDEs.

Secondly, we remove sources with variability history in PTF and iPTF from the sample since variability is an ubiquitous signature of AGN (e.g. Vanden Berk et al. 2004; Wilhite et al. 2005). We search for detection history in archival PTF and iPTF database from 2009 to 2016 at the coordinates of the nuclear transients. To avoid dubious subtractions, we require at least two detections ($>5\sigma$) on the same night to report the detection as 'real'. A source is removed from the sample if it was detected in at least one of the previous seasons and was not reported as any transient phenomenon other than AGN.

By limiting the search to inactive galaxies only, we have eliminated iPTF16ezh (or PS16dtm) from the sample, which is a unique event that has been reported as

a TDE in a narrow line Seyfert 1 galaxy at $z = 0.08$ by Blanchard et al. (2017).

2.3.5 Variability amplitude cut (step 5)

We exclude sources with insignificant variability amplitude by comparing the magnitude of the flare with respect to the PSF magnitude of the host. We define the the amplitude of variability (Δm_{var}) as

$$\Delta m_{var} = -2.5\log_{10}(10^{-\frac{m_{\rm PSF}}{2.5}} + 10^{-\frac{m_{\rm trans}}{2.5}}) - m_{\rm PSF}, \tag{2.3}$$

where $m_{\rm PSF}$ is the PSF magnitude of the host galaxy and $m_{\rm trans}$ is the host-subtracted transient magnitude. We remove nuclear transients with $|\Delta m_{var}| < 0.5$ mag that can be attributed to small variability from AGNs. By imposing the 0.5 mag variability cut, we are only sensitive to sources with a >60% flux increase in the nuclear region. This parameter can also be considered as a selection for high contrast against the core of the galaxy.

2.3.6 Selection of blue flares (step 6)

Since the spectral energy distribution (SED) of optically bright TDEs can be approximated by a blackbody peaking in the UV, these events are intrinsically blue. Therefore, we use $g_{\rm PTF}-R_{\rm PTF}$ colors from P48 and P60 to remove redder events that are most likely to be SNe. We query the database to calculate the mean $g_{\rm PTF}-R_{\rm PTF}$ color over a timespan of one week from the date of discovery for each source. We correct for Galactic extinction using the Cardelli et al. (1989) extinction curve with $R_C = 3.1$ and $E(B-V)$ values based on the Schlafly & Finkbeiner (2011) dust

map. We do not take the K-correction into account when calculating the color of the flares. Since a TDE spectrum is dominated by a hot blackbody with the optical portion being on the Rayleigh-Jeans tail, the color is not significantly affected by the K-correction. Considering a case where the K-correction would have a greater impact, we assume a blackbody spectrum with T_{BB}=2×10^{4}K, which is on the cooler end for TDEs. At z=0.3, the $g-R$ color would recover from −0.26 to −0.36 after applying K-correction. The correction on $g-R$ color would be even smaller for TDEs with typical temperature (3×10^{4}K) or at a lower redshift.

An important caveat is, however, the host extinction, which is expected to be non-negligible in galaxy nuclei. This value is largely unknown and sometimes may result in the rejection of a transient with a color cut. A steep extinction curve like SMC would redden the $g_{\rm PTF}-R_{\rm PTF}$ color by 0.12 mag. Considering these possible reddening mechanisms, we chose a conservative blue flare cut at $g_{\rm PTF}-R_{\rm PTF}$=0. We only use $g_{\rm PTF}$ and $R_{\rm PTF}$ pairs that were observed on the same night with the same telescope (P48 or P60) for the color calculation. With the condition $g_{\rm PTF}-R_{\rm PTF}$<0 mag (Figure 2.8), roughly half of the flares were rejected from the sample.

2.3.7 Brightness limit for spectroscopic follow-up (step 7)

Finally, we remove sources that were too dim for spectroscopic follow up with 4-meter class telescopes (e.g. DCT) if $g_{\rm PTF}$ or $R_{\rm PTF}$ did not reach <20 mag in 3 days after being saved. The final sample consists of 26 sources.

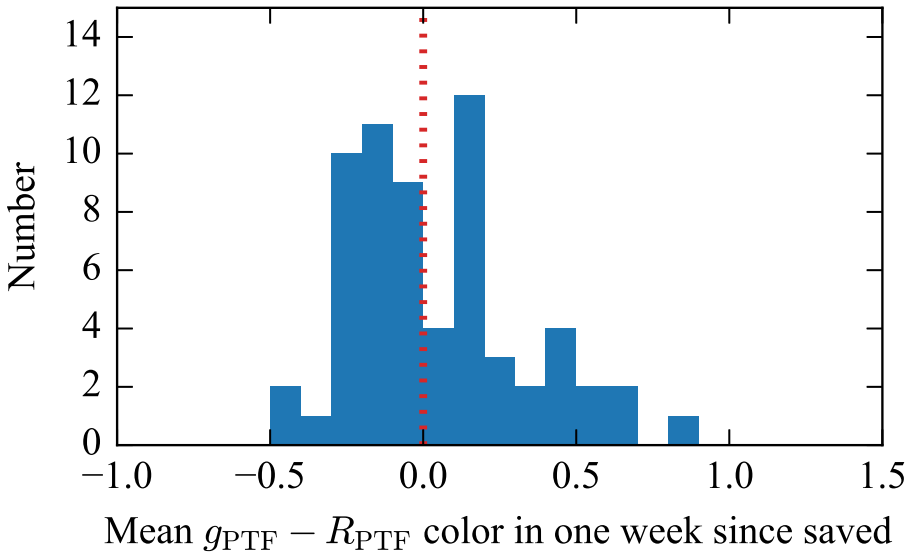

Figure 2.8: The average $g_{\rm PTF}-R_{\rm PTF}$ color of the transients in the first week of discovery. The colors shown here are Galaxy extinction corrected. With the color cut $g_{\rm PTF}-R_{\rm PTF}< 0$ mag, we removed 30/63 ($\approx$48%) of the sources.

2.4 Photometric and Spectroscopic Follow up

2.4.1 P48 and P60 photometry

The Palomar 48-inch telescope (P48) is the workhorse of iPTF. During the experiment, the targeted fields were exposed for 60s for each image to reach a depth of ∼20.5 mag in the $g_{\rm PTF}$ and $R_{\rm PTF}$ bands. The raw images were detrended and astrometrically and photometrically calibrated at IPAC (Laher et al. 2014).

Follow up photometry observations with the robotic Palomar 60-inch telescope (P60) is sometimes triggered in *gri* bands to get color and better sampling of the light curve. The P60 raw images were processed by the Fremling Automated Pipeline to be subtracted against the reference images from SDSS (Fremling et al. 2016). We did not obtain any host-subtracted photometry for sources outside of the SDSS footprint with P60.

2.4.2 Swift UVOT and XRT photometry

We obtained *Swift* (Gehrels et al. 2004) UVOT (Roming et al. 2005) observations in the bluest *uvw*2 (1928 Å) filter for classification purpose. The exposure time for each *Swift* trigger is 1ks in order to achieve a limiting magnitude of $uvw2 \sim 23$ mag. We used the task `uvotsource` in the HEASoft package to extract the photometry within a 5″ radius aperture in the AB magnitude system.

Simultaneous *Swift* XRT (Burrows et al. 2005) observations were processed by the Swift Data Science Centre pipeline. The pipeline extracts counts from the source

in the energy band 0.3 – 10 keV by accounting for dead columns and vignetting.

2.4.3 SED Machine

The Spectral Energy Distribution Machine (SEDm) is a integral-field-unit (IFU) spectrograph mounted on the P60 telescope (Blagorodnova et al. 2017b). The wide FOV (28″), low resolution (R∼100) IFU is a powerful tool for classifying transients down to $r \sim 19$ mag. The data obtained by SEDm IFU are automatically processed by the data reduction pipeline, which includes basic image reduction, defining the IFU spatial and wavelength geometry, and spectral extraction. The extracted spectra are flux calibrated with the observations of spectrophotometric standard stars.

2.4.4 P200 DBSP

We observed with the Double Beam Spectrograph (DBSP) on the 200-inch Hale telescope at Palomar Observatory (P200). A dichroic is used to split the light into a blue and a red component. The observing setup includes a 1″ wide slit and 600g/mm grating, giving a dispersion of 1.5 Å/pixel. The images are reduced with the `pyraf-dbsp` script.

2.4.5 DCT

Spectroscopic observations were made with the DeVeny spectrograph mounted on the 4.3 meter Discovery Channel Telescope at Lowell observatory. We used a slit

width of 1.5" since the seeing did not get better than 1″. A 300g/mm grating is used to achieve a dispersion of 2.2 Å/pixel. We used standard IRAF routines to reduce the data. The procedures include bias subtraction, flatfielding, aperture extraction, wavelength calibration, and flux calibration.

2.4.6 Keck LRIS

Spectroscopic observations were made with the Low Resolution Imaging Spectrometer (LRIS; Oke et al. 1994) on Keck observatory. The observing configuration includes a 1″ slit and a 400/3400 grism that gives a FWHM resolution of ∼7Å. The data were reduced with the LRIS automated reduction pipeline[1] and flux-calibrated with the standard star BD+28d4211.

2.5 Classification

The photometric properties of the final sample of 26 candidates are listed in Table 2.3. Classification spectra were taken for 9 of the candidates. We requested *Swift* UVOT photometry in *uvw*2 band for 7 of the high-confidence transients in this final sample that did not have light curves or color evolution resembling a SN Ia or AGN, and did not have a classification spectrum. We describe the classification based on both spectroscopy and photometry in the following sections. Even if a source was not followed-up during the flare, we still obtain spectroscopy of their host galaxies at a later time to measure their redshifts. The host spectra are shown

[1] `http://www.astro.caltech.edu/~dperley/programs/lpipe.html`

in the Appendix with observing details described in Table 2.5. The spectroscopic data will be be made available via WISeREP (Yaron & Gal-Yam 2012).

2.5.1 Supernovae

2.5.1.1 Type Ia supernovae

The similarity in SN Ia light curves has direct application to determining cosmological distances. The SN Ia light curves become even more uniform after accounting for the empirical correlation between the maximum luminosity and the width of the light curve (Phillips 1993), making them the standardizable candles in the Universe. Unlike CCSNe, SNe Ia do not have a preference for star-forming regions.

In this sample, 5 transients are spectroscopically confirmed SNe Ia classified with the Supernova Identification code (SNID; Blondin & Tonry 2007). For the transients without any follow up spectrum, we inspect the light curves by eye and found 9 transients having burst-like light curves and/or $g_{\rm PTF}-R_{\rm PTF}$ color reddening with time that are characteristic of a SN Ia. We label them as "SN Ia phot" in Table 2.3. A typical SN Ia light curve is characterized by a smooth rise ($\lesssim$20 days) and decay ($\sim$0.1 mag per day). Contrary to the lack of color evolution in TDEs, the color of a SN Ia reddens as the ejecta expand with time.

We obtained host spectra for all of these photometric SNe Ia (Figure 2.9) in 2017 and measured their redshifts. The peak absolute magnitudes of these photometric SNe Ia are all typical of a SN Ia with m_{peak} around -19 mag. *Swift*

observations in $uvw2$ for iPTF16fmd and iPTF16gyl were both >22 mag, which is consistent with the SN Ia classification.

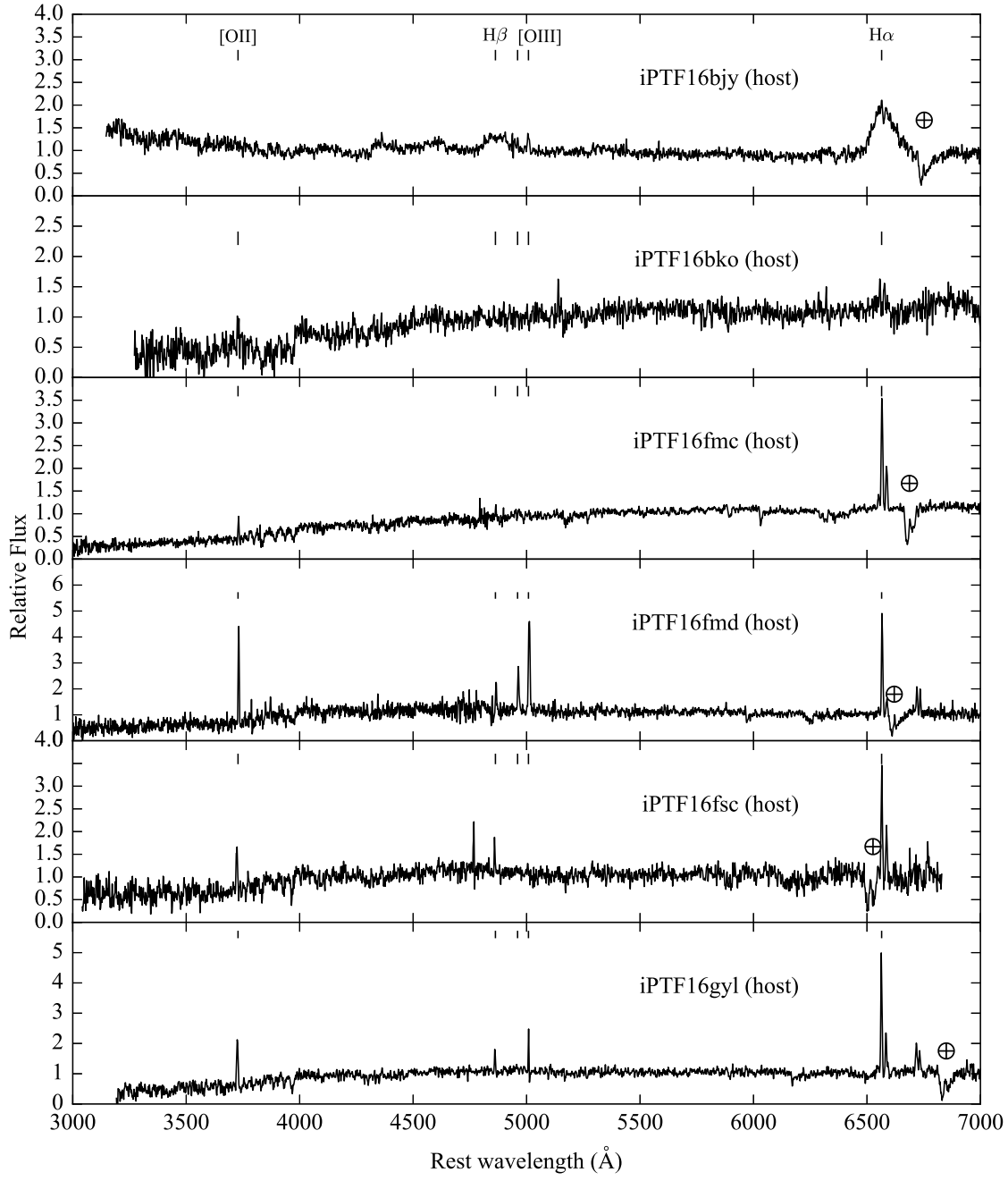

Figure 2.9: Host galaxies of SNe Ia classified based on the photometry. Strong telluric absorptions are marked with the $\oplus$ symbol.

To verify our classification, we perform light curve fitting on all 9 photometric SNe Ia as well as 5 spectroscopically confirmed SNe Ia using the implementation of the SALT2 model in Python package `sncosmo`[2]. By fixing the redshift determined from host galaxy spectra, we simultaneously fit light curve data points from both IPAC and NERSC pipelines with the SN Ia time-series model convolved with filter response in $g_{\rm PTF}$ and $R_{\rm PTF}$. The key parameters in this model are the date of B–band maximum (t_0), normalization x_0, light curve stretch x_1, and the color c. The best-fit light curves of the 8 photometric SN Ia are shown in Figure 2.10 while the best-fit parameters of all 14 sources are listed in Table 2.4. Most of the sources (12/14) have a goodness of fit $\chi^2_\nu < 3.0$. The 2 sources with a slightly larger χ^2_ν include 1 spectroscopic (iPTF16bke) and 1 photometric (iPTF16hcn) SN Ia.

2.5.1.2 Probable core-collapse supernovae

While confirming the SN Ia classification through light curve fitting, we noticed an outlier, iPTF16bmy, that has a decline too steep to be consistent with a SN Ia light curve. We show the light curve of iPTF16bmy and the best-fit SN Ia light curve ($\chi^2_\nu = 58.8$) in dotted lines in Figure 2.11.

We obtained a host spectrum of iPTF16bmy with P200 on Jul 29 2017. The host spectrum of iPTF16bmy (Figure 2.12) shows absorption lines dominated by an old stellar population in an elliptical galaxy at $z = 0.129$. The redshift corresponds to a peak magnitude of -18.9 mag in $g_{\rm PTF}$. The fast rise to peak (<10 days) would also be unusual for an AGN. The faster rise than decline timescales and the blue

[2] `https://github.com/sncosmo/sncosmo`

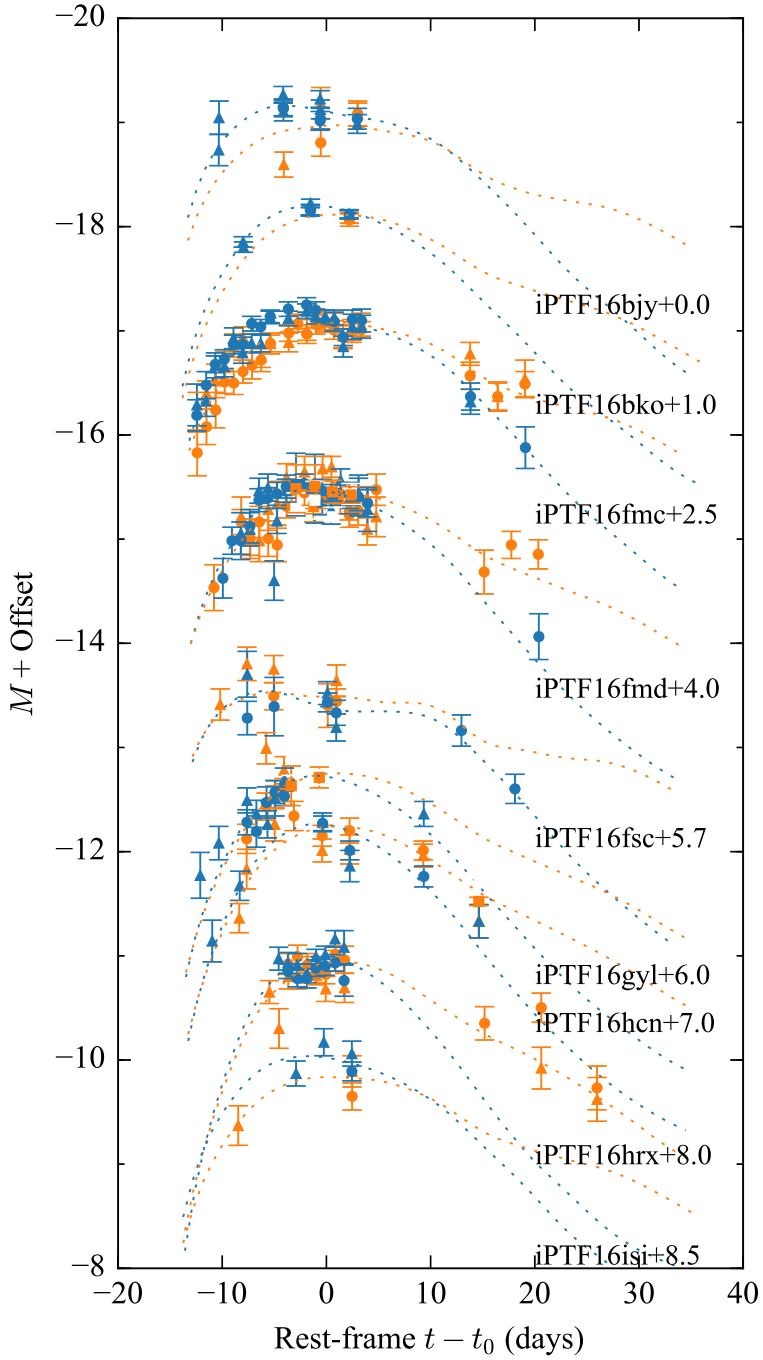

Figure 2.10: Light curves of the photometric SN Ia in the sample. The blue and orange dotted curves show the best-fit result for $g_{\rm PTF}$ and $R_{\rm PTF}$ band data with the SALT2 model. The circles show the photometry extracted by the IPAC pipeline while the triangles show the photometry extracted by the NERSC pipeline.

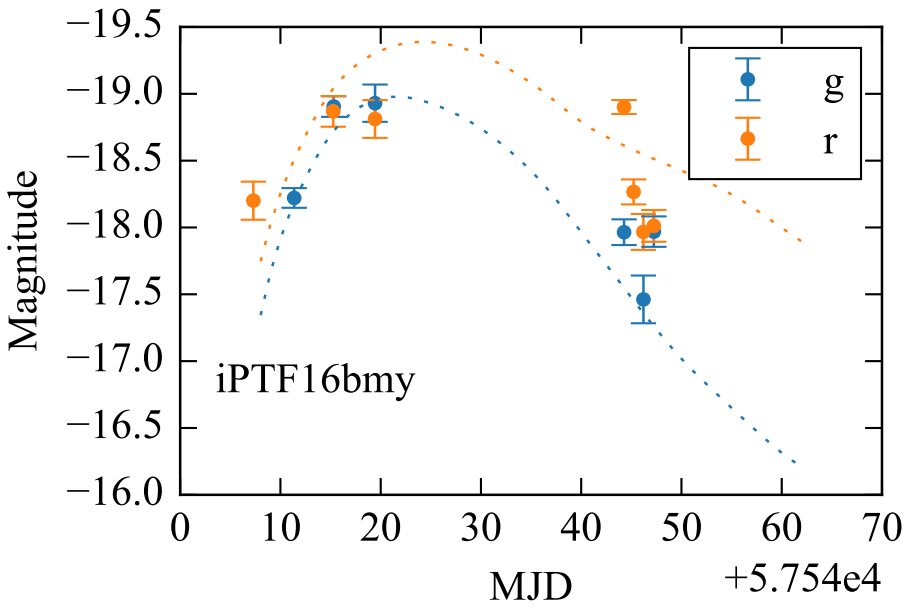

Figure 2.11: The light curve of iPTF16bmy The dotted line shows the best-fit SN Ia light curve with $\chi^2_\nu = 58.8$.

color ($g_{\rm PTF} - R_{\rm PTF} = -0.14$) near peak resemble the sample of rapidly evolving transients found by Drout et al. (2014), which is likely to have a CCSN origin. All the host galaxies of the rapidly evolving transients have nebular emission lines that are indictive of ongoing star formation. By doing a careful fitting with `ppxf` (Figure 2.12), we do see some weak level of Hα, [NII], and [OIII] emission. With the information available to us, we classify iPTF16bmy as a "probable" CCSN in Table 2.3 even though we cannot rule out iPTF16bmy as a subtype of SNIa.

2.5.2 Variable AGN

We obtained spectra of iPTF16ayd and iPTF16fqa during their flaring states and classified them as AGNs. iPTF16ayd was typed as an AGN due to the presence

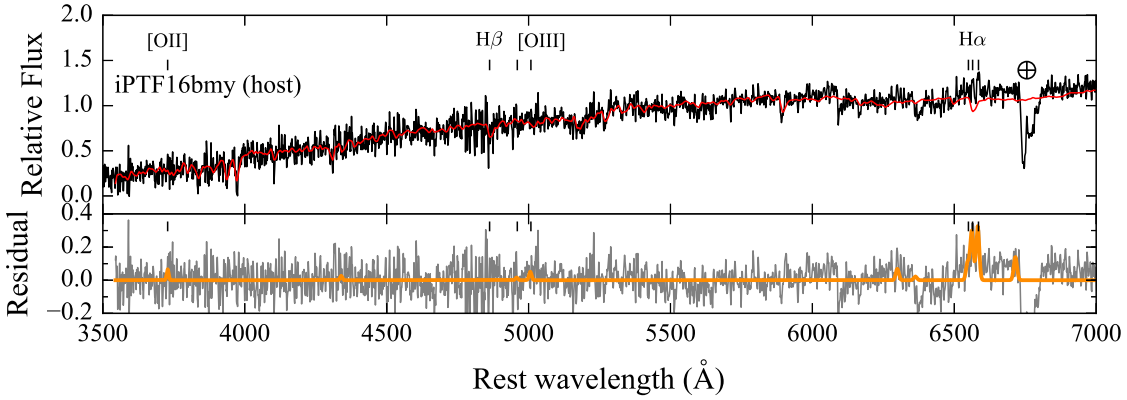

Figure 2.12: Host spectrum of iPTF16bmy. The black line in the top panel shows the P200 spectrum of the host galaxy of iPTF16bmy while the red line shows the best-fit galaxy spectrum from `ppxf`. The bottom panel shows the residual of the fit in grey. The emission line profiles that were simultaneously fitted with the stellar templates are colored in orange. Weak Hα, [NII], and [OIII] lines detected in the host spectrum are suggestive of ongoing starformation.

of the broad Balmer emission lines (FWHM($H\beta$) = 3080 km s^{-1}) that are typical of a Type 1 Seyfert. Although the light curve of iPTF16fqa surged by ≈2 mag in 60 days, its flaring spectrum does not show broad P-Cygni spectral features like an SN Ia. The *Swift* observation of iPTF16fqa showed no X-ray emission though the $uvw2$ magnitude had increased by 1 mag compared to the pre-flare GALEX NUV photometry. While the lack of P-Cygni line and increase in UV flux are both in favor of a TDE origin, we did not notice any HeIIλ4686 emission that are often seen in optical TDEs in its flaring spectrum. In addition, we did not detect any change in the optical continuum or the emission line in this source when we made another spectroscopic observation with P200 in 2017. This is at odds with previously detected TDEs, where spectral evolution becomes noticable on weekly to monthly timescales (e.g. Holoien et al. 2014; Blanchard et al. 2017). The narrow line ratios (Figure 2.13) also place this object within the boundary for Seyfert galaxies. The overall spectroscopic properties of iPTF16fqa are more consistent with the scenario of a variable AGN.

We classify 7 other transients in the sample as photometric AGN because their light curves do not have an obvious rising or declining trend. The light curves of all 9 spectroscopic and photometric AGNs in our sample are shown in Figure 2.14.

We verify the photometric AGN classification with the host spectra obtained in 2017. Among these 7 photometric AGNs, iPTF16fly, iPTF16fjc, and iPTF16hma have broad Balmer emission lines (Figure 2.15). We measure and report the broad Hβ line widths in Table 2.5. Among the sources in our sample, iPTF16fly has the highest redshift (z=0.45) that the Hα is shifted out of the bandpass. We measure

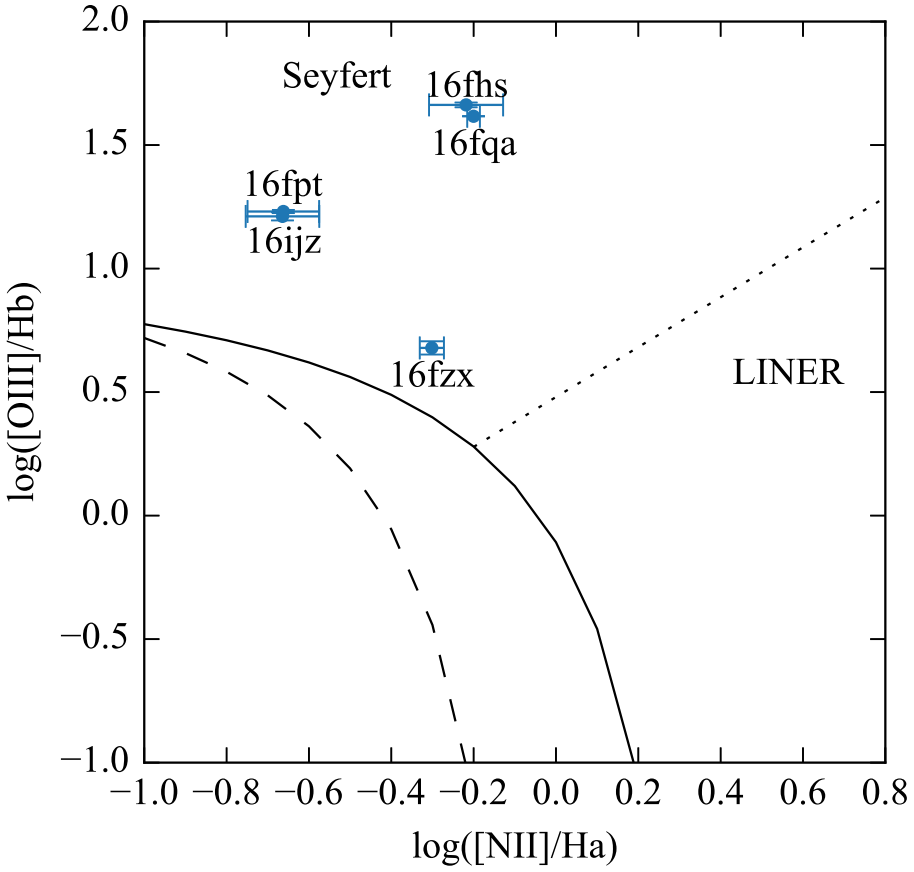

Figure 2.13: BPT diagram with the solid (Kewley et al. 2001) and dashed (Kauffmann et al. 2003) line separating AGN from starforming galaxies. The dotted line represents the Seyfert LINER demarcation (Cid Fernandes et al. 2010). The photometric AGNs that do not have broad Balmer lines are color-coded in blue.

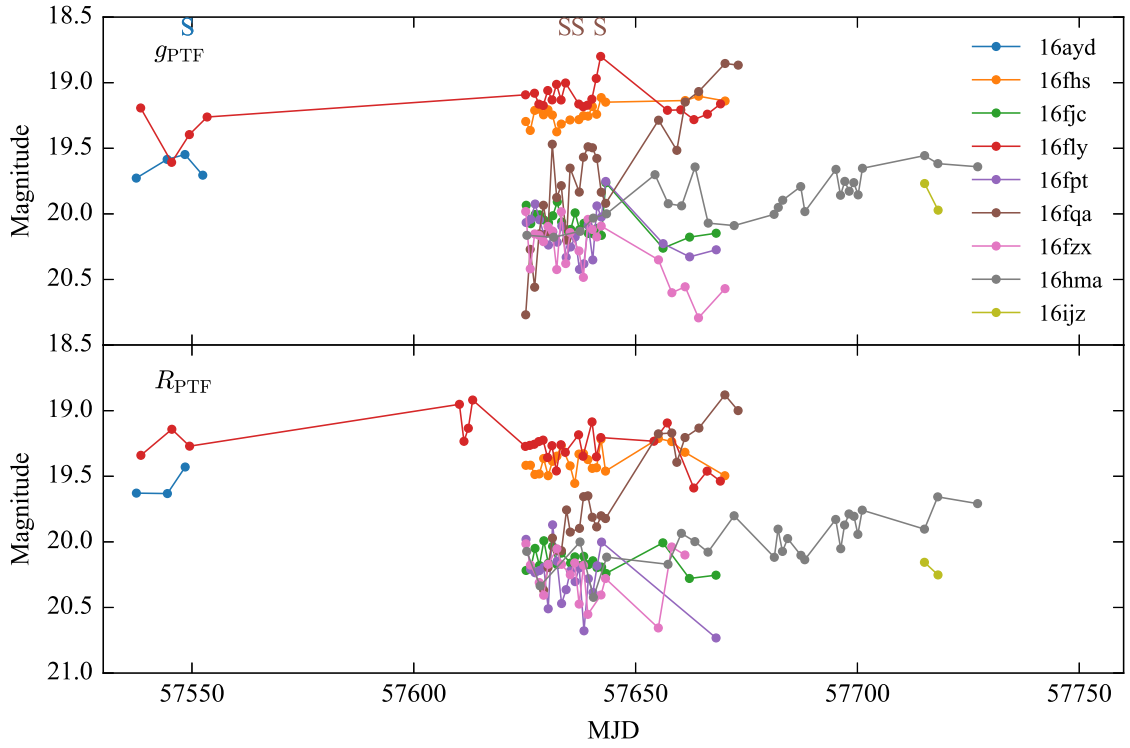

Figure 2.14: Light curves of the spectroscopically confirmed AGNs and candidate AGNs in our sample. AGN candidates are selected based on the light curve, which lacks obvious rise or fall over the monitoring period. Archival PTF data shows no detection at the positions of the AGN candidates.

the narrow line ratios for the 7 AGNs without broad emission lines and plot them on the [OIII]/Hβ versus [NII]/Hα diagnostic diagram (Figure 2.13). Their spectra are shown in Figure 2.16. One of these transients, iPTF16fpt, has a pre-flare SDSS spectrum. Because the host spectrum of iPTF16fpt is dominated by the underlying galaxy, we re-measure the line ratios by fitting the SDSS spectrum with `ppxf` (Cappellari 2017), which allows simultaneous fitting of the emission lines and the host galaxy template. We classify iPTF16fhs, iPTF16fpt, iPTF16ijz, and iPTF16fzx as AGNs based on their narrow line ratios as shown in Figure 2.13.

All 9 transients that are classified as AGNs have a variability amplitude $|\Delta m_{var}| > 0.7$ mag at peak. Five of them (iPTF16ayd, iPTF16fjc, iPTF16fly, iPTF16fpt, and iPTF16hma) have $|\Delta m_{var}| > 1.0$ mag, making them changing-look quasar (CLQ) candidates (MacLeod et al. 2016). CLQs are a recently emerged class of objects that exhibit extreme variability in both continuum and emission lines on the timescale of a few years (Shappee et al. 2014; LaMassa et al. 2015; Gezari et al. 2017b). The name refers to the fact that their optical spectra change from a Type 1 to a Type 2 Seyfert or vice versa. Compared to mundane AGNs that only vary by 20% on timescales of months to years (e.g. Hook et al. 1994), CLQs have sparked even more questions on the origin of AGN variability. Currently, it is generally agreed that variable obscuration in the line of sight, lensing of a background quasar, or a tidal disruption event cannot explain every aspect of a CLQ.

This leaves changes in the accretion rate as the favored mechanism for what is causing the CLQs. However, the timescale for viscous perturbations to propagate in a classical thin accretion disk in the UV/optical emitting region ($\approx 100 r_g$) is

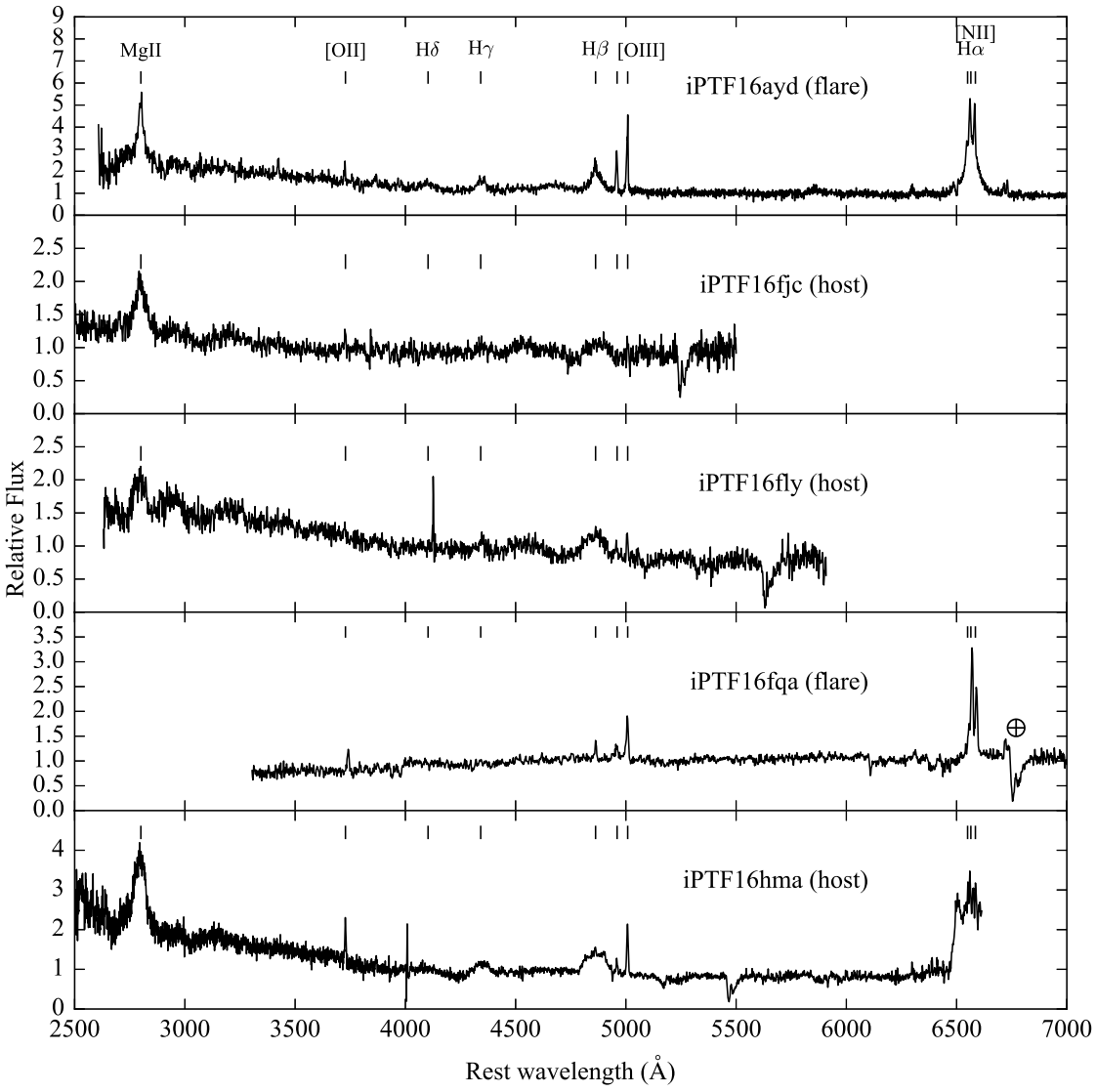

Figure 2.15: AGNs classified based on the presence of broad emission lines. Strong telluric absorptions are marked with the $\oplus$ symbol.

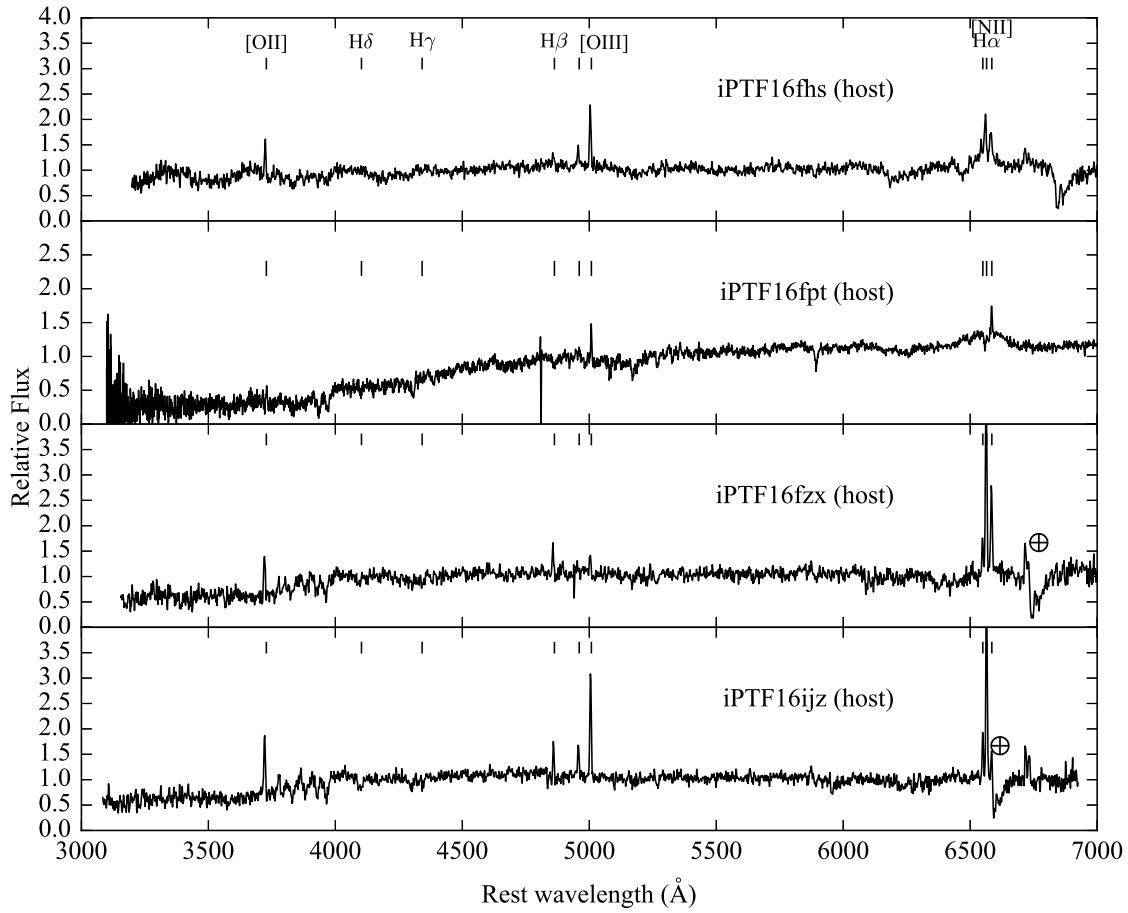

Figure 2.16: AGNs classified by [OIII]/Hβ versus [NII]/Hα line ratio. Strong telluric absorptions are marked with the $\oplus$ symbol.

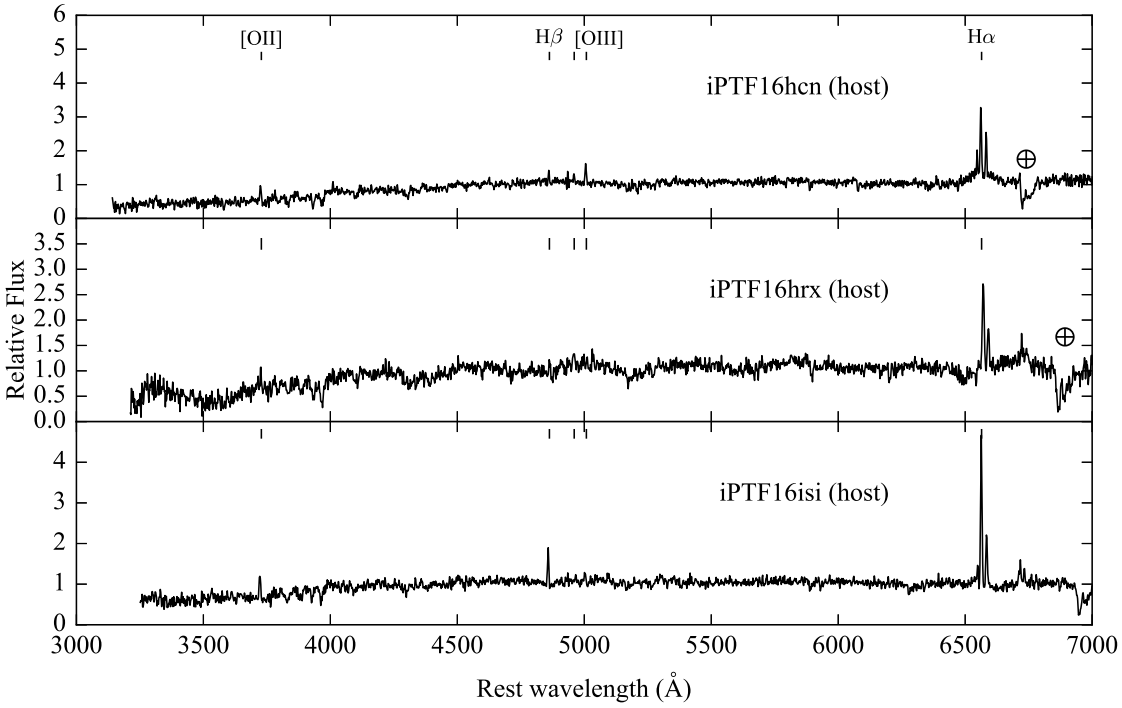

Figure 2.17: Figure 2.16 continued.

on the order of 10^3 years (Hung et al. 2016), which is much longer than what was observed for CLQs. But this may be resolved if the UV/optical emission of CLQs are irradiated spectrum with variability originating from a smaller radius, where the viscous timescale is effectively reduced.

Although we cannot verify whether these transients have gone through a transition in spectral class at this point due to the absence of pre-flare spectra, it may be worthwhile to keep an eye on these candidates since some CLQs have shown a reversion to the original spectral class after tens of years (e.g. McElroy et al. 2016).

It has been shown that the difference spectra of quasars could be well fitted by a thin accretion disk spectrum with changing accretion rates (e.g. Pereyra et al. 2006; Hung et al. 2016), which is consistent with a disk spectrum that follows $f_\nu \propto \nu^{1/3}$ in

the optical emitting region. Even in the extreme case of CLQs, it has been reported in some cases that the difference spectra also have power law indices in agreement with a geometrically thin optically thick accretion disk (Gezari et al. 2017c; MacLeod et al. 2016).

The power-law thin disk spectrum corresponds to a $g_{\rm PTF}-R_{\rm PTF}\sim -0.1$ mag. The $g_{\rm PTF}-R_{\rm PTF}$ colors measured for iPTF16fhs, iPTF16fjc, iPTF16fpt,and iPTF16fzx are consistent with this value while iPTF16fly, iPTF16fqa, iPTF16hma, and iPTF16ijz are slightly bluer with $g_{\rm PTF}-R_{\rm PTF}\sim -0.2$ mag. It is interesting that 3 out of 4 Type 1 Seyferts with broad emission lines, including iPTF16ayd ($g_{\rm PTF}-R_{\rm PTF}\approx -0.01$ mag), seem to deviate from the thin disk prediction. As discussed in Hung et al. (2016), the deviation could be caused by the presence of broad emission lines in the bandpass that are also variable. While changes in accretion rate can describe the change in the AGN continuum quite well, variability in the broad emission lines may be driven by different physical mechanisms.

2.5.3 TDEs

During the rolling $g_{\rm PTF}+R_{\rm PTF}$ experiment, iPTF discovered two TDEs, iPTF16axa at $z = 0.108$ (Hung et al. 2017a) and iPTF16fnl at z =0.016 (Blagorodnova et al. 2017a), on UT 2016 May 29 and 2016 August 29, respectively. *Swift* was triggered immediately after the discovery for iPTF16axa. The brightening in the $uvw2$ filter along with the strong HeII and Hα line in the Keck DEIMOS classification spectrum are both in agreement with the TDE interpretation. iPTF16axa has a persistent

blackbody temperature of $\sim 3 \times 10^4$ K throughout the 3-months monitoring period. The light curve of iPTF16axa followed the classic $t^{-5/3}$ power-law decline. No X-ray or radio emission were detected for this source. In Hung et al. (2017a), we measured the stellar velocity dispersion with high resolution spectroscopy and derived a black hole mass of $M_{BH} = 5.0^{+7.0}_{-2.9} \times 10^6$ $M_\odot$ using the M-σ relation in McConnell & Ma (2013). The black hole mass and the overall light curve properties of this source resemble the archetypal TDE PS1-10jh (Gezari et al. 2012).

On the other hand, iPTF16fnl was classified on the same night of discovery by the low resolution SEDm (Blagorodnova et al. 2017b). iPTF16fnl is the nearest (66Mpc) and also the faintest TDE ever found at optical wavelengths. The light curve of iPTF16fnl declined much more rapidly than the other optically detected TDEs. Whether this decline follows an exponential form or a power-law with a steeper exponent is still debated. iPTF16fnl also has a constant blackbody temperature of $\sim 2 \times 10^4$ K and its host galaxy happens to be an E+A galaxy that features strong Hδ absorption.

Both of the TDEs exhibit strong HeII and Hα line in their spectra. The helium-to-hydrogen ratios in these two objects are both higher than what would be expected in a nebular environment with solar abundance of He/H. This suggests that optical depth effects may be important in the line emitting gas in TDEs. For example, high density gas could lead to the suppression of Balmer lines as these transitions become optically thick (Hung et al. 2017a; Roth et al. 2016).

2.5.4 The Swift sample

We used *Swift* ToO observations in the UV and X-rays under our Cycle 12 program (PI Gezari) to identify TDEs from our high-confidence candidates that do not have light curves resembling a SN Ia or an AGN at the time of discovery. We obtained *Swift* observations for a total of 7 candidates in our sample, 6 of which were scheduled with the time allocated to our Cycle 12 program and 1 (iPTF16fnl) was scheduled through the regular ToO request. We triggered *Swift* on these 6 candidates because we were unable to assign them to any spectroscopic observing runs in the timeframe of 3 days after saving. A separate *Swift* ToO request for a two-months long monitoring campaign was submitted for iPTF16fnl after the rapid classification by SEDm. Details of these *Swift* observations are presented in Table 2.6. We show the Galactic extinction corrected $g_{\rm PTF}-R_{\rm PTF}$ and $uvw2-R_{\rm PTF}$ color of all the nuclear events in our sample in Figure 2.18. The $g_{\rm PTF}$ and $R_{\rm PTF}$ photometry of the flares are chosen to be the nearest to the epoch of the *Swift* observation. We note that although the $g-r$ color of iPTF16gyl had reddened when *Swift* observed it, it had a $g_{\rm PTF}-R_{\rm PTF}$ color of -0.3 at the time that we triggered *Swift*. We also plot the mean $g_{\rm PTF}-R_{\rm PTF}$ color in the first week of discovery for the AGNs (blue), SNe Ia (yellow), and unclassified sources (grey) in our sample. The two TDEs are well separated from the rest of the non-TDEs in $uvw2-R_{\rm PTF}<-0.5$ mag (red dotted line).

While we are able to get rid of the AGNs by adopting a more stringent optical color cut on the flare ($g_{\rm PTF}-R_{\rm PTF}< -0.2$ mag), SNe Ia can appear as blue as the

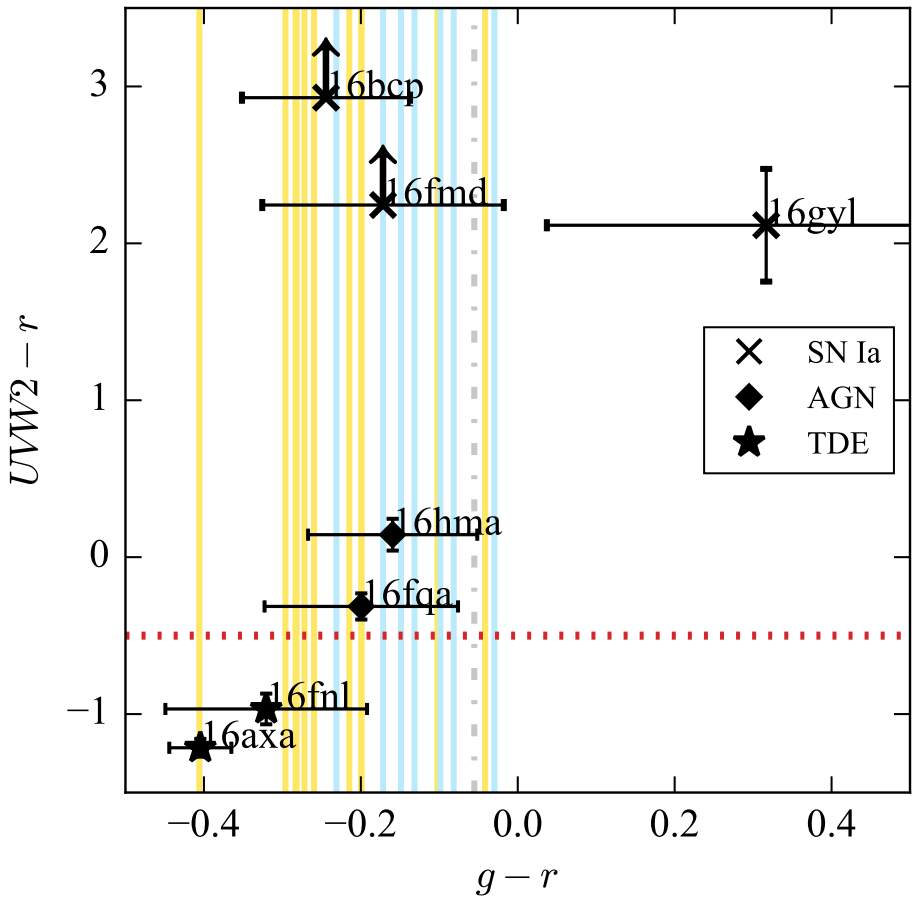

Figure 2.18: Color-color diagram of the transient events in the sample. The symbols mark sources that were observed by *Swift* and the $g_{\rm PTF}$ and $R_{\rm PTF}$ magnitudes are chosen to be the nearest to the time of the *Swift* observation. The vertical lines show the mean $g_{\rm PTF}-R_{\rm PTF}$ color of the sources in the final sample that were not observed by *Swift*. The yellow lines represent sources that are classified as SNe Ia while the cyan lines represent sources that are classified as variable AGNs. iPTF16gyl had a $g_{\rm PTF}-R_{\rm PTF}$ color of -0.3 when we triggered *Swift* but has reddened in $g_{\rm PTF}-R_{\rm PTF}$ by the time *Swift* observed it.

TDEs up to one week post peak (e.g. Miller et al. 2017). We therefore conclude that the UV is an important discriminator between TDEs and SNe Ia at early times.

2.6 Discussion

2.6.1 Selection on SDSS vs non-SDSS fields

Among the unique fields, 77%(509 out of 660) of the fields also lie within the survey footprint of SDSS DR12. The absence of SDSS data would have direct impact on the selection based on host galaxy properties (subsection 2.3.2, subsection 2.3.3) since our selection requires $u - g > 1.0$ and $g - r > 0.5$ and the PS1 survey was conducted without the u band. In our final sample, 19 out 26 sources were observed by SDSS and have archival SDSS photometry. If we apply the host morphology and host galaxy color cut with only $g - r > 0.5$ for PS1 data, our pipeline would end up selecting 35 candidates. All nine additional candidates were rejected in our original selection for being in SDSS footprint but not satisfying $u - g > 1.0$ mag. From this, we estimate the contamination rate to increase by $\sim$35% when only using PS1 data.

2.6.2 Completeness

In order to determine the completeness of our search, we apply our selection criteria on 10 well-studied TDEs that were discovered by ground-based optical surveys. These 10 TDEs are TDE1 and TDE2 from SDSS (van Velzen et al. 2011), PS1-11af (Chornock et al. 2014), PS1-10jh (Gezari et al. 2012), ASASSN-14ae, ASASSN-14li, ASASSN-15oi (Holoien et al. 2014, 2016b,a), PTF09ge, PTF09axc, and PTF09djl

(Arcavi et al. 2014). We do not consider TDE candidates with DEC < -20 deg (OGLE16aaa (Wyrzykowski et al. 2016), ASASSN-15oi (Holoien et al. 2016a), and ASASSN-15lh (Dong et al. 2016; Leloudas et al. 2016)) here since we require host galaxies information from SDSS or PS1 in our selection.

All ten TDEs pass our selection criteria (see Table 2.2), with a few caveats described below. All ten TDEs have extended host galaxies and $g-r$ ¡ 0 at discovery. The only host galaxy the does not pass our host color cut is that of PS1-10jh, which has $(u-g)_{host} = 0.91 \pm 0.38$ mag (Figure 2.7) according to SDSS. The large error bar in host color is mainly contributed by the faint u band photometry with $u_{host} = 22.85 \pm 0.37$ mag. In fact, the host color of PS-10jh does satisfy our criteria using a deeper stacked CHFT u band and PS1 g band image (Kumar et al. 2015), which indicates an (u-g)host $= 2.00 \pm 0.015$ mag.

As mentioned earlier, PS16dtm is rejected by our selection since its pre-outburst archival SDSS spectrum indicates that the host is consistent with a Seyfert galaxy. All ten TDEs have $|\Delta m_{var}| > 0.5$ mag at peak except TDE1, which has a $|\Delta m_{var}|$ of 0.3 mag. However, we must note that TDE1 was discovered after peak, and so it likely had a larger amplitude of variability. In sum, our selection criteria are inclusive of all the properties of all optically discovered TDEs hosted by quiescent galaxies.

2.6.3 Contamination

Our final sample consists of 14 SNe Ia, 9 AGNs, 1 probable core-collapse SN, and 2 TDEs. To investigate if TDEs can be separated from AGN and SN in other parameter space, we use a control sample 26 SNe Ia, 34 AGNs, and 3 TDEs (including PS16dtm) to compare their properties. This control sample consists of spectroscopically classified sources derived from the nuclear transient sample ($d < 0.8''$) in extended host galaxies in this study. We compare the cumulative distribution of different parameter space in Figure 2.19 including the absolute peak magnitude in $g_{\rm PTF}$ band, absolute host PSF magnitude in r, apparent host PSF magnitude in r, and Δm_{var} in Figure 2.19.

As we pointed out in subsection 2.5.4, about 67% (6 out of 9) of AGNs, 43% (6 out of 14) of SNe Ia, and a probable CCSN can be effectively removed in our final sample by employing a more stringent flare color cut of $g_{\rm PTF} - R_{\rm PTF} < -0.2$ mag. We notice from panel b and c in Figure 2.19 that AGNs have brighter absolute flare magnitudes and absolute host magnitudes compared to TDEs and SNe Ia, which would be two potential ways to remove AGN. Unfortunately, these two parameters require spectroscopy to determine the redshift and it is uncertain if the photometric redshift would be accurate enough for making these cuts. However, we find photometric criteria that can be applied to further reduce the contamination by AGNs and SNe Ia. We verify that $|\Delta m_{var}| < 0.5$ mag (panel d in Figure 2.19) is an effective filter for AGNs. We also find that a magnitude cut on the host galaxy of $r_{\rm PSF} < 21.0$ mag removes 25% of the SNe Ia. This is in good agreement with

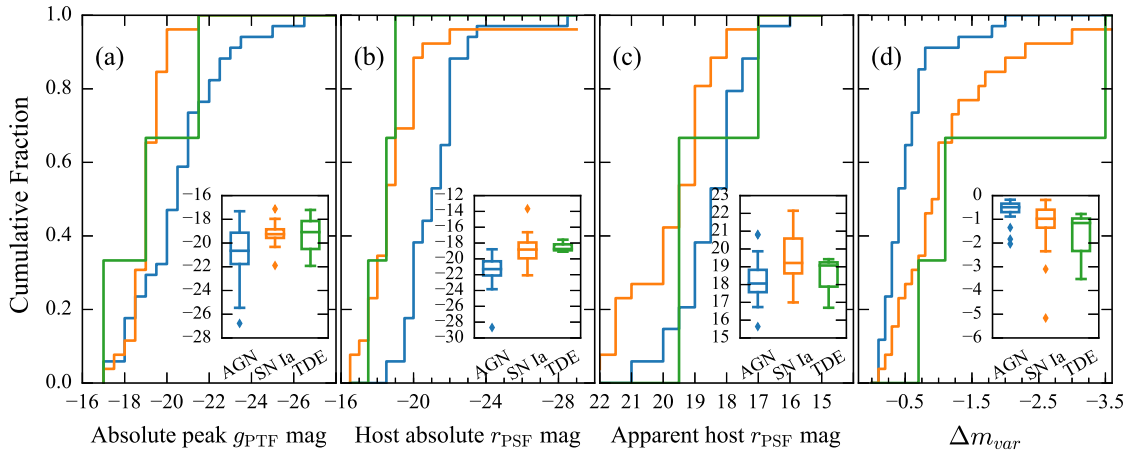

Figure 2.19: The cumulative distribution of the (a) absolute peak magnitude in $g_{\rm PTF}$ band, (b) absolute host PSF magnitude in r, (c) apparent host PSF magnitude in r, and (d) Δm_{var} for spectroscopically typed nuclear transients with extended hosts. The insets show the distribution of parameters in the form of box plot that marks the interquartile range (IQR) for each object class. Although AGNs appear to be brighter than SNe Ia and TDEs in (a) and (b), it is uncertain if photometric redshift would be accurate enough for making these cuts. A magnitude cut on the host galaxy at apparent $r_{\rm PSF}$ <21.0 mag may help to remove some of the SNe Ia. Our variability amplitude cut can effectively remove AGNs as shown in (d).

the results of Kumar et al. (2015), who found that a combination of host galaxy apparent magnitude and variability amplitude can be used to discriminate between AGN and SNe, where AGN have brighter host magnitudes and smaller variability amplitudes relative to their host galaxy flux.

In subsection 2.3.1 we removed flares that are farther than 0.8″ away from the centroid of their host galaxies. This offset was calculated by taking the median of all offsets measured from each detection up to the time when the transient was saved. We investigate this condition further by plotting the distributions of the flare-host separation for our control sample with spectroscopically confirmed AGNs (34), SNe Ia (26), and TDEs (3). The histograms of the median separation in the first week of discovery are plotted in Figure 2.20.

We noticed that the flare-host separation for AGN peaks toward 0.3″ while the separation for SN Ia peaks around 0.2″ and 0.6″. The TDEs, with a small sample size of 3, all seem to have a nuclear offset of less than 0.2″. While it is unclear why there seem to be a double-peaked offset for SN Ia, the second peak of SN Ia clearly stands out from the distribution of the nuclear flares. If we place a tighter cut at $d < 0.5''$ we can get rid of 4 out of 14 (29%) of the SNe Ia with the new spatial cut alone.

We compare the composition of our sample selected with the initial selection criteria and the empirical cuts defined in this section in Figure 2.21. With the initial selection, we end up with a TDE contamination rate of 13:1 (left panel in Figure 2.21). By requiring $g_{\rm PTF} - R_{\rm PTF} < -0.2$ mag to remove AGNs and SNe, we achieve a contamination rate of 6:1 (middle panel in Figure 2.21). After applying

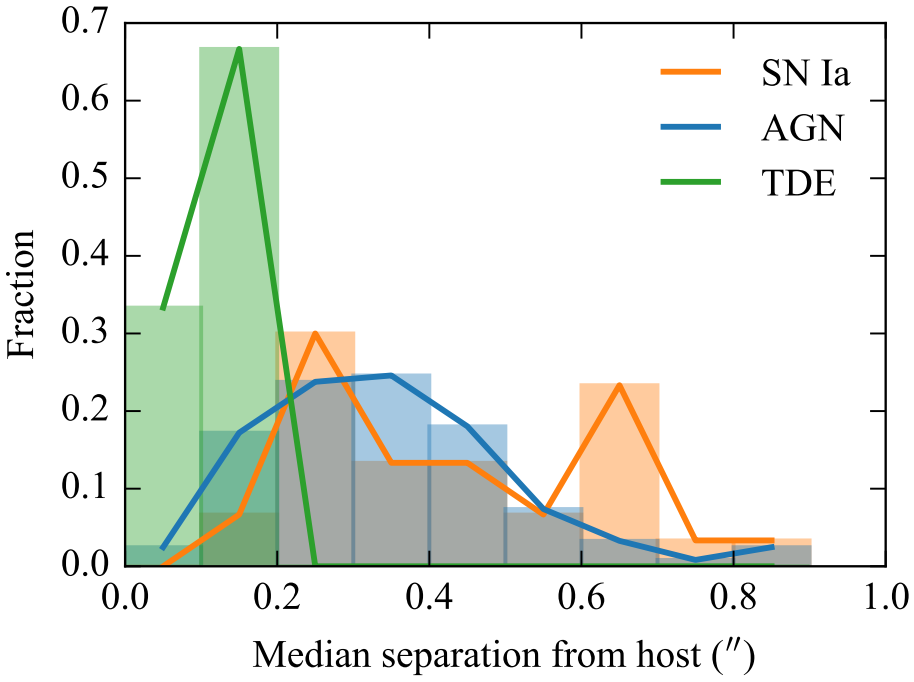

Figure 2.20: Distribution of the median flare-host separation in the first week of discovery for AGN, SN Ia, and TDEs. Another 41% of the SNe Ia can be removed from our nuclear sample if we employ a spatial cut at $d < 0.5''$.

the spatial cut at $d < 0.5''$ and host galaxy magnitude cut $r_{\rm PSF}$ <21.0 mag, our lowest TDE contamination rate is 4.5:1 (right panel in Figure 2.21).

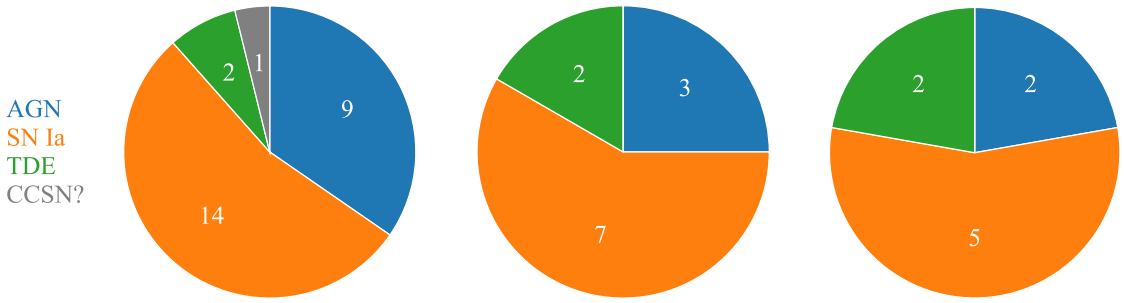

Figure 2.21: *Left*: Pie charts of the classification in the final sample of 26 sources. *Middle*: After applying the color cut $g_{\rm PTF}-R_{\rm PTF} < -0.2$, 6 AGNs and 5 SNe Ia are removed from the sample . *Right*: After applying the spatial cut $d < 0.5''$ and the host galaxy magnitude cut $r_{\rm PSF}$ <21.0 mag, we are left with 2 TDEs, 5 SNe Ia, and 2 AGNs.

2.6.4 TDE rate

The number of TDEs detected by the survey can be expressed as

$$N_{TDE} = \int \frac{d\dot{N}}{dL_g} \times \frac{4\pi}{3} D^3_{max}(L_g) \times \frac{\Delta\Omega}{4\pi} \times \tau \; dL_g \,, \tag{2.4}$$

where $d\dot{N}/dL_g$ is the luminosity function of TDEs (the volumetric TDE rate with respect to peak $g_{\rm PTF}$ band luminosity), D_{max} is the maximum distance (redshift) within which a flare can be detected by the flux-limited survey and is a function of the peak magnitude of the flare, $\Delta\Omega$ is the survey area, and τ is the duration of the survey.

We estimate the average timescale of the survey over all the fields by

$$\tau = \sum_{i=1}^{N} \Delta\tau_{max}/N\,, \tag{2.5}$$

where i is the i-th field observed by iPTF, $\Delta\tau_{max}$ is the longest baseline in the $g_{\rm PTF}$+$R_{\rm PTF}$ survey for the i-th field (right panel of Figure 2.2), and N is the total number of unique fields. For fields that are observed before and after the hiatus in summer, we use the longest τ_{max} of these two periods to represent the baseline for the field. By summing over all the unique fields, we find τ ∼44 days. Since the tidal disruption flares are luminous and long-lasting, the detection should not be sensitive to the week-long observing gaps caused by the full moon. This is true even for fast events like iPTF16fnl, which peaked at $g_{\rm PTF}$=17.07 mag and faded below 20th mag after 70 days. For iPTF16fnl-like events, which fade by 0.4 mag in the first 7 days post peak, they should remain detectable by iPTF out to $z \sim 0.05$ even in the presence of a week-long gap in the light curve.

We can solve for D_{max} by requiring the apparent magnitude of a source with a given peak luminosity νL_g being above the limiting magnitude $m_g = 20$ mag. We assume a standard blackbody temperature of $T = 3{\times}10^4$ K, which is representative for the optical TDEs, to account for K-correction. The differential flux is expressed as

$$f_\nu = \frac{(1+z)L_{\nu(1+z)}}{4\pi D_L^2(z)}, \tag{2.6}$$

where f_ν is the observed flux density, $L_{\nu(1+z)}$ is the emitted luminosity density, and D_L is the luminosity distance of the object. We then solve z by converting f_ν back to AB magnitude.

The empirical luminosity function of UV/optical selected TDEs is measured in van Velzen (2017), which can be approximated as a steep power-law where $d\dot{N}/dL_g$ $\propto L_g^{-2.5}$. The luminosity function can then be parameterized at $L_0 = 10^{43}$ erg s^{-1} as

$$\log_{10}\left(\frac{d\dot{N}}{d\log_{10}L_g}\right) = \log_{10}(\dot{N}_0) - 1.5\log_{10}\left(\frac{L_g}{L_0}\right). \tag{2.7}$$

We adopt the power-law form of luminosity function from van Velzen (2017) and substitute in the areal coverage (4792 deg^2) and timescale (τ =44 days) into Equation 2.4. We integrate Equation 2.4 from 10^{42} – $10^{43.5}$ erg s^{-1}. The lower integration limit is chosen to include iPTF16fnl, which has an observed peak luminosity of $10^{42.3}$ erg s^{-1} in g band. The upper integration limit is chosen since the luminosity bin is not well-sampled beyond $\nu L_g > 10^{43.5}$ erg s^{-1}. The only TDE in this high luminosity bin is ASASSN-15lh, which is thought to be a TDE around a rotating black hole with a mass $> 10^8$ $M_\odot$ (Leloudas et al. 2016). We also note that the nature of this event is still debated as it is also interpreted as a highly superluminous supernova in Dong et al. (2016). Our chosen luminosity range would also include iPTF16axa, which has an observed peak luminosity νL_g of 10^{43} erg s^{-1}. Low luminosity TDEs like iPTF16fnl should be harder to see in flux-limited surveys since its detection volume is almost two orders of magnitude smaller than that for events like iPTF16axa. The fact we are seeing both events may suggest a steep TDE luminosity function.

We estimate the pipeline efficiency from Frohmaier et al. (2017), where they investigated the efficiency as a function of the ratio of host galaxy surface brightness

to the flux of the flare. Since they estimated the host surface brightness by integrating the counts over a small image size that is close to the size of the PSF, we use the PSF magnitude from PS1 as a proxy for the surface brightness in our calculation. Our variability amplitude (Δm_{var}) cut already places a limit on this ratio. We are only sensitive to flares with $F_{\rm PSF,\ host}/F_{\rm PSF,\ flare} \lesssim 1.6$ since we required a $\gtrsim 60\%$ increase in the nuclear region in step 5. The median of the $F_{\rm PSF,\ host}/F_{\rm PSF,\ flare}$ ratio is ~ 0.6 in our sample after applying the Δm_{var} cut. This value corresponds to the $\approx$50% recovery fraction (Frohmaier et al. 2017, Fig 6).

After applying an efficiency factor of $\epsilon = 0.5$, the 2 TDEs discovered in the iPTF color experiment would imply a rate of $\dot{N}_0 = 1.1\ ^{+1.8}_{-0.8} \times 10^{-7}$ Mpc^{-3} yr^{-1}. We note that the volumetric rate is a lower limit because our selection is only sensitive to the red galaxies. We account for this bias when calculating the per galaxy rate as detailed below.

The volumetric rate can be converted to a per galaxy rate $\dot{n}$ by dividing the galaxy density that can be estimated from the galaxy luminosity function. We use the luminosity function derived for SDSS in Blanton et al. (2001), which has the form of a Schechter function, to calculate galaxy density (ρ) probed by iPTF. The majority (90%) of the red host galaxies with spectroscopic redshift in our sample have r band magnitudes falling in the range $-22.7 < M_r < -18.9$. Since the more massive black holes cannot produce a tidal disruption flare, we cut off the luminosity at $M_r = -21.5$ mag, which corresponds to a black hole mass of $10^8\ M_\odot$ in Tundo et al. (2007).

We also account for the fraction of red galaxies ($u - g > 1.0$ mag and $g - r >$

0.5 mag) in the luminosity range of $-21.5 < M_r < -18.9$ by querying the SDSS database. This fraction is 21% for sources within SDSS footprint (ugr) and 74% for sources with PS1 photometry (gr). Using the source number weighted fraction of 34.8%, we estimate a density ρ of 6.4×10^{-4} gal Mpc^{-3}, implying a TDE rate of $\approx 1.7\ ^{+2.9}_{-1.3} \times 10^{-4}$ TDEs gal^{-1} yr^{-1}. We compare the per galaxy rate derived in this study to the value reported from other X-ray and optical surveys Figure 2.22.

Lastly, we note that the TDE rate derived here only applies to TDEs characteristic of the known optically-selected TDE population in inactive galaxies. Our selection method of excluding AGNs and blue galaxy hosts may have the caveat of introducing a systematic error in the TDE rate since the types of TDEs associated with these galaxies are not probed in this work.

2.6.5 Prospects with ZTF

The camera mounted on P48 has been replaced with a wider FOV camera (47 deg^2) for ZTF, which is almost an order of magnitude upgrade from iPTF. Together with the reduced overhead time, ZTF will be scanning the sky at a rate of 3760 deg^2 hr^{-1}. In 2018, 40% of the ZTF operation time will be dedicated to the public survey to monitor $\sim$15000 deg^2 of the sky with a 3-day cadence with near-simultaneous $g_{\rm PTF}$ and $R_{\rm PTF}$ observations.

We define a field as visible at Palomar to have an airmass<3 for more than 3 hours in one night. The baseline of each field is $\sim$8 months. Scaling from this iPTF color experiment to the wider areal coverage and longer baseline for ZTF, we expect

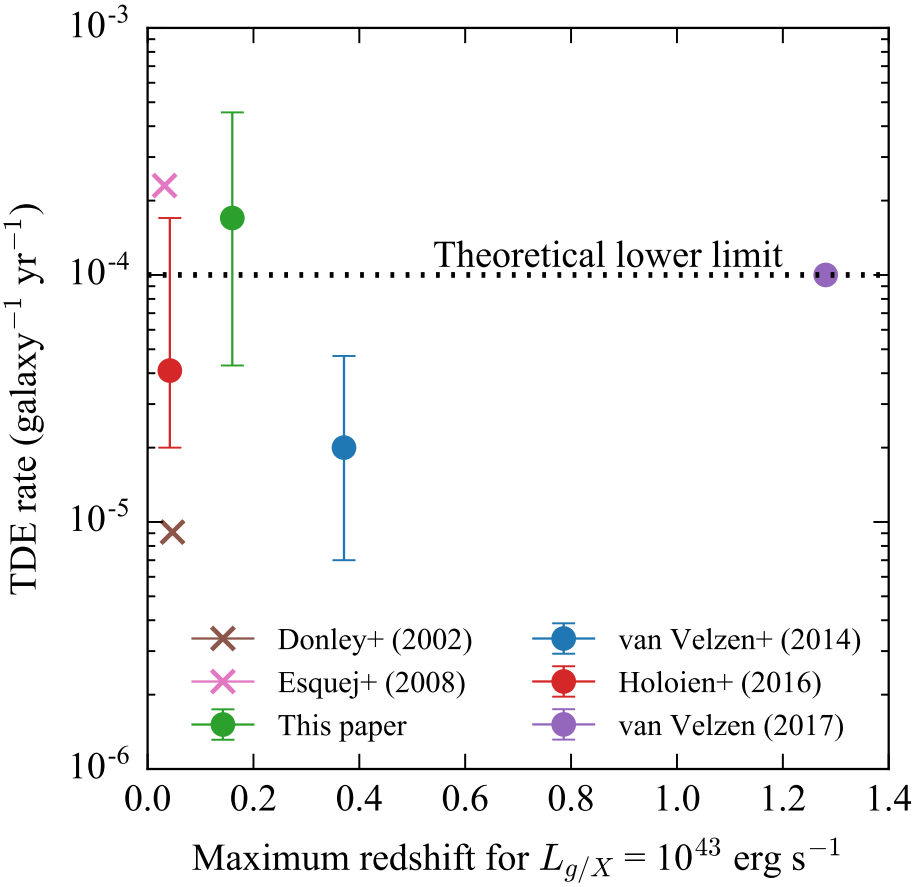

Figure 2.22: Observational rate of TDEs from X-ray (crosses) and optical (circles) surveys including SDSS+PS1 (van Velzen & Farrar 2014), ASASSN (Holoien et al. 2016b), iPTF (this paper), ROSAT All-Sky Survey (Donley et al. 2002), and XMM-Newton Slew Survey (Esquej et al. 2008). The x-axis shows the maximum redshift for each survey to detect a flare with a peak luminosity of $L_g = 10^{43}$ erg s^{-1} for optical surveys or $L_X = 10^{43}$ erg s^{-1} in 0.2–2.4keV energy band for X-ray surveys. The dotted horizontal line marks the theoretical lower limit from Wang & Merritt (2004).

to find $\sim 2 \cdot (\frac{15000}{4792})(\frac{8\text{months}}{44\text{days}}) = 32^{+41}_{-25}$ TDEs in a year.

We estimate ZTF to discover $(\frac{15000\text{deg}^2/3\text{day}}{771\text{deg}^2}) \times 6$ nuclear candidates per night = 39 nuclear candidates per night. The original selection criteria in our nuclear transient pipeline can already get rid of $\sim$ 95% of the transients, reducing the number of candidates to 2 per night.

We show the classification of the final sample in a pie chart in Figure 2.21. By employing the empirical cuts ($g_{\rm PTF} - R_{\rm PTF} < -0.2$ mag, $d < 0.5''$, $r_{\rm PSF,\ host} < 21.0$ mag) established in this paper, we are able to further reduce the number of contamination from 13:1 down to 4.5:1 (right panel in Figure 2.21). The number of nuclear transients satisfying these new criteria will be 0.7 per night for ZTF.

During the operation of ZTF, the low resolution SEDm will be entirely dedicated to spectroscopic follow up of ZTF transients that are brighter than 19 mag in $g_{\rm PTF}$. In our sample, $\sim$20% of the sources have apparent magnitudes $\lesssim$ 19.0 mag near peak, where rapid SEDm classification will be feasible. u band imaging and higher precision astrometry will also help to distinguish between SNe Ia and TDEs, leaving only the highest-confidence TDE candidates. With our selection criteria, the number of candidates that require follow up will be a manageable amount for available spectroscopic resources. With a spectroscopically complete sample of TDEs, we will be able to measure TDE luminosity function and rate that are closely connected to the physical processes leading to the disruption of stars by the central black holes of their host galaxies.

2.7 Acknowledgements

We thank the anonymous referee, Jesper Sollerman for helpful comments that improved the manuscript. S.G. is supported in part by NASA Swift Cycle 12 grant NNX16AN85G and NSF CAREER grant 1454816. These results made use of the Discovery Channel Telescope at Lowell Observatory. Lowell is a private, non-profit institution dedicated to astrophysical research and public appreciation of astronomy and operates the DCT in partnership with Boston University, the University of Maryland, the University of Toledo, Northern Arizona University and Yale University. The W. M. Keck Observatory is operated as a scientific partnership among the California Institute of Technology, the University of California, and NASA; the Observatory was made possible by the generous financial support of the W. M. Keck Foundation. This research used resources of the National Energy Research Scientific Computing Center, a DOE Office of Science User Facility supported by the Office of Science of the U.S. Department of Energy under Contract No. DEAC02-05CH11231.

Table 2.1. Sample composition after each filtering step

Selection	all	Host color		Known	Historical	$\lvert\Delta m_{var}\rvert$		$g_{\rm PTF}-R_{\rm PTF}$		Peak mag	
		blue	red	AGN	Detection	$\geq$0.5	$\leq$0.5	$\leq$0	$\geq$0	$\leq$20	$\geq$ 20
Nuclear	493	216	267	37	94	249	235	200	203	285	206
Extended host	375	150	225	31	62	189	186	158	157	221	154
Red host	225	···	225	12	37	81	144	78	105	136	89
Not known AGN	200	···	200	···	37	78	122	72	95	119	81
No variability history	163	···	163	···	···	69	94	62	73	90	73
$\lvert\Delta m_{var}\rvert > 0.5$	69	···	69	···	···	69	···	33	30	46	23
Blue flare	33	···	33	···	···	33	···	33	···	26	7

Table 2.2. Applying selection criteria on previously reported TDEs.

Name	ext	red host	Not AGN	No variability	Δm_{var}	$g-r$
SDSS-TDE1	Y	Y	Y	Y	-0.27[1]	-0.32
SDSS-TDE2	Y	Y	Y	Y	-0.73	-0.31
ASASSN-14ae	Y	Y	Y	Y	-0.54	-0.27
ASASSN-14li	Y	Y	Y	Y	-1.20	-0.41[3]
PS16dtm	Y	Y	N	Y	-2.75	-0.16
PS1-11af	Y	Y	Y	Y	-0.98	-0.30
PS1-10jh	Y	Y[2]	Y	Y	-1.21	-0.31
PTF09ge	Y	Y	Y	Y	-1.25	-0.25
PTF09axc	Y	Y	Y	Y	-0.52	-0.04[3]
PTF09djl	Y	Y	Y	Y	-0.97	-0.24[3]

[1]Peak is not resolved in the light curve of TDE1.

[2]Deeper u band imaging confirms the host galaxy color of PS1-10jh satisfy $u-g>1$ mag.

[3]Since PTF09axc and PTF09djl only have single band light curve, we derive their observed $g-r$ by convolving a redshifted blackbody spectrum with the minimal best-fit temperatures reported in Arcavi et al. (2014) with the $g_{\rm PTF}$ and $R_{\rm PTF}$ response functions and adding in the Galactic extinction. The same is done for ASASSN-14li since the published g and r photometry include contribution from the host galaxy.

Table 2.3. Photometric properties of the final sample

Object	z	$m_{peak,g}$	$M_{peak,g}$	Δm_{var}	g-r	Classification	Instrument[1]
iPTF16axa[s]	0.108	19.44	-19.08	-1.16	-0.45	TDE	DEIMOS
iPTF16ayd	0.171	19.54	-20.06	-0.54	-0.01	AGN	LRIS
iPTF16bcp[s]	0.14[f]	19.55	-19.57	-3.10	-0.19	SN Ia	DEIMOS
iPTF16bjy	0.128	19.65	-19.27	-0.52	-0.20	SN Ia phot	
iPTF16bke	0.15[f]	19.25	-20.01	-0.72	-0.28	SN Ia	LRIS
iPTF16bko	0.085	18.74	-19.22	-1.09	-0.10	SN Ia phot	
iPTF16bmy	0.129	19.94	-18.99	-1.04	-0.14	CCSN?	
iPTF16fhs	0.110	19.08	-19.48	-0.81	-0.12	AGN phot	
iPTF16fjc	0.449	19.56	-22.45	-2.01	-0.11	AGN phot	
iPTF16fjg	0.14[f]	19.3	-19.83	-0.88	-0.23	SN Ia	SEDM
iPTF16fly	0.349	18.38	-22.99	-1.25	-0.24	AGN phot	
iPTF16fmc	0.139	19.37	-19.75	-1.09	-0.34	SN Ia phot	
iPTF16fmd[s]	0.151	19.75	-20.05	-1.86	-0.17	SN Ia phot	
iPTF16fnl[s]	0.016	17.06	-17.21	-0.78	-0.22	TDE	SEDM
iPTF16fpt	0.160	19.52	-19.93	-0.75	-0.12	AGN phot	
iPTF16fqa[s]	0.125	19.1	-19.76	-0.51	-0.21	AGN	SEDM
iPTF16fsc	0.167	19.23	-20.30	-0.64	-0.02	SN Ia phot	

Table 2.3 (cont'd)

Object	z	$m_{peak,g}$	$M_{peak,g}$	Δm_{var}	g-r	Classification	Instrument[1]
iPTF16fzx	0.125	19.73	-19.13	-0.60	-0.10	AGN phot	
iPTF16glz	0.03[f]	16.91	-18.7	-5.16	-0.25	SN Ia	SEDM
iPTF16gyl[s]	0.112	19.82	-18.78	-0.79	-0.08	SN Ia phot	
iPTF16hcn	0.130	19.59	-19.36	-0.99	-0.28	SN Ia phot	
iPTF16hma[s]	0.391	19.48	-22.18	-1.35	-0.20	AGN phot	
iPTF16hrx	0.105	19.29	-19.16	-0.51	-0.28	SN Ia phot	
iPTF16ijw	0.07[f]	18.15	-19.36	-1.25	-0.20	SN Ia	SEDM
iPTF16ijz	0.151	19.56	-19.73	-0.71	-0.23	AGN phot	
iPTF16isi	0.092	19.45	-18.67	-0.75	-0.30	SN Ia phot	

[1]Objects for which no classification spectrum was taken are left blank.

[s]Has *Swift* $uvw2$ photometry. Results are summarized in Table 2.6.

[f]Redshift derived from SNID fit to the flaring SN Ia spectra.

Table 2.4: Best-fit parameters to the SALT2 model

Object	χ^2_ν	redshift	t_0	x_0 ($\times 10^{-4}$)	x_1	c
iPTF16bcp	1.03	0.14	57545.6	2.47	1.86	-0.137
iPTF16bke	4.62	0.15	57558.4	2.57	1.87	-0.162
iPTF16fjg	1.54	0.14	57627.4	3.2	0.83	-0.217
iPTF16glz	2.13	0.03	57664.8	36.67	0.98	-0.024
iPTF16ijw	1.73	0.07	57722.1	10.55	2.66	-0.005
iPTF16bjy	1.70	0.128	57550.1	2.0	3.51	-0.140
iPTF16bko	0.49	0.085	57549.1	6.02	1.29	-0.086
iPTF16fmc	0.89	0.139	57639.4	3.15	2.52	-0.108
iPTF16fmd	1.05	0.151	57637.7	2.26	1.18	-0.082
iPTF16fsc	2.07	0.167	57641.4	1.31	6.18	0.021
iPTF16gyl	2.48	0.112	57672.9	1.93	0.37	-0.006
iPTF16hcn	5.18	0.130	57670.6	2.64	-0.17	-0.096
iPTF16hrx	1.62	0.105	57699.5	2.99	-1.04	-0.077
iPTF16isi	1.88	0.092	57725.5	2.8	1.88	-0.185

Table 2.5. Observations of the host galaxies of the photometrically classified sources

Object	z	Date	Telescope	Host class[1]	FWHM$_{H\beta}$ (km s^{-1})
iPTF16bjy	0.128	2017-09-15	DCT Deveny	broad line AGN	6199.0
iPTF16bko	0.085	2017-09-15	DCT Deveny	early-type galaxy	···
iPTF16bmy	0.129	2017-07-29	P200 DBSP	early-type galaxy	···
iPTF16fhs	0.110	2017-09-15	DCT Deveny	AGN	···
iPTF16fjc	0.449	2017-09-17	DCT Deveny	broad line AGN	4086.3
iPTF16fly	0.349	2017-09-15	DCT Deveny	broad line AGN	4633.2
iPTF16fmc	0.139	2017-07-29	P200 DBSP	starforming	···
iPTF16fmd	0.151	2017-07-29	P200 DBSP	AGN	···
iPTF16fpt	0.160	2012-06-29	SDSS(host)	AGN	···
iPTF16fzx	0.125	2017-09-15	DCT Deveny	starforming	···
iPTF16gyl	0.112	2017-09-17	DCT Deveny	AGN	···
iPTF16hcn	0.130	2017-09-16	DCT Deveny	AGN	···
iPTF16hma	0.391	2017-07-31	P200 DBSP	broad line AGN	4419.3
iPTF16hrx	0.105	2017-09-15	DCT Deveny	starforming	···
iPTF16ijz	0.151	2017-09-15	DCT Deveny	AGN	···
iPTF16isi	0.092	2017-09-15	DCT Deveny	starforming	···

[1]Host galaxies are classified based on the [OIII]/Hβ versus [NII]/Hα diagnostic diagram.

Table 2.6. *Swift* observations of the sample

Object	Phase	UVW2[1]	GALEX NUV	XRT	z	$m_{peak,g}$	$m_{peak,r}$	Class	Δm_{var}
	days	mag	mag	erg s^{-1}cm^{-2}					
iPTF16axa	8.7[d]	18.77 ±0.05	···	$<1\times10^{-14}$	0.108	19.44	19.99	TDE	-1.16
iPTF16bcp	1.7[d]	>22.60	···	$<3.3\times10^{-13}$	0.14	19.55	19.77	SN Ia	-3.10
iPTF16fmd	3.8	>22.02	···	$<4.1\times10^{-13}$	0.151	19.75	19.62	SN Ia phot	-1.86
iPTF16fnl	0.6	16.32 ±0.03	19.57	$4.6^{+3.6}_{-2.0}\times10^{-15}$	0.016	17.06	17.23	TDE	-0.78
iPTF16fqa	13.8[d]	19.23 ±0.06	20.59	$<2.7\times10^{-13}$	0.125	18.77	18.87	AGN	-0.51
iPTF16gyl	8.5	22.03 ±0.31	22.81	$<2.7\times10^{-13}$	0.112	19.82	19.35	SN Ia phot	-0.79
iPTF16hma	69.5[d]	19.78 ±0.08	···	$<5.9\times10^{-13}$	0.391	19.47	19.65	AGN phot	-1.35

[1]Galactic extinction correction applied.

[d]If the peak is not clearly sampled in the light curve, we list Δt since iPTF discovery instead.

Chapter 3: Revisiting Optical Tidal Disruption Events with iPTF16axa

3.1 Introduction

While the properties of X-ray TDEs are roughly consistent with the theoretical expectations for radiation powered by mass accretion in the TDE debris disk, the discovery of optical TDEs has challenged this simple picture. Not only do they have a much lower temperature than expected, but the lack of temperature evolution in tandem with the decreasing accretion rate is also in disagreement with thermal radiation from the debris disk. Many studies have tried to resolve this discrepancy by considering several mechanisms that could lead to the observed signature. For example, the production of an optically thick envelope that radiates at the Eddington limit (Loeb & Ulmer 1997), or a strong disk wind or outflow that regulates the accretion rate (Strubbe & Quataert 2009; Miller 2015; Metzger & Stone 2016). Alternatively, elliptical accretion may cause energy lost to the black hole before circularization, resulting in 1%-10% of the bolometric efficiency of a standard accretion disk (Svirski et al. 2017).

Another weakness in the classical picture of TDEs is debris circularization, which was assumed to happen immediately when the debris returns to pericenter (R_p) (Rees 1988). Recent work by Shiokawa et al. (2015) has shown that orbital

energy cannot be dissipated efficiently at r$\sim R_p$ and therefore the circularization process does not happen as quickly as previously thought. Instead, stream-stream collisions are thought to play an important role in producing shocks that convert kinetic energy into thermal energy (Kochanek 1994). In Dai et al. (2015), the extent of apsidal precession that causes different distances of self-intersection of the tidal debris from the supermassive black hole was proposed to explain why there exists two populations of TDE temperatures. Hydrodynamical simulations also suggest that stream-stream collisions may be responsible for the observed UV/optical emission of TDEs (Piran et al. 2015; Shiokawa et al. 2015; Bonnerot et al. 2017; Jiang et al. 2016).

The method for photometric selection of TDEs in optical transient surveys was demonstrated in an archival study of the SDSS Stripe 82 Survey by van Velzen et al. (2011), and resulted in the recovery of two likely TDE candidates. Since then, on the order of a dozen of optical TDEs have been discovered promptly enough for spectroscopic follow-up observations, and they show a diversity of broad hydrogen and helium emission line strengths. For example, the optical spectra of PS1-10jh, PTF09ge, and ASASSN-15oi display broad HeIIλ4686 emission lines with no sign of Hα emission, ASASSN-14li shows both broad prominent HeII and Hα emission, and ASASSN-14ae has strong Hα emission and a weaker but broad HeIIλ4686 that developed later in time. The spectral family of TDEs was first discussed in Arcavi et al. (2014). The mechanisms behind the spectroscopic signatures are still under debate. Proposed explanations include the chemical composition of the progenitor star (Gezari et al. 2012), and photoionization conditions in the debris disk (Guillo-

chon et al. 2014) or an optically-thick reprocessing envelope (Roth et al. 2016).

The paper is structured as follows. In §3.2 we present the discovery of a newly discovered optical TDE candidate iPTF16axa. We describe the pre-event data associated with its host galaxy in §3.3 and the follow up photometric and spectroscopic observations we obtained for iPTF16axa in §3.4. The results of SED and spectral analyses are presented in §3.5. In §3.6, we compare the physical quantities derived from the SEDs and the spectral measurements with 11 UV/optical events that are classified as strong TDE candidates with well-sampled optical light curves.

3.2 Discovery of iPTF16axa

iPTF16axa (right ascension, α_{J2000} = 17h03m34.36s; declination, σ_{J2000} = +30°35'36.8") is a TDE discovered by the intermediate Palomar Transient Factory (iPTF) using the Palomar 48-inch (P48) telescope. The flare was first detected on UT 2016 May 29 (UT dates are use throughout the paper) with a host flux subtracted magnitude of g =19.49 ± 0.07 mag. Astrometrically aligned P48 images show that the position of the flare is coincident with the nucleus of the host galaxy, with an offset of 0.17 arcsec that is within the positional uncertainties measured for a reference AGN sample of 0.3 arcsec. Constraints on the peak time are not available since the field is not regularly monitored by iPTF. However, the PTF survey visited this field in 2011 Mar-Sep, 2012 Mar, 2013 Aug, and 2014 May-Jun. No historical variability activity was detected to a 3σ limiting magnitude of R ≈ 21 mag in any observations during the aforementioned period, which indicates that the source of

the flare is unlikely to be caused by a variable active galactic nucleus (AGN).

We requested target-of-opportunity (ToO) observation of iPTF16axa on 2016 June 01 using our Cycle 12 *Swift* key project (PI Gezari) triggers that are designed for a systematic follow up of iPTF nuclear transients with red host galaxies. The transient satisfies our selection criteria: observations made with the Palomar-60 inch (P60) telescope shows the transient has a blue color ($g-r \sim -0.4$ mag) and is found in a red host galaxy ($u-g$=1.94 mag and $g-r$=0.91 mag) as is revealed by the Sloan Digital Sky Survey Data Release 9 (SDSS DR9).

The observation made with the *Swift* satellite on Jun 07 2016 using the UV-optical telescope (UVOT) in the *uvw2* filter showed signs of a UV bright source. After triggering the Swift ToO observation, a classification spectrum was also taken with Keck DEIMOS on 2016 June 04. The classification spectrum shows conspicuous broad HeIIλ4686 line as well as Hα emission lines at $z = 0.108$ that are indicative of TDEs discovered in the optical. However, a simultaneous *Swift* X-Ray Telescope (XRT) observation did not show any sign of X-ray emission in 0.3–10keV. A VLA observation made on June 12 also resulted in null detection with a rms of 13 μJy at 6.1 GHz and 15 μJy at 22 GHz. With the Swift UVOT photometry and the classification spectrum confirming iPTF16axa being a strong TDE candidate, we triggered a series of follow up programs in the UV and optical over a span of three months until the target was not observable by ground-based telescopes.

3.3 Archival Data

The celestial position of iPTF16axa was covered by SDSS. A galaxy associated with this position, SDSS J170334.34+303536.6, has photometry measurements in *ugriz*. However, no spectroscopy is found to be associated with the host galaxy.

Archival AllWISE data (Cutri & et al. 2013) shows that the host galaxy was observed with 15.8 mag, 15.5 mag, <11.7 mag, and <9.4 mag in 3.4, 4.6, 12, and 22 μm, respectively, in the Vega system. Pre-event GALEX or ROSAT limits of the host galaxy are not available.

3.3.1 Host galaxy properties

Due to the long-lived nature of TDE, we were not able obtain a host galaxy spectrum of iPTF16axa for this analysis before it went behind the Sun in October.

We perform synthetic stellar population template fitting to the SDSS broad-band photometry `cmodelMag` in *ugriz* as well as the WISE 3.4 μm and 4.6 μm photometry with Fitting and Assessment of Synthetic Templates (`FAST`) by Kriek et al. (2009). Assuming an exponentially declining star formation history with the Bruzual & Charlot (2003) templates, a Salpeter IMF, the Cardelli et al. (1989) dust extinction law, and A_V=0.12 from the Schlafly & Finkbeiner (2011) dust map, the fitting program yields a χ^2_ν of 1.57. The results of the fit suggest that star formation has quenched in the galaxy with an SFR of $10^{-6.6}$ $M_\odot$ yr^{-1}. In February 2017, we obtained a high-resolution spectrum of iPTF16axa with the Echellette Spectrograph and Imager (ESI) mounted on the Keck-II telescope (PI Gezari). We observed the

host galaxy and a template GIII star BD+332423 with the 0.5" slit for a total integration time of 3600s and 120s, respectively. The data is reduced with the MAuna Kea Echelle Extraction (`MAKEE` [1]) package while the wavelength is calibrated with `IRAF`.

We measure a stellar velocity dispersion of 101.3±1.9 kms^{-1} with the Mg I*b* $\lambda\lambda$5167, 5173, 5184 triplet (Figure 3.1) by broadening the GIII stellar template to match the linewidths in the host spectrum. The velocity dispersion translates to a black hole mass of $5.0^{+7.0}_{-2.9}\times$ 10^6 $M_\odot$ (McConnell & Ma 2013). Despite the large intrinsic scatter in the M-σ relation (0.38 dex), the black hole mass estimated from velocity dispersion is within the range of allowable black hole masses able to disrupt a solar-type star outside of its event horizon.

3.4 Follow-Up Observations

3.4.1 Photometry

The follow-up photometric observations of iPTF16axa are described in this section. These measurements are presented in Table 3.3.

3.4.1.1 P48 and P60 photometry

On 2016 May 29, the transient iPTF16axa was discovered in the g band while iPTF conducted a seasonal experiment that searches for young supernovae using the P48 telescope in Mould-R and SDSS-g' filters to a depth of ∼20.5 mag with a

[1] http://www.astro.caltech.edu/ tb/makee/

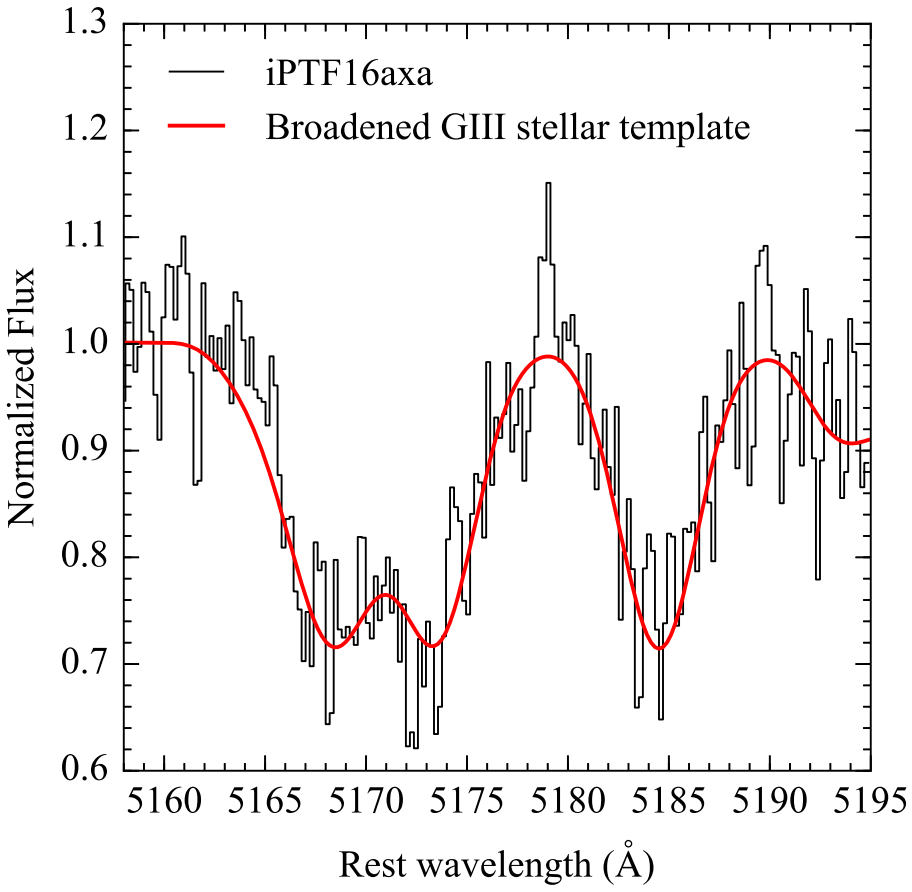

Figure 3.1: Spectral fit around the Mg I*b* triplet region. The black line shows the Keck ESI spectrum of the host galaxy of iPTF16axa. The red line marks the Keck ESI spectrum of a GIII star BD+332423 that has been broadened to fit the absorption linewidths in the host.

4 day cadence. The nightly P48 raw images are detrended and astrometrically and photometrically calibrated at the Infrared Processing and Analysis Center (IPAC) (Laher et al. 2014). Following the discovery of the transient, we requested a series of observations of the source in *gri* bands with the robotic Palomar 60-inch telescope in order to keep track of the color evolution. The collected data are processed by the Fremling Automated Pipline (Fremling et al. 2016) that performs image subtraction with respect to the SDSS images and extracts the PSF magnitude of the source.

3.4.1.2 LCO photometry

We obtained 6 epochs of the Las Cumbres Observatory (LCO) follow-up photometry in *gri* bands. Host flux subtraction is performed using SDSS references. The LCO light curves are consistent with the P60 data but have larger error bars due to cross subtractions of LCO and SDSS. Therefore, the LCO data are not included in the light curve fit in subsection 3.5.1. The LCO subtractions may be improved once the LCO references are obtained.

3.4.1.3 *Swift* UVOT and XRT photometry

Following the discovery of TDE emission signatures from the spectroscopy, we requested and were granted 13 target-of-opportunity observations spanning a time period of $\sim$ 2.5 months with *Swift*. The observations were made in all 6 filters of UVOT: UVW2 (1928 Å), UVM2 (2246 Å), UVW1 (2600 Å), U (3465 Å), B (4392 Å), and V (5468 Å). We used a 5" radius aperture and a 20" background region

to extract the photometry of the UV source with the task `uvotsource` in HEASoft [2]. Note that due to the lack of pre-event UV limits, we do not attempt to perform host subtraction with the UVOT images.

We also observed the location of iPTF16axa with the XRT (Burrows et al. 2005) on-board the *Swift* satellite Gehrels et al. (2004) beginning at 4:32 UT on 7 June 2016. Regular monitoring of the field in photon counting (PC) mode continued for the next 10 weeks.

No significant emission is detected in individual epochs. Using standard XRT analysis procedures (e.g., Evans et al. 2009), we place 90% confidence upper limits ranging from (2.9–12.0) $\times 10^{-3}$ counts s^{-1} in the 0.3–10.0 keV bandpass over this time period. Stacking all the XRT data obtained over this period together (29 ks of total exposure time) also results in an upper limit of 2.7×10^{-4} counts s^{-1}.

To convert this count rate to a flux, we adopt a power-law spectrum with a photon index of $\Gamma = 2$ and incorporate absorption from the Milky Way (but none in the TDE host galaxy). We then find an upper limit on the time-averaged unabsorbed X-ray flux from the location of iPTF16axa of $< 1.1 \times 10^{-14}$ erg cm^{-2} s^{-1} (90% confidence limit). At the distance of iPTF16axa, this corresponds to a 0.3–10.0 keV X-ray luminosity of $L_X < 3.3 \times 10^{41}$ erg s^{-1}. While this limit is significantly fainter than the luminous X-ray emission observed from ASASSN-14li (Holoien et al. 2016b; van Velzen et al. 2016b), it is comparable to the much fainter emission observed from ASASSN-15oi ($L_X = 4.8 \times 10^{41}$ erg s^{-1}; Holoien et al. 2016a). And it is several orders of magnitude above the faint X-ray emission observed at the

[2] `https://heasarc.gsfc.nasa.gov/lheasoft/`

location of iPTF16fnl ($L_X = 2.4 \times 10^{39}\,\mathrm{erg\,s^{-1}}$; Blagorodnova et al. (2017a)).

3.4.2 Spectroscopy

3.4.2.1 Keck DEIMOS

A Keck DEIMOS classification spectrum was scheduled 3 days after the first *Swift* ToO observation was triggered (Jun 04 2016). The spectrum was taken with a 0.8" wide slit along with the LVMslitC slit mask and a 600ZD grating. The on-source exposure time was 360s. The data was reduced using the DEIMOS DEEP2 data reduction pipeline with flux calibrated by the spectrum of a spectrophotometric standard star, BD+28d4211, taken on the same night.

3.4.2.2 Keck LRIS

Keck LRIS spectra were taken on Jun 10 2016 and Jul 06 2016. Same configuration were used and the integration time was 900s in both nights. The spectra were taken with a 1" slit and a 400/3400 grism that yields a FWHM resolution of ∼7 Å. The data were reduced with the LRIS automated reduction pipeline [3]. The observed flux standard star is BD+28d4211.

3.4.2.3 DCT DeVeny

An exposure of iPTF16axa was taken on Jun 13 with the 4.3-meter DeVeny spectrograph mounted on the Discovery Channel Telescope (DCT). A 1.5" slit and

[3] `http://www.astro.caltech.edu/~dperley/programs/lpipe.html`

a 300g/mm grating were used with a central wavelength setting of 5800 Å. The spectral coverage is 3600-8000 Å at a dispersion of ∼2.2 Å per pixel, yielding a FWHM resolution of ∼9 Å. Data were reduced with standard IRAF routines, which include bias removal, flat-fielding, 1-d spectrum extraction, wavelength calibration and flux calibration using spectrophotometric standard star BD+40d4032.

3.5 Analysis

Throughout this paper, we correct for Galactic extinction for all data used for analysis using the Cardelli et al. (1989) extinction curve with $R_C = 3.1$ and $E(B-V) = 0.0390$ based on Schlafly & Finkbeiner (2011) dust map. We use a luminosity distance of $d_L = 505$ Mpc based on a WMAP9 cosmology with $H_0 = 69.32$ km s^{-1} Mpc^{-1} , $\Omega_M = 0.29$, $\Omega_\Lambda = 0.71$.

3.5.1 Light curves

Classical calculations assume a uniform distribution in specific energy so that the bound stellar debris returns to the pericenter at a rate of $t^{-5/3}$ (Rees 1988; Phinney 1989). For more realistic energy distributions, there are deviations from $t^{-5/3}$ at early times, but the light-curve eventually approaches a $t^{-5/3}$ power-law at late times (Lodato et al. 2009), or approaches a power-law index within a range of values that brackets -5/3 (Guillochon & Ramirez-Ruiz 2013). The $t^{-5/3}$ power-law can be expressed as

$$L(t) \propto \dot{M}(t) \propto (t - t_D)^{-5/3}, \tag{3.1}$$

where t_D is the time of disruption. We fit the light curves in both g and r bands simultaneously with data taken by P48 and P60 telescopes. With a fixed power-law index of -5/3, we can rewrite Equation 3.1 to

$$m_{obs} = N + \frac{5}{2} \cdot \frac{5}{3}(t - t_D), \tag{3.2}$$

where m_{obs} is the observed magnitude and N is a normalization constant. We derived a disruption time (t_D) of MJD 57482.9±1.1 using `emcee` (Foreman-Mackey et al. 2013), a python implementation of the Affine invariant Markov chain Monte Carlo (MCMC) ensemble sampler. The corner plot for 1000 MCMC simulations is shown in Figure 3.2. If we loosen the fitting parameter constraints further by allowing the power law index to change freely, we obtain a best-fit power-law index of -$1.44^{+0.09}_{-0.12}$ and a t_D of 57494.7±0.1. The derived values imply the rise time to peak light is shorter than 49 rest-frame days assuming the peak was reached some time before the discovery of iPTF16axa.

The light curve is fitted well by a $t^{-5/3}$ power-law in all the UV and optical bands, with a constant color between the bands with time. The model fit shown in Figure 3.3 has the colors $UVW2 - r = -1.05$ mag and $g - r = -0.34$. The lack of color evolution and the observed $t^{-5/3}$ power-law decline in the UV and optical bands requires a fixed temperature over time to be consistent with the expected $t^{-5/3}$ evolution of the bolometric luminosity.

In Figure 3.4, we show the best-fit blackbody spectrum implied by these colors using the magnitudes extrapolated from the power-law in Figure 3.3 to the time of discovery MJD 57537.4 in $UVW2$, $UVM2$, $UVW1$, u, g, r, and i bands. The best-

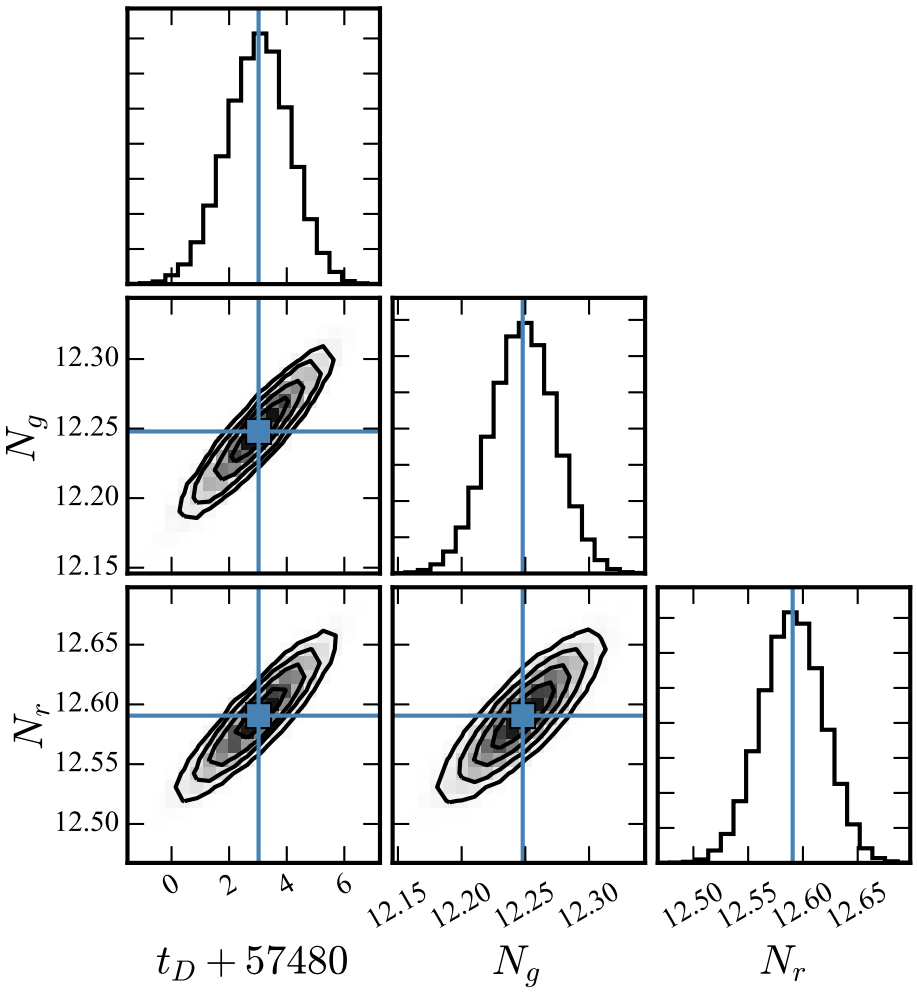

Figure 3.2: Corner plot of the light curve fit, which contains 1000 MCMC simulations.

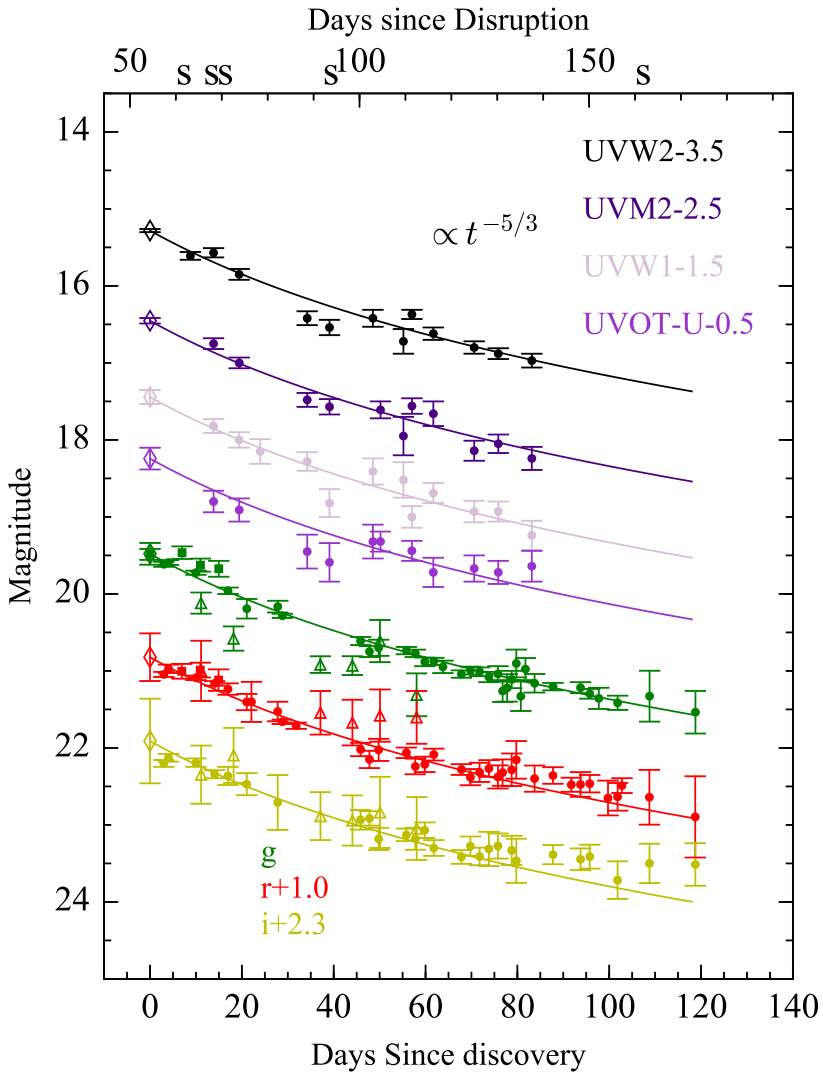

Figure 3.3: The light curve of iPTF16axa with a $t^{-5/3}$ power law fit and dates normalized to the derived disruption time MJD57482.9. The circles and squares for *gri*bands denote the host-subtracted data taken with P60 and P48 respectively while the diamonds are the extrapolated magnitudes at the time of iPTF discovery. The open triangles in *gri* bands mark the LCO host-subtracted magnitudes. Note that the LCO data are not included in the light curve fit since they the cross subtractions of LCO data and SDSS result in larger error bars.

fit blackbody temperature implied by the light curve model is 2.85×10^4 K. Using the X-ray upper limit, we also place an upper limit of 1.85×10^5 K on the blackbody temperature of the TDE, which is shown in the green dashed line in Figure 3.4.

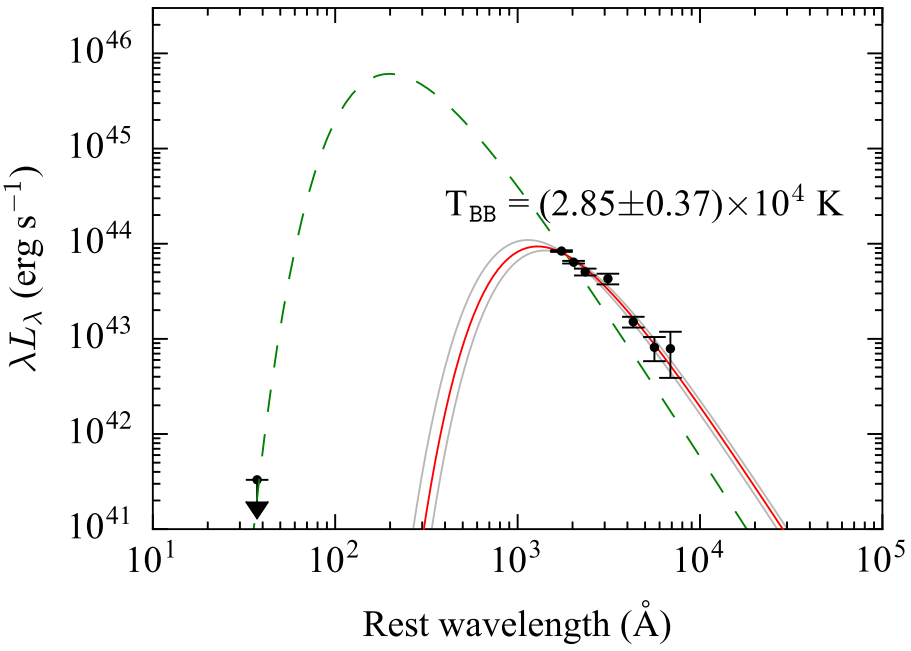

Figure 3.4: Blackbody fit of the UV-optical SED derived from the $t^{-5/3}$ power-law fit in subsection 3.5.1 extrapolated to t_{disc}= MJD 57537.4. The grey curves show the highest and lowest temperatures bounded by the 90% confidence interval. The green curve shows the blackbody spectrum corresponding to T_{bb}=1.85×10^{5}K, which is an upper limit on the temperature imposed by the stacked *Swift* XRT flux in 0.3keV-10keV.

3.5.2 SED analysis

Given the archival SDSS u band magnitude of the host is $\sim$ 21.4 mag, we assume the host light contribution is negligible in UVOT filters with shorter wavelengths ($UVW2, UVM2, UVW1, u$). The data in B and V bands are excluded for data analysis since the contribution from the host galaxy is unknown. We also collected the host-subtracted photometry in gri from P48 and P60, which use images from IPAC and SDSS as references, respectively.

To construct UV-optical SEDs at different epochs, we interpolate the host-subtracted flux in g and r bands using the $t^{-5/3}$ light curves in Figure 3.3 to the epoch of *Swift* observations. The uncertainties of the interpolated magnitudes in g and r are estimated to be the weighted residual of the light curve fit with the $t^{-5/3}$ power law.

The SEDs are fit with a blackbody using Markov chain Monte Carlo (MCMC) method. Shown in Figure 3.5 are the best-fit blackbody spectra. The 1σ uncertainties of the model parameter are shown by the two grey lines in each panel, representing the upper and the lower bound of the best-fit temperature. The best-fit blackbody temperatures are plotted as a function of time in the top panel of Figure 3.6. The blackbody temperatures of iPTF16axa remained nearly constant temperature $\bar{T}$=(3.0$\pm$0.33)$\times10^4$K over 80 days of the *Swift* monitoring.

In Figure 3.6, we also plot the time evolution of the UV-optical integrated luminosity and the blackbody radius in the middle and the bottom panels. We calculate the luminosity by integrating the area under the best-fit blackbody for

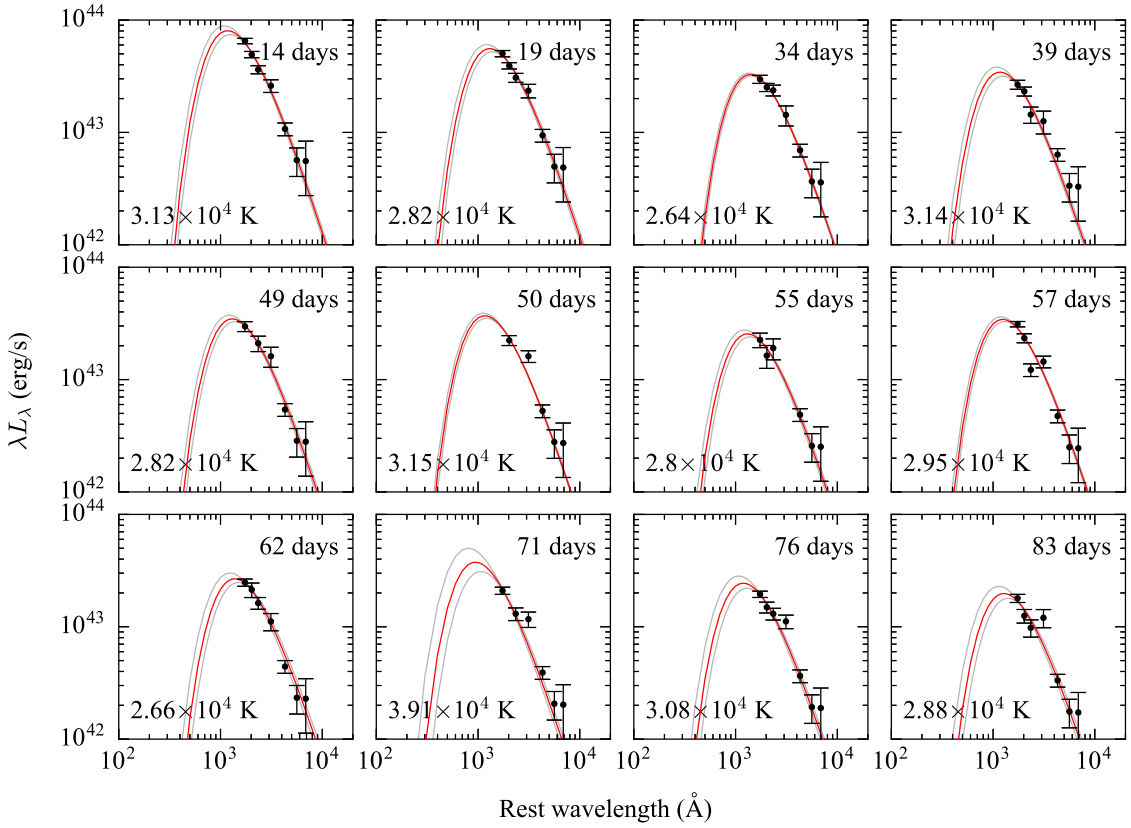

Figure 3.5: The blackbody fit for the transient SEDs. The time indicated in each panel shows the time elapsed since discovery t_{disc} = MJD 57537.4. The blackbody temperature remains roughly constant with a mean temperature $3{\times}10^4$K over time.

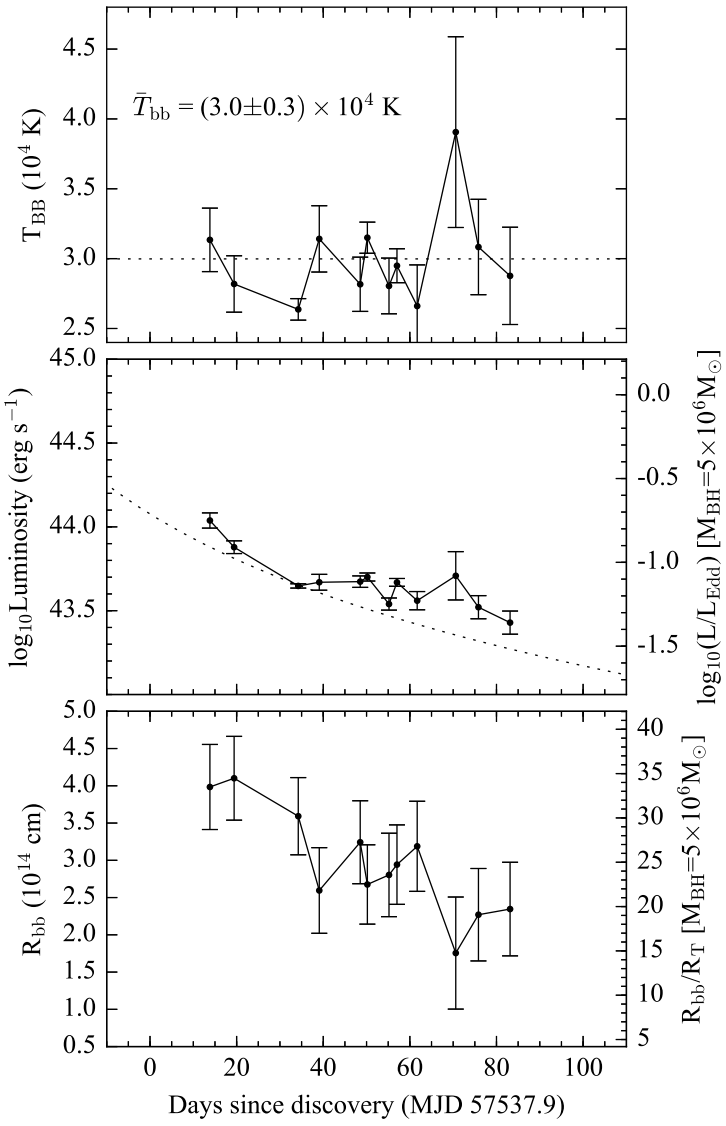

Figure 3.6: The time evolution of iPTF16axa. Upper: The time evolution of blackbody temperature of iPTF16axa. The black dotted line marks the mean T_{bb} of 3×10^4 K. Middle: The evolution of integrated UV-optical luminosity. The black dotted line shows the $t^{-5/3}$ prediction from the light curve with a peak luminosity indicated in Figure 3.4. Total power emitted (Area under the dotted line integrated from t_{disc} to t_∞) is 5.5×10^{50} ergs. Lower: The time evolution of the blackbody radius inferred from SED fitting.

each SED, which follows the theoretical $t^{-5/3}$ law. Given there is no detection in the X-ray, we assume the bolometric luminosity of the transient is dominated by the emission in the UV and optical. The observed peak luminosity of 1.1×10^{44} erg s^{-1} corresponds to an Eddington ratio of 17.4% for a $5{\times}10^6$ $M_\odot$ black hole and a mass accretion rate ($\dot{M}_0$) of $1.8{\times}10^{-2}$ $(\epsilon/0.1)^{-1}$ $M_\odot$ yr^{-1}, where ϵ is the accretion efficiency. The total energy integrated under the model fit from from t_{disc} to t_∞ is $5.5{\times}10^{50}$ erg, which corresponds to a total mass accreted of $3.1{\times}10^{-3}$ $(\epsilon/0.1)^{-1}$ $M_\odot$. Note, that this is a small fraction of the $0.5M_\star$ of mass expected to remain bound to the black hole in a TDE (Rees 1988) unless the radiative efficiency (ϵ) is low .

We also calculate the emitting radius of the blackbody using the Stefan-Boltzmann law:

$$L = 4\pi R_{bb}^2 \sigma T_e^4, \tag{3.3}$$

where L is the luminosity integrated from the best-fit blackbody spectrum to the SED, R_{bb} is the blackbody radius, and T_e is the effective temperature, which is set to be equal to the blackbody temperature derived from the SED fit. In Table 3.1 we list our fits for the blackbody temperature, luminosity, and photospheric radius for each of our photometric observations. In the bottom panel of Figure 3.6, we plot our fit for the photospheric radius as a function of time, where the y-axis on the right hand side of Figure 3.6 shows the radius in units of the tidal radius (R_T) assuming the disrupted star is a solar mass star. The tidal radius, $R_T = R_\star(M_{\rm BH}/M_\star)^{1/3}$, is $1.19{\times}10^{13}$ cm for a $5{\times}10^6 M_\odot$ black hole.

3.5.3 Spectral analysis

Five follow up spectra are shown in Figure 3.7. We also show the best-fit host spectrum from `FAST` fit with SDSS `fiberMag` (flux enclosed in a 3" diameter fiber) in *ugriz* filters as described in subsection 3.3.1. In Figure 3.7, we rescale all the new spectra to the synthetic magnitude in the r band ($m_{r,syn}$), which is defined as

$$m_{r,syn} = -2.5\log_{10}(10^{-m_{r,0}/2.5} + 10^{-m_{r,sub}/2.5}), \tag{3.4}$$

where $m_{r,0}$ is the fiber magnitude of the host and $m_{r,sub}$ is the host-subtracted r band magnitude derived from the $t^{-5/3}$ power-law fit at the time of the observation.

In order to measure the broad emission lines in the spectra, we first subtract off the instrumental broadened host template spectrum from the `FAST` fit in subsection 3.3.1, where $\sigma = \sqrt{\sigma^2_{instrument} - \sigma^2_{lib}}$, for each spectrum. The FWHM resolution of the Bruzual & Charlot (2003) template library is 3Å. The host-subtracted spectra are shown in Figure 3.8.

It is known that the spectroscopic signatures of an optically discovered TDEs consist of a strong blue continuum and a combination of broad HeII and Hα emission (Arcavi et al. 2014). We select the regions outside of the Balmer lines and the He II emission line in the host subtracted spectrum to estimate the continuum. The line-free regions are fit with a 5th-order Legendre polynomial. A blackbody spectrum with $T_{bb} = 3.0\times\ 10^4$ (K) is shown in red in Figure 3.9, which is the mean blackbody temperature from the SED fit. The blackbody spectrum shows depature from the host-subtracted spectrum at rest wavelength $\lambda > 4500$ Å.

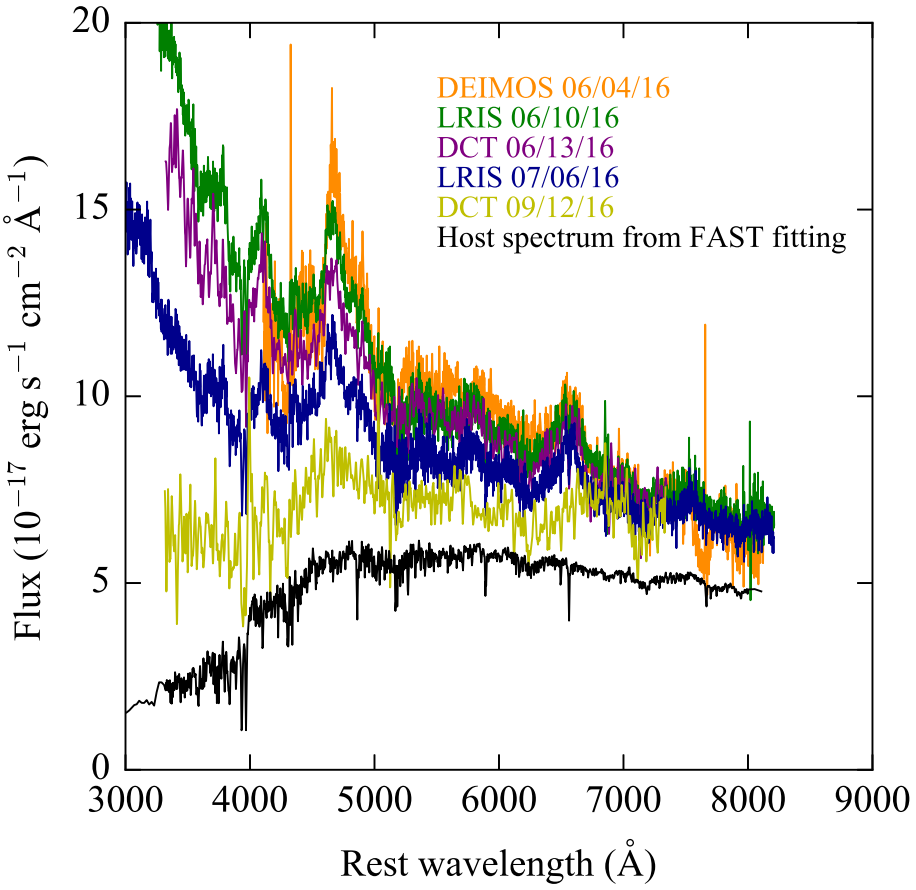

Figure 3.7: Newly observed spectra and host spectrum obtained from fitting the SDSS broadband photometry.

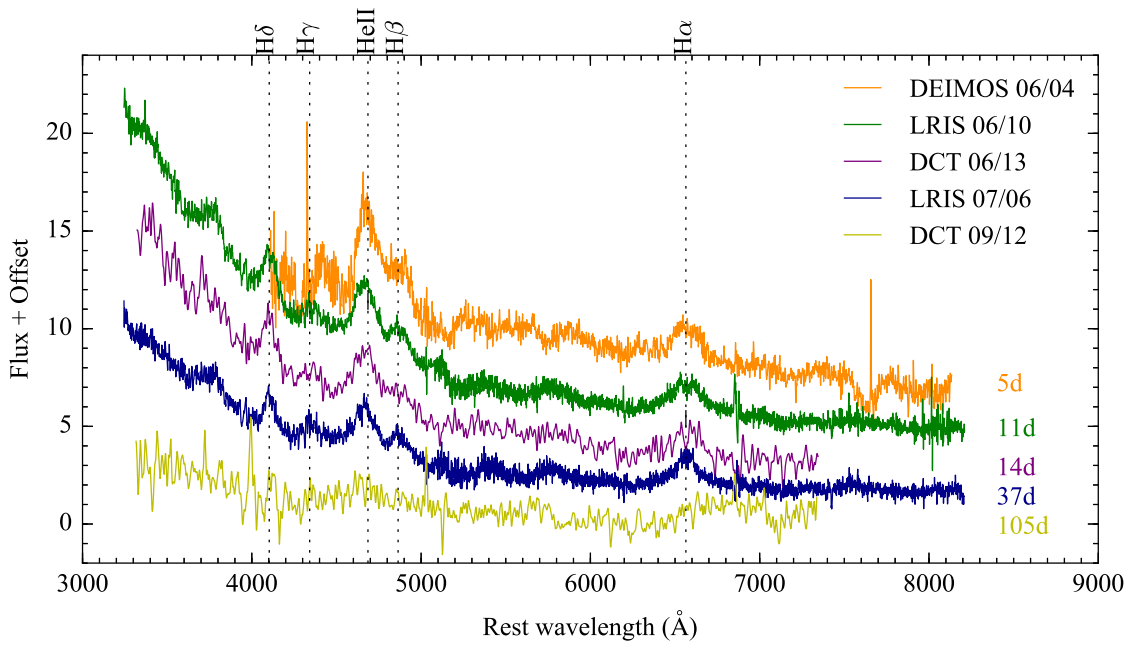

Figure 3.8: Host-subtracted spectra of the new observations. The flux levels are offset for better visualization. The DEIMOS spectrum is smoothed by two pixels.

We approximate the continuum with the Legendre polynomial because it fits the spectra better than the blackbody spectrum and does not require an assumption of the physical origin for the continuum. The line profiles of HeIIλ4686 and Hα are measured after host and TDE continuum subtraction. The best-fit results are shown as red lines in Figure 3.10, where the grey solid line is the flux of the subtracted spectrum centered at the indicated line in velocity space. We simultaneously fit the HeIIλ4686 (orange) and Hβ (green) emissions as two individual Gaussian profiles. The Hα line is modelled as a single Gaussian. The linewidths and line luminosities are listed in Table 3.2.

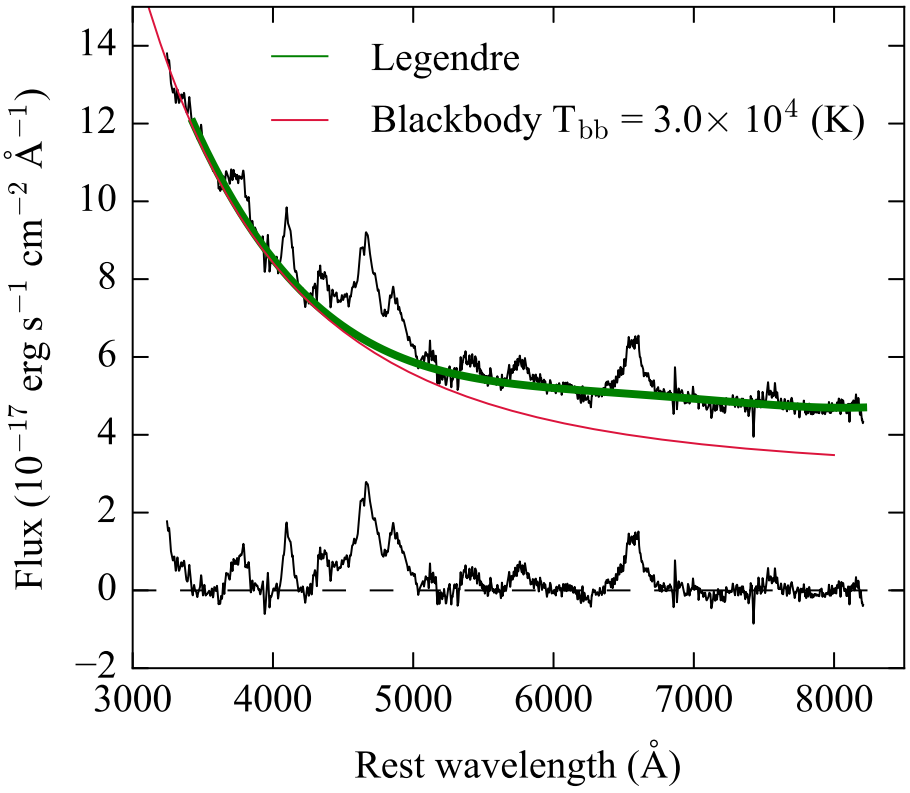

Figure 3.9: An example of continuum subtraction of the host-subtracted LRIS spectrum from Jul 06. The black solid line shows the spectrum smoothed by 2 pixels. The green line shows the best-fit 5th-order Legendre polynomial while the red curve shows a blackbody spectrum. The spectrum near the dashed line is the residual from the subtraction of a 5th-order Legendre polynomial, which fits the spectrum better at shorter wavelengths.

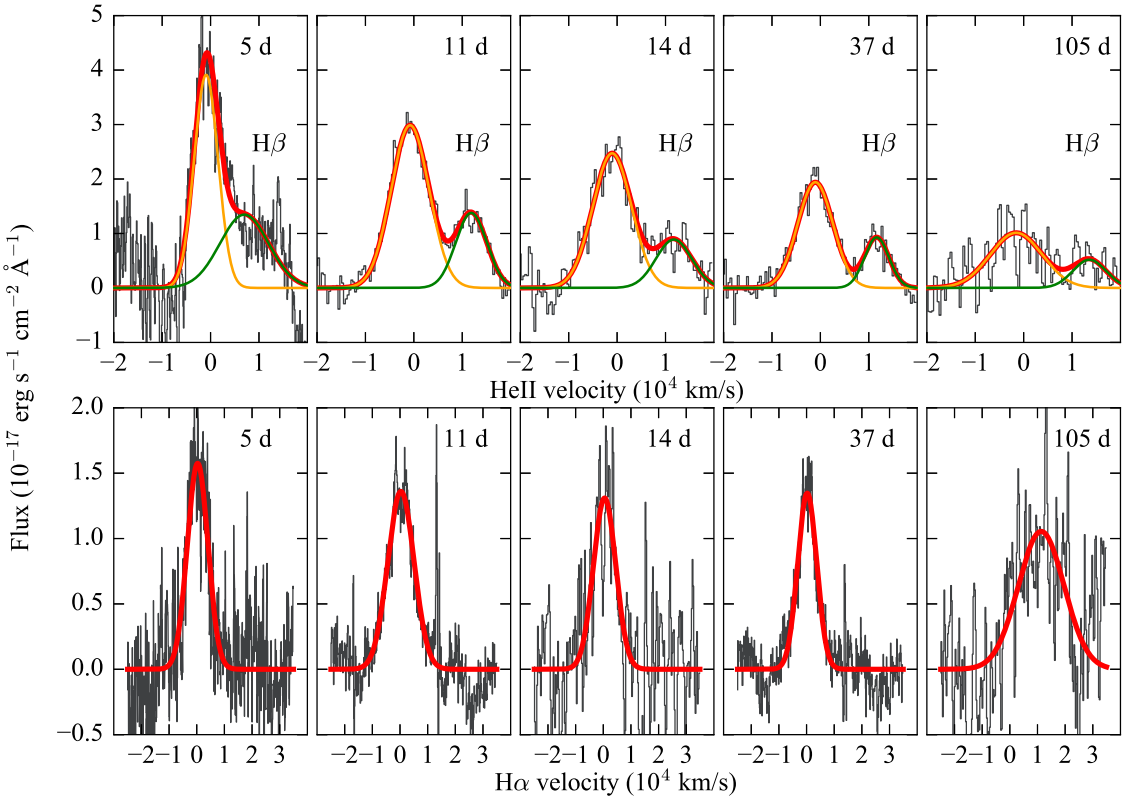

Figure 3.10: Time evolution of He II and Hα line profiles. The black solid lines show the TDE spectra after host and continuum subtraction. The TDE spectra are binned by a factor of 3 for clarity. He II (orange) and Hβ (green) lines are fit simultaneously with two gaussian profiles to resolve spectral blending. The best-fit results are shown by the red solid lines. The time in the upper right corner corresponds to the time elapsed since discovery (MJD 57537.4).

3.6 Discussion

In this section, we start with discussing other potential mechanisms that could drive the observed flare and the implication of the derived rise time for iPTF16axa. We then compare its properties with 11 TDE candidates discovered in UV and optical sky surveys with well-sampled optical light curves: D1-9 and D3-13 from *GALEX*+CFHTLS (Gezari et al. 2008), TDE1 and TDE2 from SDSS (van Velzen et al. 2011), PTF09ge from PTF (Arcavi et al. 2014), PS1-10jh (Gezari et al. 2012), and PS1-11af (Chornock et al. 2014) from *GALEX*+Pan-STARRS1, ASASSN-14ae (Holoien et al. 2014), ASASSN-14li (Holoien et al. 2016b), and ASASSN-15oi (Holoien et al. 2016a) from ASASSN, and iPTF16fnl (Blagorodnova et al. 2017a). The luminosities, temperatures, and radii of the three ASASSN candidate TDEs (ASASSN-14ae, ASASSN-14li, ASASSN-15oi) are provided by T. Holoien via private communication. We calculate the luminosities and radii for the other TDE candidates by scaling the best-sampled optical light curve (g or r-band) to the peak bolometric luminosity reported in the literature, and assuming a constant temperature fixed to the value reported in the literature.

3.6.1 Origin of the flare

The color evolution and the spectroscopic signatures of the flare are not consistent with any known supernova. Supernovae exhibit a much faster color evolution due to cooling in the expanding ejecta and can only remain bright in the UV for a few days. In addition, we do not detect any P-Cygni profile indicative of outflow in

the spectra of iPTF16axa.

Although the nuclear position of the flare may connect it to AGN activity, we do not see any evidence of the host galaxy harbouring an active nucleus. Firstly, common AGN lines such as [OIII] and [NII] are not present in the spectra. Although the Balmer lines Hα and Hβ were detected, the broad Balmer lines have faded almost entirely from June 2016 to September 2016, which indicates the presence of broad Balmer lines is associated with the transient instead of the host galaxy. In fact, in the rare case of a changing-look AGN, we may see broad emission lines in an AGN suddenly appear or disappear on the timescale of a few years (e.g. LaMassa et al. 2015; Gezari et al. 2017b; Shappee et al. 2014; Ruan et al. 2016). However, the lack of X-ray emission in iPTF16axa does not support the changing-look AGN scenario. Furthermore, AGN are known to vary on various timescales across the electromagnetic spectrum. As mentioned in section 3.2, the position of iPTF16axa does not have any historical PTF detection signposting AGN activity between 2011 and 2014.

The photometric and spectroscopic properties bear a stronger resemblance to previous events classified as optical TDE candidates. We compare and discuss their temperatures, luminosities, and spectral line ratios in subsection 3.6.3,subsection 3.6.5, and subsection 3.6.4.

3.6.2 Timescale

We derive the shortest rise time (t_0-t_D) by setting the derivative of Eq. A2 (in Guillochon & Ramirez-Ruiz 2013) with respect to the impact parameter β to zero. The minimum theoretical timescale implied by a 5×10^6 $M_\odot$ black hole is 63 days for β=1.9 assuming a γ=4/3 and a solar type star. Since the TDE was discovered on the decline, we can only place an upper limit on the rise time derived from the observed light curve. The upper limit on the rise time is Δt <49 rest frame days assuming the peak light occurred some time before the iPTF discovery. This rise time is consistent with a black hole mass of less than 3×10^6 $M_\odot$, which is within the intrinsic scatter (0.38 dex) of the M-σ relation in McConnell & Ma (2013) given in subsection 3.3.1.

3.6.3 Temperatures

The blackbody temperature of iPTF16axa remained constant ($T_{bb}\sim3.0\times10^4$ K) over the 3 month monitoring period. This temperature is similar to what was found in PS1-10jh (Gezari et al. 2012), which was also reported to have constant temperature on the timescale of about a year.

The TDE candidates discovered by *GALEX* (D1-9, D3-13), which were also detected in the optical with CFHTLS, have higher blackbody temperatures than the other optical TDE candidates in Figure 3.11. However, the difference is much less significant than the difference between X-ray-detected TDE candidates and optical TDE candidates, where the former is usually 1–2 orders of magnitude hotter than

the latter.

TDE candidates found in the All-Sky Automated Survey for Supernovae (ASASSN), ASASSN-14ae and ASASSN-14li, the SDSS TDEs TDE1 and TDE2, PS1-10jh, PS1-11af, and PTF09ge also have blackbody temperatures that remain roughly constant over months (Figure 3.11). The only outlier here is ASASSN-15oi, which features a ∼100% increase in blackbody temperature on the timescale of less than a month.

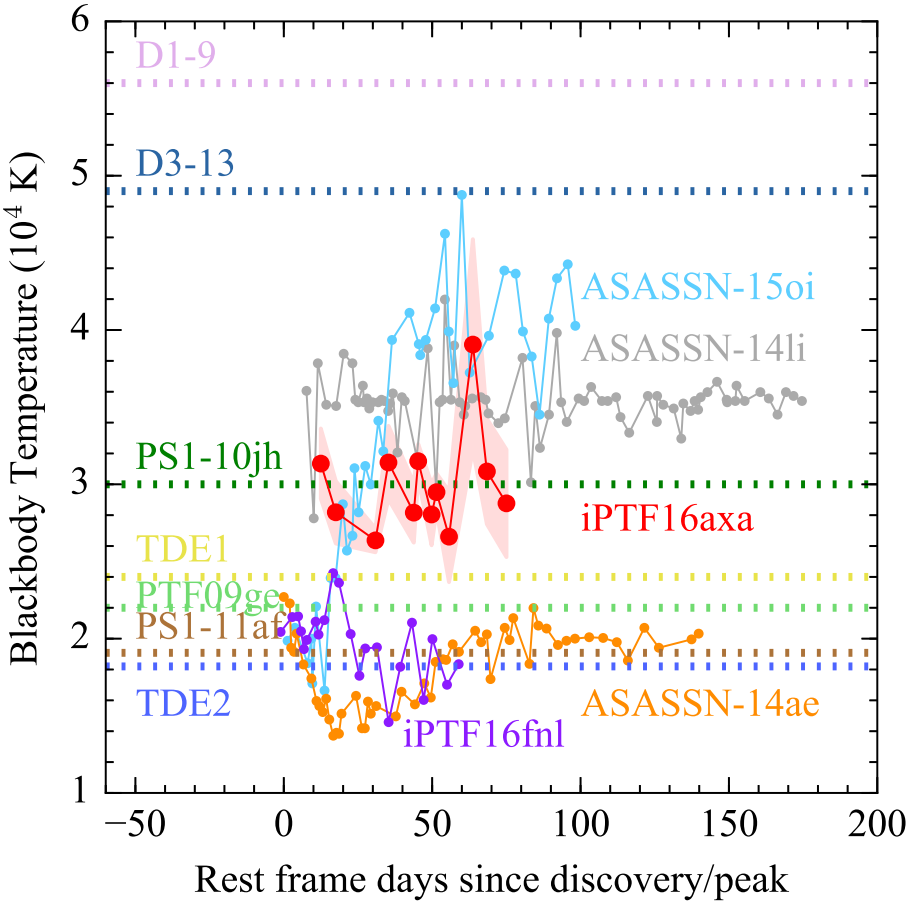

Figure 3.11: Comparison of the evolution of the blackbody temperature inferred from SED fitting. The blackbody temperatures of the UV/optical TDE candidates remain constant on the order of a few 10^4K over time except ASASSN-15oi.

3.6.4 Helium-to-hydrogen ratio

Figure 3.12 shows the integrated Helium-to-Hα line ratio of iPTF16axa and the other TDE candidates discovered in the optical. PS1-10jh, PTF09ge, and ASASSN-15oi do not have Hα emission. A lower limit of 4.7 was reported for PS1-10jh (Gezari et al. 2015), a lower limit of $\sim$ 1 was reported for ASASSN-15oi (Holoien et al. 2016a), and we measure a lower limit of 1.9 for PTF09ge from fitting its spectrum obtained from the Double Spectrograph mounted on the Palomar 200-inch (P200) telescope on 2009 May 20.

We measure the line ratios for ASASSN-14ae and ASASSN-14li by performing Gaussian line fit on the spectra on the open TDE catalog [4] in a similar fashion as described in subsection 3.5.3. The continuum is modelled as a 5th-order Legendre polynomial and subtracted before measuring the lines. ASASSN-14ae did not develop HeIIλ4686 until later epochs.

Throughout the spectroscopic epochs, the Hα line was readily detected in iPTF16axa except for the last epoch. iPTF16axa did not show significant Hα suppression as was observed in PS1-10jh and PTF09ge. From Figure 3.12, the spectroscopic signatures of TDE candidates can be divided into two groups based on the presence/absence of Hα emission. The sources that show both HeIIλ4686 and Hα emission appear to have similar He II/Halpha ratios, with the exception of iPTF16fnl near peak, which shows a high HeIIλ4686-to-Hα ratio that rapidly evolves to the lower ratio observed in the other sources.

[4] `tde.space`

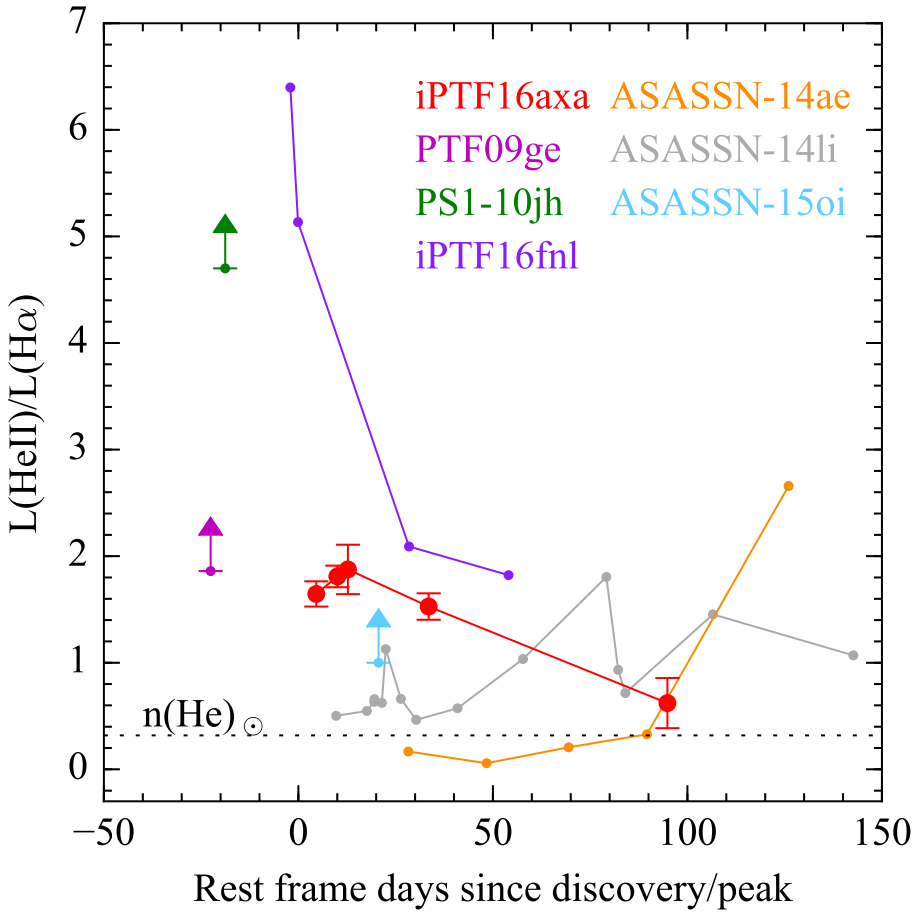

Figure 3.12: Comparison of the evolution of the helium-to-hydrogen line ratio inferred from spectral fitting. The x-axis shows the time elapsed since peak (t_0) for PTF09ge, PS1-10jh, and iPTF16fnl, and time elapsed since *discovery* for the ASASSN TDEs and iPTF16axa (MJD 57537.4). The dotted line shows the expected helium-to-hydrogen ratio in a nebular environment assuming the solar abundance of He/H. It is noticed that nebular arguments may not be valid for TDE candidates despite being frequently used in literature.

The nebular HeIIλ4686 to Hα line ratio can be expressed as

$$\frac{L(\text{HeII}\lambda 4686)}{L(\text{H}\alpha)} = \frac{n(He^{++}) n_e \alpha^{eff}_{\lambda 4686} h\nu_{\lambda 4686}}{n_p n_e \alpha^{eff}_{\lambda \text{H}\beta} (j_{H\alpha}/j_{H\beta}) h\nu_{\lambda \text{H}\beta}}, \tag{3.5}$$

where $n(He^{++})$ is the density of He^{++}, n_p is the proton density, n_e is the electron density, and α^{eff}_{λ} is the effective recombination coefficient. For a typical T=10^4 K nebular gas, $\alpha^{eff}_{\lambda 4686} = 3.57\times\ 10^{-13}$ cm^3 s^{-1}, $\alpha^{eff}_{H_\beta} = 3.02\times\ 10^{-14}$ cm^3 s^{-1}, and $j_{H\alpha}/j_{H\beta}$ is 2.87 (Osterbrock p80). Substituting in these values, the HeIIλ4686 to Hα line ratio can be expressed as 3.98 $n(He^{++})/n_p$ for an electron density of 10^2 cm^{-3} in case B recombination. Assuming the solar helium abundance $Y_\odot = 0.2485$ (Serenelli & Basu 2010), the number abundance of helium $n(He^{++})/n_p$ is $\approx$0.08. This results in a line ratio of $0.32(\frac{n_{He}}{n_{He,\odot}})$, which is denoted by the dotted line in Figure 3.12.

It is noticed that the nebular arguments, while still commonly used in the literature, are not valid for most of the TDE spectra. Figure 3.12 demonstrates that all measurements of the helium-to-hydrogen line ratio in TDEs, with the exception of the early epochs of ASASSN-14ae, display a helium enhancement compared to the nebular prediction assuming solar abundance. While stellar composition may be affecting these ratios in some events, this pattern also suggests that nebular arguments along the lines of Equation 3.5 may break down for TDEs. A likely explanation is that high gas densities ($> 10^{10}$ cm^{-3}) are leading to the suppression of the Balmer lines as these transitions become optically thick. This possibility was first suggested by Bogdanović et al. (2004), and has been recently studied with CLOUDY caclulations (Gaskell & Rojas Lobos 2014; Saxton et al. 2016; Strubbe & Murray 2015) and full radiative transfer calculations (Roth et al. 2016).

3.6.5 Bolometric luminosity

Shown in Figure 3.13 is the time evolution of the UV-optical integrated luminosity of iPTF16axa from the blackbody model. Also shown in this plot are the UV/optical integrated luminosities of ASASSN-14ae, ASASSN-14li, ASASSN-15oi, PS1-10jh, PS1-11af, TDE1, TDE2, D1-9, and D3-13.

In Figure 3.13, all of the TDE candidates except iPTF16fnl follow a power-law decline with a decline rate more or less consistent with $t^{-5/3}$. It is also interesting that, based on our blackbody fit, all of these TDEs except iPTF16fnl are confined to a small range of luminosities, with the peak luminosities ranging from $\log(L$ [erg s^{-1}])$= 43.4-44.4$. We must caution, however, that a substantial fraction of the total radiated energy, especially if originally emitted at FUV and EUV wavelengths, may be missing in our observations, as was demonstrated by van Velzen et al. (2016a) in the case of PTF09ge based on infrared light echo observations.

3.6.6 Photospheric radius

Figure 3.14 shows the evolution of blackbody radius for iPTF16axa and other optically bright TDE candidates. The blackbody radius of iPTF16axa decreased steadily from 4×10^{14} cm to 2×10^{14} cm as the luminosity decreases with time. The blackbody radius of PS1-10jh is derived assuming a $t^{-5/3}$ decay in luminosity and constant temperature. Since the tidal radius is weakly dependent on the black hole mass ($R_T \propto M_{\rm BH}^{1/3}$), Figure 3.14 shows that the derived radii are at least 10 times farther away from the R_T for all the TDE candidates.

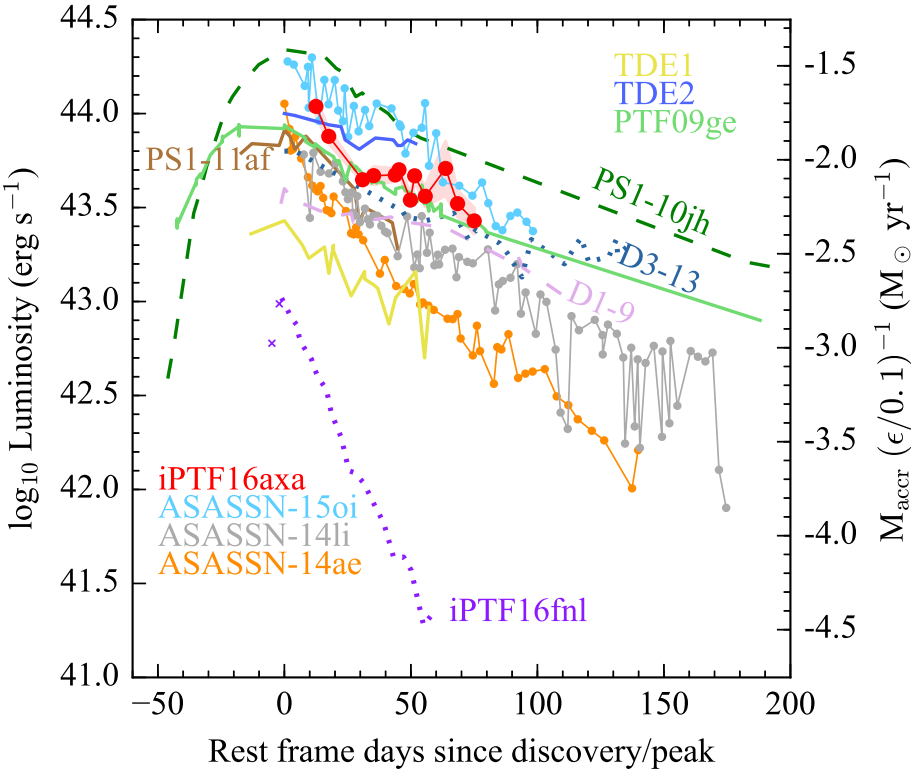

Figure 3.13: Comparison of the evolution of the integrated UV-optical luminosity inferred from SED fitting. The y-axis on the right hand side is the mass accretion rate assuming an efficiency of 0.1. The x-axis shows the time elapsed since peak (t_0) for PTF09ge, PS1-10jh, and iPTF16fnl and the time elapsed since discovery for the ASASSN TDEs and iPTF16axa (MJD 57537.4). The two crosses in purple are derived from pre-peak g band data of iPTF16fnl assuming a blackbody temperature of 2×10^4K. It is worth noting that all of the UV and optically detected TDE candidates discussed here follow a $t^{-5/3}$power law decay except iPTF16fnl. These TDE candidates span a narrow range in the peak luminosity log(L [erg s^{-1}]) = 43.4–44.4.

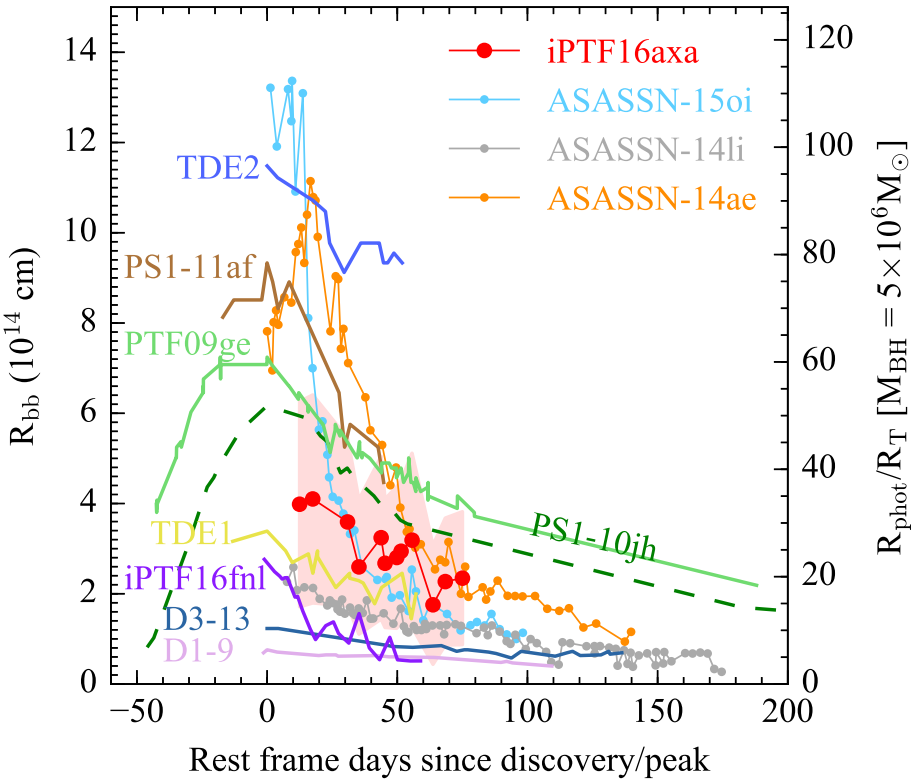

Figure 3.14: Comparison of the evolution of the blackbody radius (R_{bb}) inferred from SED fitting. The dots in the figure represent R_{bb} derived from the SED some time after discovery for iPTF16axa and the ASASSN objects. The pink shaded area shows the uncertainties of R_{bb} for iPTF16axa. The blackbody radii derived are on the order of a few 10 times of the tidal radius.

Due to the non-varying temperature evolution of TDE emission, the photospheric radius must decline at late times in order to match the fading light curve. The physical meaning of this decline remains unclear. One explanation is that the density of the optically emitting gas drops over time, allowing the observer to see light emitted from increasingly deeper regions, even if the gas is continuously outflowing (Strubbe & Murray 2015). Another possibility is that the optically emitting gas is in fact moving closer to the black hole over time, and may be related to the decreasing apocenter radius of the circularizing debris stream (Bonnerot et al. 2017).

3.6.7 Virial radius

The FWHMs of HeIIλ4686 and Hα are plotted in Figure 3.15. The triangles denote the linewidths of HeIIλ4686 lines while the dots denote the linewidths of Hα emission. The HeIIλ4686 linewidths for ASASSN-14ae and ASASSN-14li were measured using the spectra on the open TDE catalog. The HeIIλ4686 linewidth of PTF09ge is measured from its P200 spectrum and the value for PS1-10jh is provided in Gezari et al. (2012).

In Figure 3.15, the FWHMs of He II and Hα emission lines evolve in the same trend. Throughout the observations of iPTF16axa, the HeIIλ4686 linewidth remains comparable, sometimes even narrower, than the linewidths of Hα. The fact that the linewidths of He II are not wider than that of Hα suggests the line emitting material is not virially bound. In the scenario of a stratified broad line region, because the photoionization energy of He is higher than hydrogen, helium has to be emitted

at a smaller radius and therefore would have a wider linewidth. As pointed out in Holoien et al. (2016b,a), in reverberation mapping studies, the linewidths would increase while the luminosity decreases due to recombination at outer radii. This trend is also not observed until the last epoch when the line detection was weak.

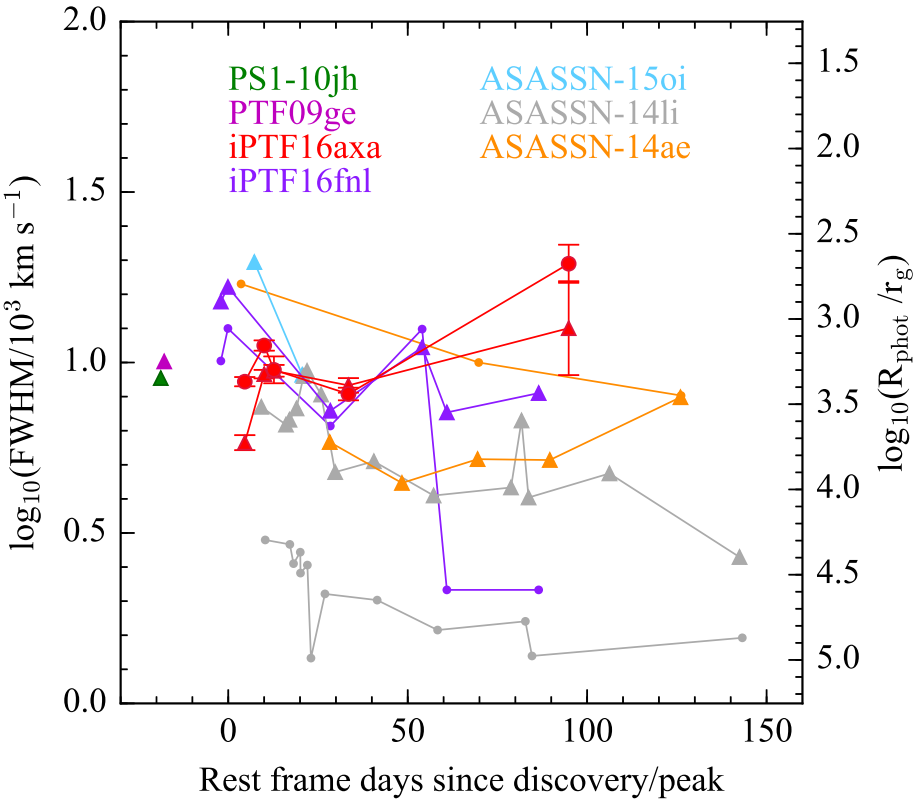

Figure 3.15: Comparison of the evolution of the photosphere radius inferred from emission linewidths. The triangles mark the linewidths of HeII lines while the dots mark the linewidths of Hα emission. The y-axis on the right hand side shows the photospheric radii in units of the gravitational radius $r_g = GM/c^2$. Throughout the monitoring period, the FWHM of Hα and HeII evolve in a similar trend. The fact that HeII line is not wider than Hα disfavors the scenario of a stratified BLR region that is virially bound.

3.6.8 Peak luminosity

In Figure 3.16 we plot the peak luminosity reported in the literature as a function of the black hole mass. The circle symbols show black hole masses reported in literature while the diamond symbols show black hole masses estimated from the r-band scaling relation in Tundo et al. (2007), which has a 1σ scatter of 0.33 dex. We obtain black hole mass of ASASSN-14ae from Holoien et al. (2014), ASASSN-14li from Holoien et al. (2016b), ASASSN-15oi from Holoien et al. (2016a), PS1-11af from Chornock et al. (2014), PTF09ge from Arcavi et al. (2014), D1-9 and D3-13 from Gezari et al. (2009), and TDE1 and TDE2 from van Velzen et al. (2011).

We show four different ratios of Eddington luminosity, L_{Edd}, $0.1L_{Edd}$, $10^{-2}L_{Edd}$, $10^{-3}L_{Edd}$, as a function of the black hole mass with the black dotted lines. The black dashed line in Figure 3.16 shows the theoretical scaling of $L_{peak} \propto \dot{M}_{peak} \propto M_{\rm BH}^{-1/2}$ (Lodato & Rossi 2011; Guillochon & Ramirez-Ruiz 2013) normalized to Eq. A1 in Guillochon & Ramirez-Ruiz (2013) assuming a star with solar mass and radius, γ=4/3, β=1, and an accretion efficiency ϵ of 0.1. The dashed line does not extend below $M_{\rm BH} \sim 10^{6.6}\ M_{\odot}$ since the emergent luminosity should be Eddington limited. Below this threshold, the luminosity scales with the Eddington luminosity, $L_{peak} \propto L_{Edd} \propto M_{\rm BH}$. We do not see a clear trend in the data that suggests the peak luminosity and the black hole mass are correlated, although we emphasize again that undetected emission originally at FUV and EUV wavelengths may alter this conclusion, and that many of the TDE candidates plotted were discovered post-peak, and thus their luminosity at discovery may be underestimating the true

peak luminosity.

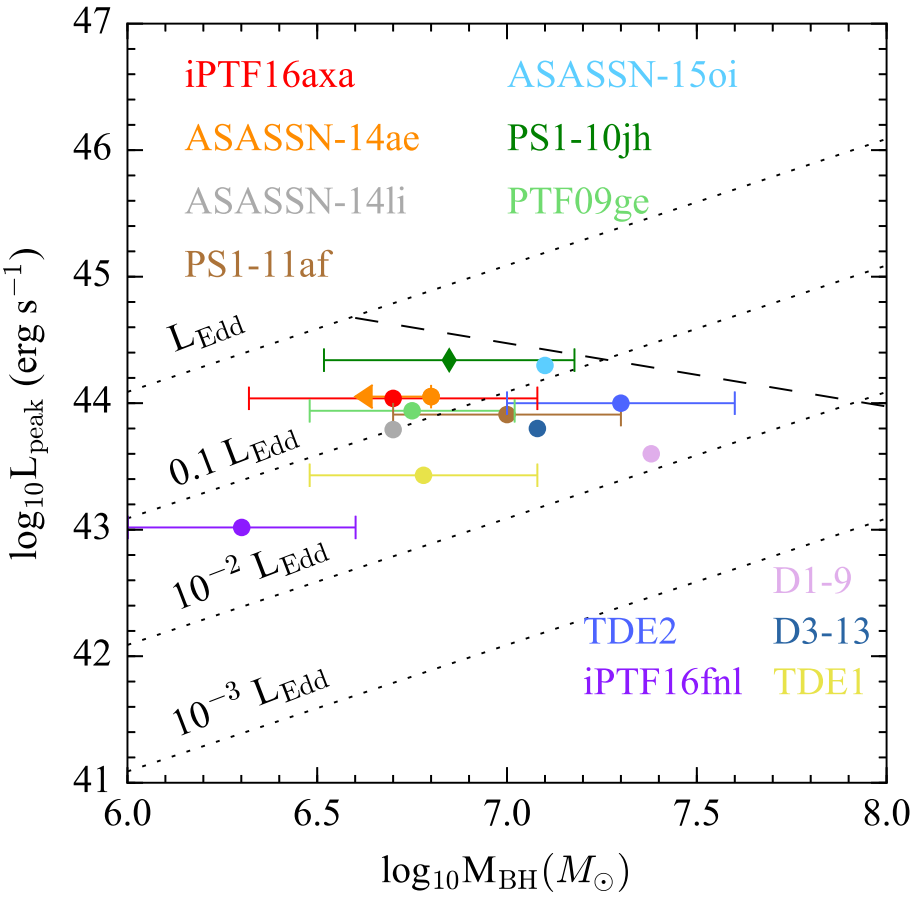

Figure 3.16: The peak luminosities for TDEs from Figure 3.13 vs black hole masses. Black hole masses obtained from literature are marked in circles while triangles are black hole masses derived using r-band scaling in Tundo et al. (2007). The dotted lines show the luminosities that correspond to 4 different Eddington ratios while the black dashed line shows the $\dot{M}_{peak} \propto M_{\rm BH}^{-1/2}$ relation expected from theoretical work normalized to Eq. A1 in Guillochon & Ramirez-Ruiz (2013) with γ=4/3, β=1, and ϵ=0.1. Below $M_{\rm BH} \sim 10^{6.6}\ M_\odot$, the luminiosity should be Eddington-limited and scales proportionally with $M_{\rm BH}$.

3.7 Conclusion

We present results from photometric and spectroscopic follow up observations of a strong TDE candidate, iPTF16axa, and comparisons of the derived physical quantities with 11 other optically studied TDE candidates from ASASSN, GALEX+CFHTLS, PTF, PS1, and SDSS. Both *Swift* UVOT observations and the follow up spectra of iPTF16axa are consistent with the object being a TDE rather than a supernova or a variable AGN. The UV and optical light curves of iPTF16axa are in good agreement with the $t^{-5/3}$ relation and suggest the TDE was discovered 49 rest-frame days after disruption. The light curve shows no color evolution with time, with an SED fitted with a constant temperature of $3{\times}10^4$ K. The TDE is hosted by an early-type galaxy with an estimated black hole mass of $5{\times}10^6 M_{\odot}$, which is similar to previously reported TDE candidate hosts. We summarize the comparisons of a sample totaling 12 TDE candidates including iPTF16axa below.

1. TDE candidates discovered in the UV and optical remain roughly constant temperature over several months. The blackbody temperatures of the TDE candidates are found to be a few 10^4 K.

2. Our sample of TDE candidates are characterized by a power law decline and, based on a blackbody fit to optical and near-UV data, span a small range of peak luminosity of $10^{43.4} < L_{peak} < 10^{44.4}$. The decline is more or less consistent with the classic $t^{-5/3}$ prediction except in iPTF16fnl, which fades more steeply than the other TDE candidates discussed in this paper.

3. Nebular arguments are not valid for interpreting line ratios in most optically discovered TDE candidates due to the presence of high density gas, which can lead to the suppression of hydrogen Balmer transitions. The spectra of UV/optical TDE candidates show a range of He-to-Hα ratios, and the time-evolution of these ratios also differs between events. Detailed modeling will be necessary to understand these behaviors.

4. The blackbody radii derived from the SEDs of UV/optical TDE candidates trace distances that are much larger than the tidal radius ($\approx$ a few 10R$_T$), and that decline with time.

5. The FWHM of HeIIλ4686 is consistent with the FWHM of Hα in the optical spectra of UV/optical TDE candidates. This evidence contradicts the assumption of a stratified BLR.

6. Theoretical work shows that the peak luminosity and the black hole mass are correlated by $L_{peak} \propto M_{\rm BH}^{-1/2}$ except at smaller black hole masses, where the emission is Eddington-capped ($L_{peak} \propto M_{\rm BH}$). However, there is no strong trend between the two quantities in the sample of candidate TDEs discovered in UV and optical.

3.8 Acknowledgements

We thank the anonymous referee for their helpful comments on the manuscript. T.H. thanks T. Holoien and C. Bonnerot for providing data from their papers. S.G.

is supported in part by NSF CAREER grant 1454816, NASA *Swift* Cycle 12 grant NNX16AN85G, and NASA Keck Grant 1568615. N.R. acknowledges the support of a Joint Space-Science Institute prize postdoctoral fellowship. A.H. acknowledges support by a grant from the I-CORE program "From the Big Bang to Planets". Support for I.A. was provided by NASA through the Einstein Fellowship Program, grant PF6-170148. These results made use of the Discovery Channel Telescope at Lowell Observatory. Lowell is a private, non-profit institution dedicated to astrophysical research and public appreciation of astronomy and operates the DCT in partnership with Boston University, the University of Maryland, the University of Toledo, Northern Arizona University and Yale University. The W. M. Keck Observatory is operated as a scientific partnership among the California Institute of Technology, the University of California, and NASA; the Observatory was made possible by the generous financial support of the W. M. Keck Foundation. This research used resources of the National Energy Research Scientific Computing Center, a DOE Office of Science User Facility supported by the Office of Science of the U.S. Department of Energy under Contract No. DE-AC02-05CH11231.

Table 3.1. Blackbody fitting from light curves

MJD	$t - t_{disc}$	BB Temperature	BB Radius	Luminosity
	days	10^4 K	10^{14} cm	10^{43}erg s^{-1}
57551.23	14	3.13±0.23	3.98±2.27	10.91±1.14
57556.82	19	2.82±0.2	4.1±2.31	7.56±0.66
57571.63	34	2.64±0.08	3.59±1.86	4.44±0.13
57576.48	39	3.14±0.24	2.6±1.49	4.67±0.51
57585.93	49	2.82±0.19	3.24±1.81	4.71±0.37
57587.59	50	3.15±0.11	2.68±1.42	5.02±0.28
57592.58	55	2.8±0.2	2.8±1.57	3.46±0.29
57594.42	57	2.95±0.12	2.94±1.57	4.67±0.25
57599.09	62	2.66±0.29	3.19±1.93	3.63±0.45
57608.0	71	3.91±0.68	1.76±1.32	5.11±1.69
57613.24	76	3.08±0.34	2.27±1.41	3.32±0.53
57620.54	83	2.88±0.35	2.35±1.47	2.68±0.43

Table 3.2. Emission line fit

Date	He II FWHM (10^3 km s^{-1})	L(He II) (10^{40} erg s^{-1})	Hα FWHM (10^3 km s^{-1})	L(Hα) (10^{40} erg s^{-1})
2016-06-04	5.8±0.3	12.5±0.8	8.8±0.3	7.6±0.3
2016-06-10	9.2±0.3	15.1±0.6	11.2±0.4	8.3±0.4
2016-06-13	9.5±0.4	12.8±0.7	9.5±0.9	6.8±0.8
2016-07-06	8.6±0.4	9.1±0.6	8.1±0.3	6.0±0.3
2016-09-12	12.6±4.2	7.0±2.6	19.5±2.4	11.2±1.5

Table 3.3. Photometric data of iPTF16axa

MJD	Magnitude	Filter	Telescope
57546.189	19.110 ± 0.050	UVW2	*Swift*
57551.232	19.070 ± 0.060	UVW2	*Swift*
57556.824	19.350 ± 0.070	UVW2	*Swift*
57571.634	19.920 ± 0.090	UVW2	*Swift*
57576.485	20.040 ± 0.100	UVW2	*Swift*
57585.937	19.920 ± 0.110	UVW2	*Swift*
57592.583	20.220 ± 0.160	UVW2	*Swift*
57594.428	19.870 ± 0.060	UVW2	*Swift*
57599.095	20.120 ± 0.080	UVW2	*Swift*
57607.999	20.300 ± 0.080	UVW2	*Swift*
57613.241	20.380 ± 0.070	UVW2	*Swift*
57620.542	20.470 ± 0.090	UVW2	*Swift*
57551.236	19.250 ± 0.070	UVM2	*Swift*
57556.828	19.500 ± 0.070	UVM2	*Swift*
57571.637	19.980 ± 0.090	UVM2	*Swift*
57576.487	20.070 ± 0.100	UVM2	*Swift*
57587.593	20.110 ± 0.110	UVM2	*Swift*

Table 3.3 (cont'd)

MJD	Magnitude	Filter	Telescope
57592.586	20.450 ± 0.250	UVM2	*Swift*
57594.436	20.060 ± 0.100	UVM2	*Swift*
57599.099	20.160 ± 0.160	UVM2	*Swift*
57608.002	20.640 ± 0.130	UVM2	*Swift*
57613.248	20.550 ± 0.120	UVM2	*Swift*
57620.546	20.740 ± 0.150	UVM2	*Swift*
57551.230	19.320 ± 0.090	UVW1	*Swift*
57556.820	19.500 ± 0.100	UVW1	*Swift*
57561.391	19.650 ± 0.160	UVW1	*Swift*
57571.630	19.780 ± 0.120	UVW1	*Swift*
57576.483	20.320 ± 0.180	UVW1	*Swift*
57585.933	19.910 ± 0.170	UVW1	*Swift*
57592.581	20.020 ± 0.230	UVW1	*Swift*
57594.422	20.500 ± 0.140	UVW1	*Swift*
57599.092	20.190 ± 0.130	UVW1	*Swift*
57607.997	20.430 ± 0.140	UVW1	*Swift*
57613.235	20.430 ± 0.130	UVW1	*Swift*

Table 3.3 (cont'd)

MJD	Magnitude	Filter	Telescope
57620.538	20.740 ± 0.190	UVW1	*Swift*
57551.231	19.300 ± 0.140	UVOT-U	*Swift*
57556.822	19.410 ± 0.150	UVOT-U	*Swift*
57571.632	19.950 ± 0.220	UVOT-U	*Swift*
57576.484	20.090 ± 0.250	UVOT-U	*Swift*
57585.935	19.820 ± 0.220	UVOT-U	*Swift*
57587.587	19.820 ± 0.130	UVOT-U	*Swift*
57594.425	19.940 ± 0.130	UVOT-U	*Swift*
57599.093	20.220 ± 0.190	UVOT-U	*Swift*
57607.998	20.170 ± 0.170	UVOT-U	*Swift*
57613.238	20.220 ± 0.150	UVOT-U	*Swift*
57620.540	20.140 ± 0.200	UVOT-U	*Swift*
57537.397	19.486 ± 0.071	g	P48
57540.404	19.615 ± 0.032	g	P60
57541.428	19.592 ± 0.031	g	P60
57544.370	19.464 ± 0.081	g	P48
57547.399	19.724 ± 0.027	g	P60

Table 3.3 (cont'd)

MJD	Magnitude	Filter	Telescope
57548.385	19.626 ± 0.085	g	P48
57548.510	20.119 ± 0.137	gp	LCO
57552.373	19.673 ± 0.103	g	P48
57554.378	19.959 ± 0.042	g	P60
57555.590	20.579 ± 0.157	gp	LCO
57558.469	20.192 ± 0.127	g	P60
57565.219	20.165 ± 0.076	g	P60
57566.220	20.284 ± 0.027	g	P60
57574.502	20.918 ± 0.108	gp	LCO
57581.465	20.931 ± 0.122	gp	LCO
57583.261	20.611 ± 0.053	g	P60
57585.194	20.749 ± 0.070	g	P60
57587.193	20.699 ± 0.105	g	P60
57587.472	20.612 ± 0.274	gp	LCO
57593.234	20.736 ± 0.048	g	P60
57595.182	20.771 ± 0.048	g	P60
57595.453	21.310 ± 0.278	gp	LCO

Table 3.3 (cont'd)

MJD	Magnitude	Filter	Telescope
57597.239	20.883 ± 0.056	g	P60
57599.197	20.875 ± 0.046	g	P60
57601.183	20.947 ± 0.081	g	P60
57605.213	21.041 ± 0.048	g	P60
57607.176	20.995 ± 0.052	g	P60
57609.177	21.011 ± 0.057	g	P60
57611.196	21.079 ± 0.067	g	P60
57613.173	21.038 ± 0.100	g	P60
57614.180	21.261 ± 0.141	g	P60
57615.168	21.221 ± 0.177	g	P60
57616.166	21.111 ± 0.113	g	P60
57617.169	20.903 ± 0.181	g	P60
57618.150	21.329 ± 0.191	g	P60
57619.156	20.976 ± 0.143	g	P60
57621.150	21.160 ± 0.120	g	P60
57625.158	21.203 ± 0.049	g	P60
57631.152	21.218 ± 0.071	g	P60

Table 3.3 (cont'd)

MJD	Magnitude	Filter	Telescope
57633.166	21.297 ± 0.063	g	P60
57635.135	21.356 ± 0.138	g	P60
57639.227	21.413 ± 0.093	g	P60
57646.190	21.328 ± 0.330	g	P60
57656.182	21.536 ± 0.277	g	P60
57540.397	20.045 ± 0.033	r	P60
57541.421	19.972 ± 0.054	r	P60
57547.392	20.090 ± 0.029	r	P60
57548.514	19.999 ± 0.391	rp	LCO
57551.451	20.162 ± 0.030	r	P60
57554.368	20.235 ± 0.074	r	P60
57558.459	20.404 ± 0.106	r	P60
57559.483	20.401 ± 0.260	r	P60
57565.198	20.527 ± 0.127	r	P60
57566.205	20.661 ± 0.029	r	P60
57569.229	20.711 ± 0.040	r	P60
57574.512	20.543 ± 0.283	rp	LCO

Table 3.3 (cont'd)

MJD	Magnitude	Filter	Telescope
57581.474	20.671 ± 0.297	rp	LCO
57583.255	21.020 ± 0.087	r	P60
57585.188	21.149 ± 0.113	r	P60
57587.188	21.025 ± 0.144	r	P60
57587.480	20.580 ± 0.339	rp	LCO
57593.228	21.063 ± 0.068	r	P60
57595.176	21.241 ± 0.102	r	P60
57595.462	20.603 ± 0.342	rp	LCO
57597.234	21.213 ± 0.100	r	P60
57599.191	21.086 ± 0.077	r	P60
57605.207	21.280 ± 0.069	r	P60
57607.170	21.380 ± 0.105	r	P60
57609.171	21.317 ± 0.124	r	P60
57611.191	21.267 ± 0.108	r	P60
57613.167	21.377 ± 0.150	r	P60
57614.175	21.320 ± 0.171	r	P60
57616.161	21.284 ± 0.212	r	P60

Table 3.3 (cont'd)

MJD	Magnitude	Filter	Telescope
57617.163	21.155 ± 0.244	r	P60
57621.144	21.398 ± 0.170	r	P60
57625.153	21.358 ± 0.107	r	P60
57629.148	21.478 ± 0.091	r	P60
57631.146	21.474 ± 0.160	r	P60
57633.161	21.464 ± 0.113	r	P60
57637.139	21.650 ± 0.226	r	P60
57639.222	21.634 ± 0.180	r	P60
57640.182	21.489 ± 0.096	r	P60
57646.151	21.640 ± 0.356	r	P60
57656.140	21.896 ± 0.527	r	P60
57540.401	19.901 ± 0.045	i	P60
57541.424	19.827 ± 0.050	i	P60
57547.395	19.891 ± 0.054	i	P60
57548.527	20.046 ± 0.378	ip	LCO
57551.456	20.041 ± 0.052	i	P60
57554.373	20.063 ± 0.118	i	P60

Table 3.3 (cont'd)

MJD	Magnitude	Filter	Telescope
57555.599	19.796 ± 0.357	ip	LCO
57558.464	20.171 ± 0.143	i	P60
57565.202	20.408 ± 0.356	i	P60
57574.519	20.586 ± 0.311	ip	LCO
57581.482	20.642 ± 0.326	ip	LCO
57583.258	20.633 ± 0.127	i	P60
57585.191	20.615 ± 0.093	i	P60
57587.191	20.881 ± 0.144	i	P60
57587.489	20.537 ± 0.462	ip	LCO
57593.231	20.829 ± 0.082	i	P60
57595.179	20.879 ± 0.143	i	P60
57595.470	20.747 ± 0.408	ip	LCO
57597.237	20.769 ± 0.101	i	P60
57599.194	21.000 ± 0.101	i	P60
57605.210	21.116 ± 0.089	i	P60
57607.173	20.975 ± 0.125	i	P60
57609.174	21.109 ± 0.114	i	P60

Table 3.3 (cont'd)

MJD	Magnitude	Filter	Telescope
57611.194	21.012 ± 0.223	i	P60
57613.170	20.974 ± 0.163	i	P60
57616.163	21.030 ± 0.189	i	P60
57617.166	21.165 ± 0.286	i	P60
57625.156	21.086 ± 0.125	i	P60
57631.149	21.146 ± 0.141	i	P60
57633.164	21.111 ± 0.155	i	P60
57639.224	21.417 ± 0.244	i	P60
57646.171	21.199 ± 0.256	i	P60
57656.163	21.213 ± 0.276	i	P60

Chapter 4: Finding Tidal Disruption Events in ZTF

4.1 Introduction

The Zwicky Transient Facility (ZTF) is a optical synoptic survey built on the the experience of PTF. ZTF uses the same 48-inch Samuel Oschin Schmidt telescope at the Palomar observatory. Capitalizing on a new camera with an unprecedent wide FOV of 47 $\deg^2$ and reduced overhead time, ZTF is discovering transients at a speed that is an order of magnitude faster than iPTF.

ZTF is partially funded by NSF through the Mid-Scale Innovations Program (MSIP). Through the support from NSF, 40% of the ZTF time will be used to conduct a general-purpose survey slow-wide survey over the Northern sky for three years (2018–2020). The public MSIP survey is designed to scan over $\sim$15000 $\deg^2$ of area every 3 days in both g and r filters. The median image quality of ZTF is $\sim 2.0''$ FWHM. ZTF achieves a 5σ depth of 20.4 mag in r band in a single exposure (30s).

Each night, alerts are generated at IPAC with a realtime image-subtraction pipeline (Masci et al. 2018, PASP, in review). The latency in alert delivery is approximately 10 to 20 minutes following the observation.

4.2 Data

ZTF alert packets contain contextual information for each source extracted from a difference image (science frame − reference frame). The alert packets are stored in the Apache Avro format and have nested schemas. We show the top-level alert schema `ztf.alert` in Table 4.1. Under this structure, the photometric and astrometric information associated with each ZTF alert are stored in `ztf.alert.candidate`. A list of alert packets that have the same format as `ztf.alert.candidate` from the past 30 day is provided in `ztf.alert.prv_candidates`. We list a partial[1] schema of `ztf.alert.candidate` with field names relevent to our analysis in Table 4.2.

4.3 GROWTH Marshal

ZTF generates a vast amount of alerts (on the order of 10^5) per night. Given the limited follow-up resources, efficient data mining has become important for identifying sources of interest in a timely manner. To achieve this, the ZTF collaboration uses a web interface, GROWTH[2] Marshal, to ingest the alert stream and save sources that meet a set of pre-defined criteria. The GROWTH Marshal also provides an intuitive interface for users to organize and plan follow-up observations.

Discovery and vetting of TDE candidates in ZTF can be broken down into 3

[1]The full schema can be found at github.com/ZwickyTransientFacility/ztf-avro-alert.

[2]The Global Relay of Observatories Watching Transients Happen (GROWTH) is a NSF-funded international scientific collaborative project in astronomy studying the physics of transient events.

steps. Firstly, the nightly alert stream is examined against an initial filter in the GROWTH Marshal filter language (Kasliwal et al in prep). The GROWTH Marshal filter language restricts its users to filter only on the keywords in the alert packets in order to minimize the usage of computationally expensive calculations at this stage. For TDE candidates, we constrain our search to sources that satisfy the following criteria.

1. Nuclear (`distnr` $< 0.8(0.5^{3})$).
2. Positive subtraction (`isdiffpos` is True).
3. A real (see subsection 4.4.4 for details) transient event as opposed to image subtraction artifacts (`rb` > 0.2).
4. Host is a galaxy as opposed to a point source (`sgscore` < 0.3).
5. Two detections separated by 30 minutes.
6. Not a diffraction spike artifact caused by a nearby bright star (`magnr` < 15 mag).

The second step involves users to manually inspect through the list of candidates that passed the GROWTH Marshal filter. The most common type of bogus seen at this stage is artifacts caused by diffraction spikes of nearby bright stars. These can be readily discerned on the scanning page when a masked star is present in the cutout image and there is no sign of an underlying source at the position of the

[3]Updated on May 16 2018.

event in the reference frame (Figure 4.1). Other types of bogus may arise from erroraneous star-galaxy separation or image subtraction artifacts against galaxies with bright cores. Currently, the real-bogus (RB) algorithm is not able to identify these artifacts confidently; more descriptions of RB will be detailed in subsection 4.4.4.

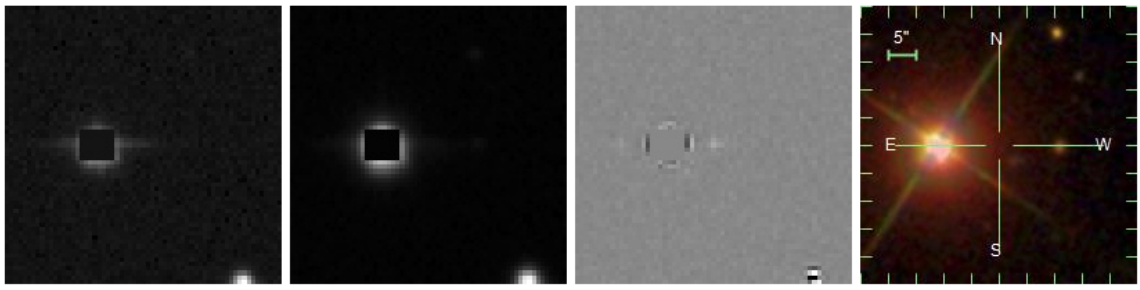

Figure 4.1: An example of a "bogus" ZTF event that is actually a diffraction spike of a bright star. From left to right: (1) Science cutout image. (2) Reference cutout image. (3) Difference image cutout. (4) SDSS thumbnail showing no underlying source is associated with this detection.

To minimize the loss due to human decisions, human scanners save all the events that are not spikes or in crowded stellar fields. Since no cross-matching to external AGN catalogues was performed in the previous steps, we expect AGNs to contribute significantly to our sample. We separate events that are likely to be caused by nuclear activity by cross-matching to the Million Quasar catalog (Flesch 2017) and the Véron-Cetty & Véron (2010) catalog, which are inclusive of all the spectroscopically classified SDSS AGNs. We also use WISE color ($W1 - W2 > 0.8$) to identify AGNs (Stern et al. 2012).

Since ZTF commissioning in Feb 2018 to Jun 24th 2018, the nuclear transient group has saved a total of 761 ZTF events. As shown in Figure 4.2, 54.7% (417/761)

of the sources have been classified. In thi pie chart, all of the supernovae are classified with spectroscopy while most of the LINERs and AGNs are classified by cross-matching to an AGN catalog. Some stars have slipped through the filter due to their low `sgscore`, these are labeled as varstar in Figure 4.2. In Figure 4.2, bogus is the code for artificial residuals when subtracting against a bright galaxy core. These are identified by the gaps of non-detections between detections in their light curves (see Figure 4.3 for example).

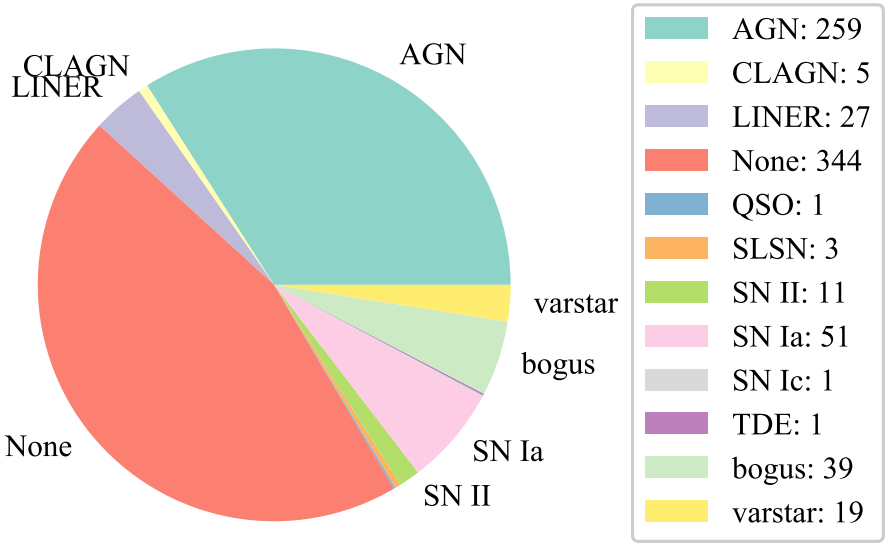

Figure 4.2: Pie chart that shows the composition of the nuclear candidate sample since ZTF commissioning till Jun 24th 2018. During this period, we have identidied 1 TDE and 5 changing-look AGN (CLAGN) that have shown dramatic spectral change with the appearance of prominent broad Balmer emission lines.

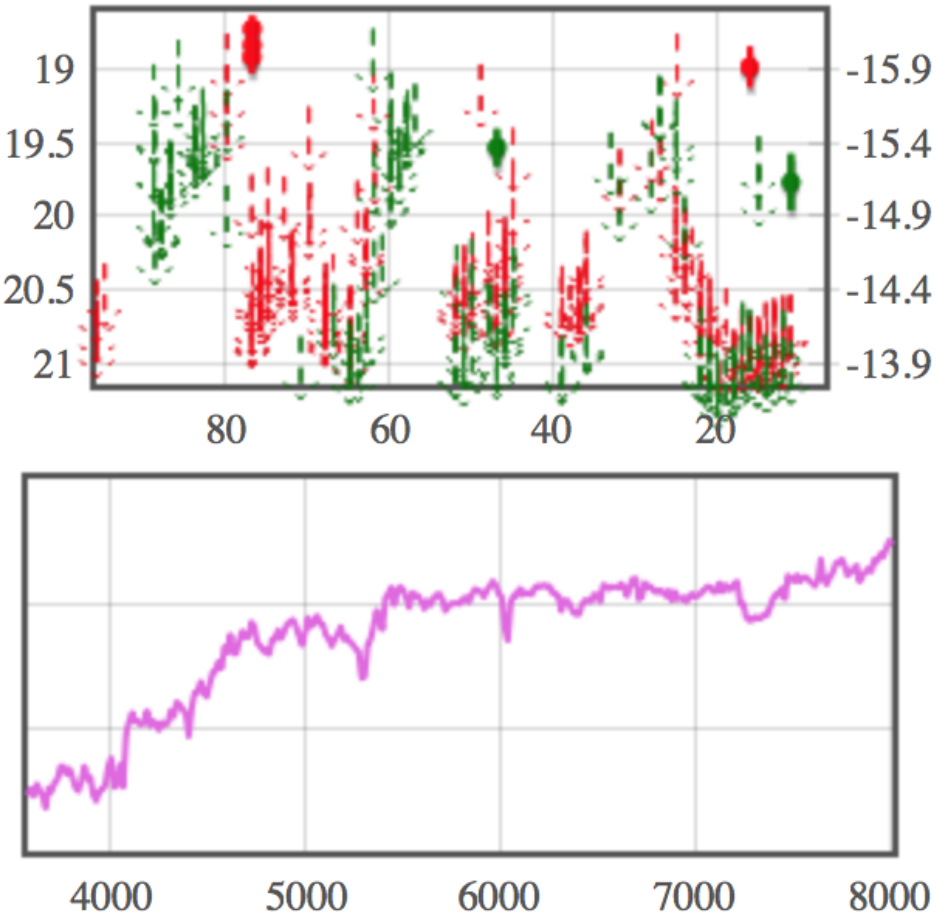

Figure 4.3: The light curve and spectrum of ZTF18aahzmqo, a "bogus" caused by bad subtraction in the center of a galaxy. The light curve has upper limits amid detections that is unlike a transient. The optical spectrum in the right panel confirms that there is no transient event in this galaxy.

4.4 Parameter Distribution

I use a subsample of spectroscopically classified sources to examine several parameter distributions for different source populations with the idea to further reduce the number of non-TDEs, including bogus events and main TDE interlopers: AGN and SN Ia. The composition of source types in this subsample is shown in Figure 4.4.

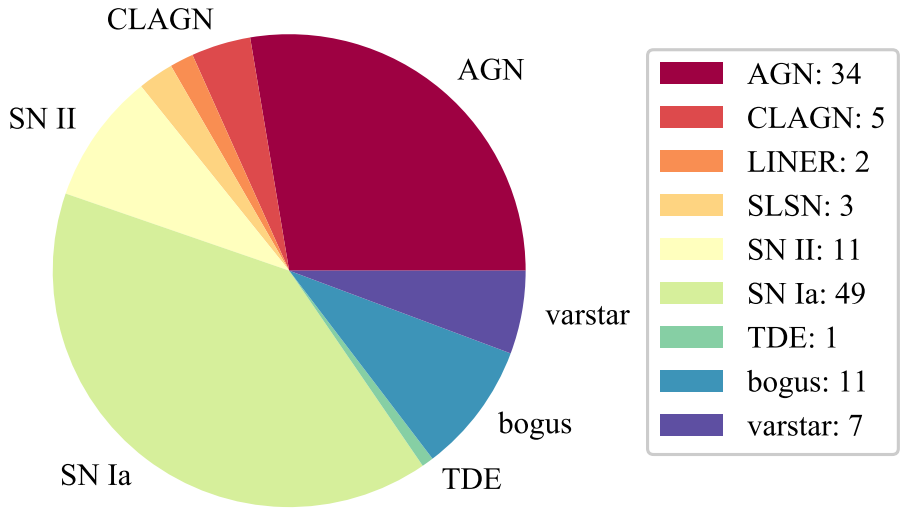

Figure 4.4: Pie chart that shows the composition of the subsample of nuclear transients that are classified with spectroscopy. We found 2 transients that have [OIII]/Hβ and [NII]/Hα line ratios consistent with low-ionization nuclear emission-line region (LINER), and 3 sources have been classified as superluminous supernovae (SLSNe).

4.4.1 Astrometry

At the beginning of the survey, we initially had a filter to remove any ZTF alert with a transient-host separation (`distnr`) of less than $0.8''$, which is an empirical value we derived in iPTF using cross-matched AGNs in the database. Whether this value is adequate was unknown since there has been several pipeline upgrade from iPTF to ZTF. In particular, the calibration of ZTF astrometry uses astrometric reference sources from the *Gaia* DR1 catalog (Gaia Collaboration et al. 2016) whereas the iPTF data were calibrated using reference from either the SDSS or the UCAC4 catalog (Masci et al. 2017).

We show the distribution of median offset of all detections for each source in our subsample in Figure 4.5. From this plot, we see most of the nuclear transients (AGNs) have a median offset of $< 0.5''$. Motivated by this improved accuracy in astrometric measurements, we decided to use a more stringent host separation cut ($< 0.5''$) to further filter out the non-nuclear transients (SNe) from May 16 2018.

4.4.2 Variability amplitude

We define the variability amplitude Δm_{var} as the PSF magnitude difference before and after the optical flare. The variablity amplitude can be calculated by

$$\Delta m_{var} = -2.5\log_{10}(10^{-\frac{m_{\rm PSF}}{2.5}} + 10^{-\frac{m_{\rm trans}}{2.5}}) - m_{\rm PSF}, \tag{4.1}$$

where $m_{\rm PSF}$ is the PSF magnitude of the host galaxy and $m_{\rm trans}$ is the host-subtracted transient magnitude. Δm_{var} is always negative by definition and can be thought of

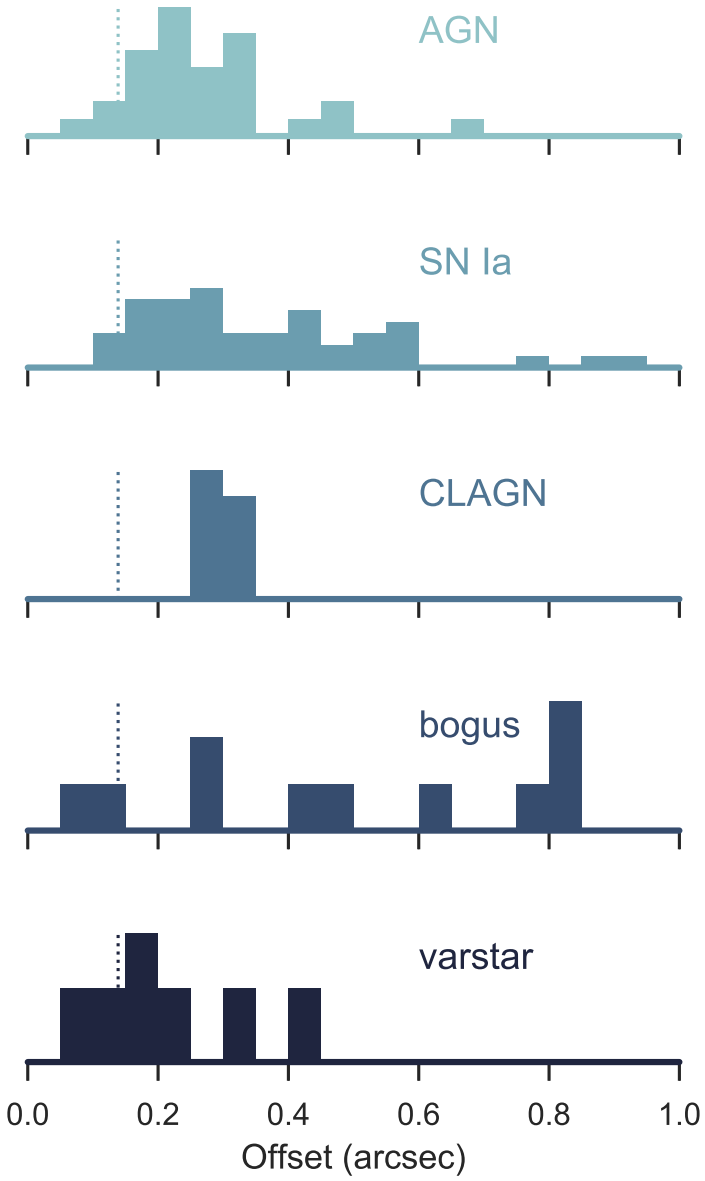

Figure 4.5: The normalized distribution of the median offset for different classes of objects. The offset cutoff has been reduced from 0.8″ from the start of ZTF commissioning to 0.5″ on May 16 2018. This lower threshold preserves most of the nuclear transients (AGNs) but would reject at least 50% more SN II and a fraction of the SN Ia. The dashed line marks the mean offset of AT2018zr, the first TDE detected in ZTF.

as the contrast between the flare and the host. The closer Δm_{var} is to 0, the less significant the variability is relative to its host.

Using the peak magnitude from ZTF light curves and PSF magnitude from PS1, we calculate Δm_{var} for each source in our subsample. We show the distribution of Δm_{var} for different types of object in Figure 4.6. The dotted line marks the Δm_{var} for TDE AT2018zr in the $R_{\rm PTF}$ band. It is noticed that AGNs, CLAGNs, and the galaxy core bogus have distributions that peak toward lower Δm_{var}. Prioritizing follow-up observations toward sources that have a $\Delta m_{var} < -0.5$ mag could help to avoid $\gtrsim 60\%$ of the nuclear activity and bogus events at the expense of finding low contrast TDEs, though none of the reported TDEs with well-sampled light curves fall in this regime.

4.4.3 Rise time

We calculate the rise time to peak (t_{rise}) for each source by taking the time difference between the light curve peak and the first detection of each source. Since AGN light curves are stochastic, the determination of t_{rise} can be difficult if there appear to be wiggles in the light curve.

The distribution of t_{rise} is shown in Figure 4.7. We see that almost all SN Ia have a rise time less than 20 days while the rise time for AGNs can range from the shortest to the longest baseline on a field. The light curves of AGNs could mimic that of a TDE, which has a typical rise time of $\gtrsim 40$ days. However, we may consider filtering on the "smoothness" of light curves to remove a fraction of AGNs whose

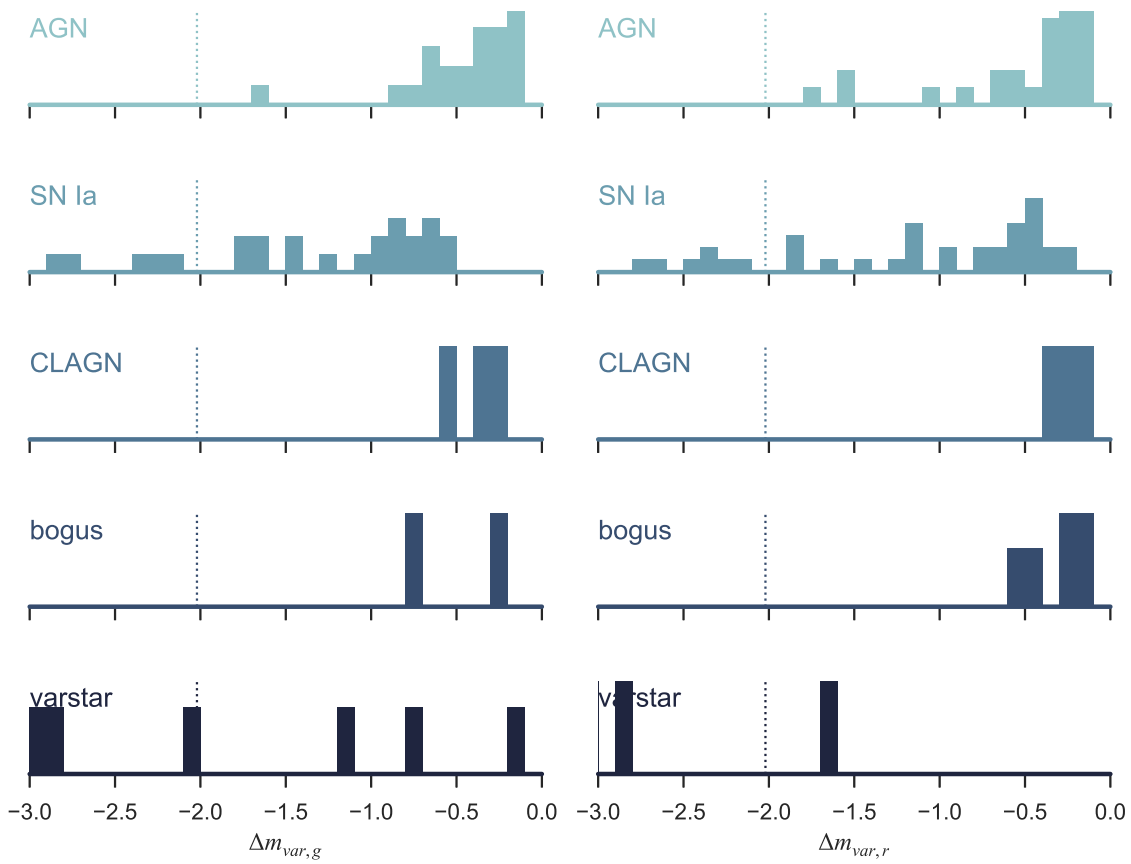

Figure 4.6: The distribution of Δm_{var} for different classes of objects in the subsample in $g_{\rm PTF}$ (left) and $R_{\rm PTF}$ (right) bands. The dotted line shows the Δm_{var} for AT2018zr in the $R_{\rm PTF}$ band.

light curves are not flare-like.

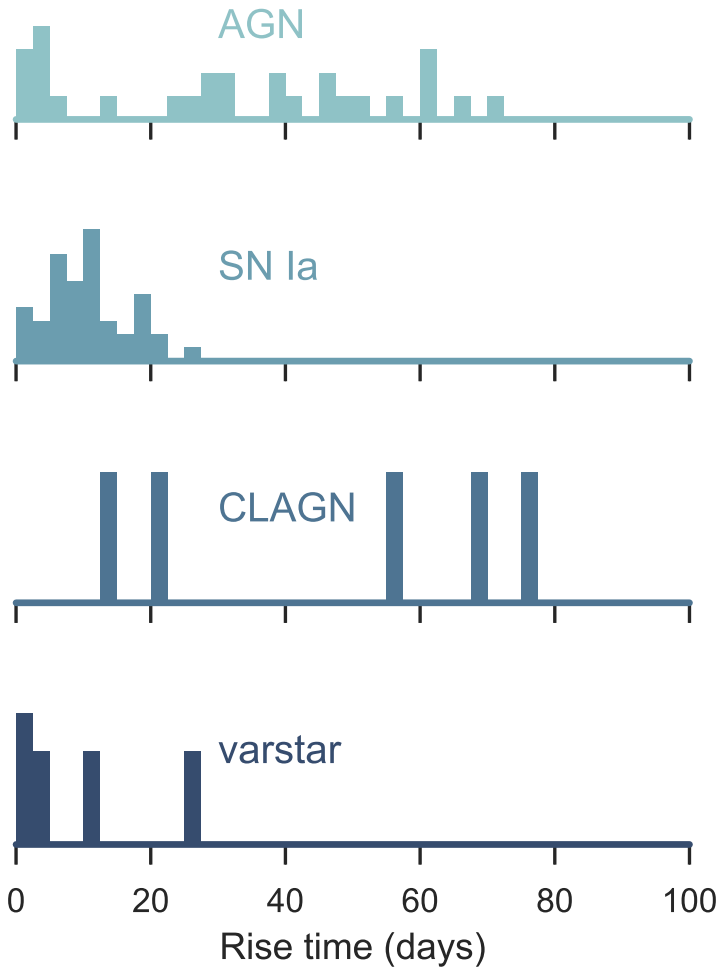

Figure 4.7: The rise time distribution for different classes of objects.

4.4.4 RB score

Since the ZTF `real-bogus` (RB) classifier is still a work in progress, our current selection criteria depend very little on the RB score. We note that the image differencing algorithm has changed from the IPAC pipeline (Masci et al. 2017) in iPTF to the ZOGY image differencing algorithm (Zackay et al. 2016) in

ZTF. Therefore, the ZTF RB classifier is trained with a different set of features from the iPTF days.

The RB classifier is trained on fresh ZTF data. Several versions of RB have already deployed since ZTF commissioning. The GROWTH Marshal scanning page is designed to record the sources saved and vetoed by its users. Each time when a new RB version is deployed, these labelled data will be collected to help fine-tuning the RB classifier. Some of the RB labels are contributed by citizen users through the ZTF MSIP zooniverse campaign[4]. We show the RB distribution of the latest RB model with version identifier $t8\_f5\_c3$ that was deployed on May 29, 2018 (Figure 4.8). This RB model is trained on data through May 7, 2018. The total distribution of RB ranges from 0.5 to 0.9 and is peaking toward the higher end. Although the RB distribution for these classes are overlapped, more bogus and variable stars are being scored lower than the extragalactic transients. Excluding sources with a RB score < 0.6 could help us get a cleaner sample, with less stars or subtraction artifacts. However, we currently do not consider placing any hard cutoff on the RB score in the GROWTH Marshal filter since the RB characteristics are still actively changing.

4.4.5 Unclassified sources

We break down the unclassified sources by several properties in Figure 4.9. Among the 344 unclassified sources, we found 15 sources in the Galactic plane ($|b| < 7$). However, a closer look at their pre-existing PS1 images revealed that

[4] `https://www.zooniverse.org/projects/rswcit/ztf-rb-project`

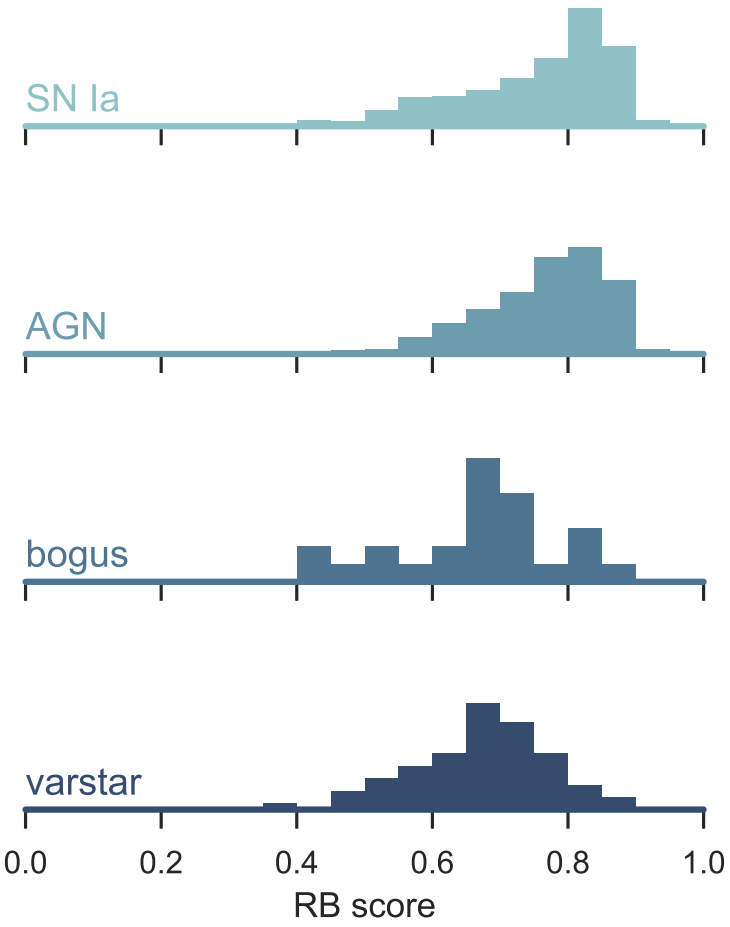

Figure 4.8: The density plots of RB score for different classes of objects.

many of these are blended double stars that were falsely interpreted as transients. For the Galactic plane sources, we define the source as a variable star if it has a $|\Delta m_{var}| > 0.8$. We found only two fifth (6/15) of these are stars that are variable (likely CV or M-dwarf flares) while the rest are due to subtraction on blended stars. We show examples of these blended stars in Figure 4.10. These are labeled as "blended" in Figure 4.9.

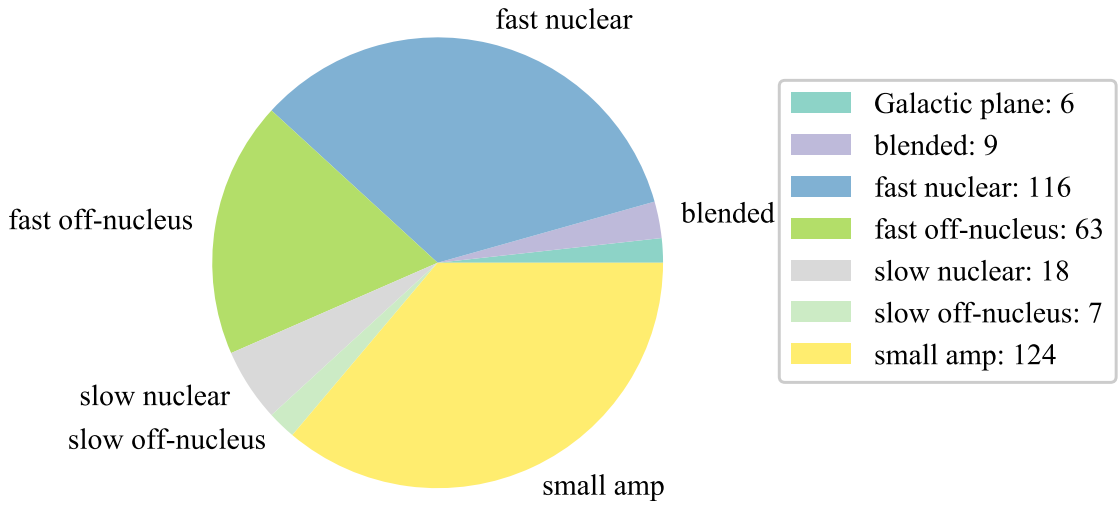

Figure 4.9: The composition of unclassified sources.

We then categorize the rest of the unclassified by its $|\Delta m_{\rm PSF}|$. Sources with $|\Delta m_{\rm PSF}| < 0.5$ have a smaller amplitude of variability relative to their host galaxies, we label them as "small amp" sources in Figure 4.9.

For the sources with larger amplitude of variability, we further separate them by their offset (d) from the galaxy nuclei. Sources with $d > 0.5''$ are labelled as "off-nucleus" while sources with $d \leq 0.5''$ are labelled as "nuclear". The nuclear and

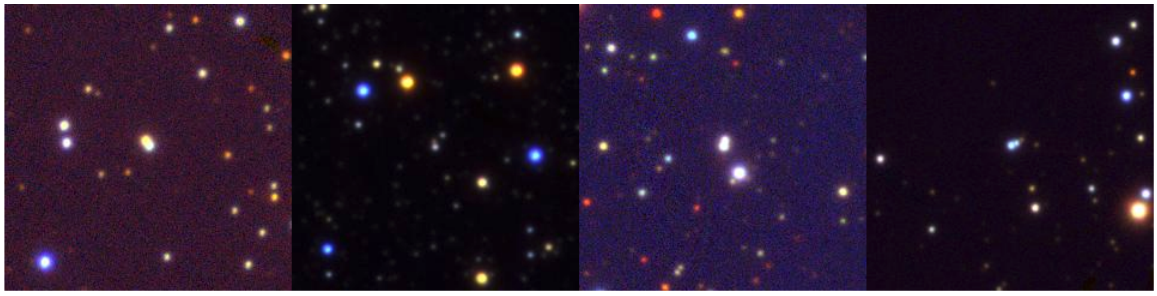

Figure 4.10: PS1 images centered on the blended stars that passed our filter due to limitations in the image subtraction. From left to right, these are the "hosts" of ZTF18aaawbgk, ZTF18aawcdxs, ZTF18aaxyqtj, and ZTF18aayhjya.

off-nuclear sources are then separated into "fast" and "slow" groups by comparing their rise time to peak with a threshold of 20 days.

4.4.6 Survey performance

The S/N threshold of ZTF alerts was decreased from 15 to 5 in 2018 March. To avoid confusion, the estimations in this section are only based on data after 2018 March. On average, ∼10 new ZTF nuclear events with extended host galaxies were saved per night. This number is derived excluding the nights when the MSIP survey was not conducted, due to reasons such as engineering. This implies a much lower space density of nuclear transients than our expectation from iPTF. Scaling directly from the nightly survey area, we estimated ZTF to discover ∼30 nuclear transients per night after accounting for the fraction of point-like sources (Hung et al. 2017b)

.

During this time, a few filter criteria have been modified. For example, the change in the offset cut from 0.8″ to 0.5″ is estimated to reduce the number of

transients by $\lesssim 20\%$. Yet this cannot fully account for the fact that we only found a total of 578 nuclear transients brighter than 20 mag in the 3 month-long ZTF survey since 2018 Apr while the expected number is > 1500 nuclear transients.

We have already found 1 TDE (AT2018zr) brighter than 19th mag in ZTF. If we consider a false-positive rate of 250:1 for nuclear candidates from iPTF, our findings are consistent given there should only be $\sim$2 TDEs among the 578 nuclear transients saved in the past 3 months.

From what can be concluded now, it seems like our photometric selection strategy is working. The main problem may lie at the earlier alert stream filtering stage. It will be important to investigate if any of our filter setup is preventing a great number of events from passing. This investigation is possible now the full alert stream has just become public in 2018 June.

4.5 Candidate Ranking

The ZTF MSIP survey has the capability of sampling the northern sky every 3 nights. For nuclear transients alone, the sources are saved at a rate of 10 events per night. The speed of spectroscopic classification, however, is much slower. Therefore, we have developed a robust ranking algorithm to help to determine which sources align better with our scientific goals.

Instead of applying a sharp cutoff on several parameters like we did for iPTF, here we use a sigmoid function to map the values of a parameter to probabilities.

Sigmoid function has the form

$$g(x) = \frac{1}{1 + e^{-\frac{x-\mu}{s}}}, \tag{4.2}$$

where x is a random variable, μ is the mean, and s is a proportional to the standard deviation (s = $\sqrt{3}\sigma/\pi$). The sigmoid function increases monotonically from 0 to 1. Since the TDE parameter spaces is still not fully probed, using a continuous probability distribution function allows us to include marginal candidates, which could be easily missed in a binary decision tree.

Using the offset (d) from the host centroid as an example (Figure 4.11), the probability of a source being a follow-up target decreases from p =0.5 to p =0 (don't follow-up) as d increases from 0.5″. The uncertainty in d controls the growth/decline rate $\frac{\Delta p}{\Delta d}$ in the sigmoid function (Figure 4.11). The larger the uncertainty, the slower the growth/decline rate.

We calculate the probabilities using both light curve properties and host galaxy properties. To summarize, the factors we have considered include

1. Separation d from the host centroid $< 0.5''$.
2. Host galaxy color from PS1 $g_{\rm PSF} - r_{\rm PSF} > 0.5$ mag.
3. $\Delta m_{var} > 0.5$ mag.
4. Transient color $g - r$ <0 mag.
5. Slope of the light curve (mag day^{-1}) > 0.
6. Rise time t_{rise} >20 days.

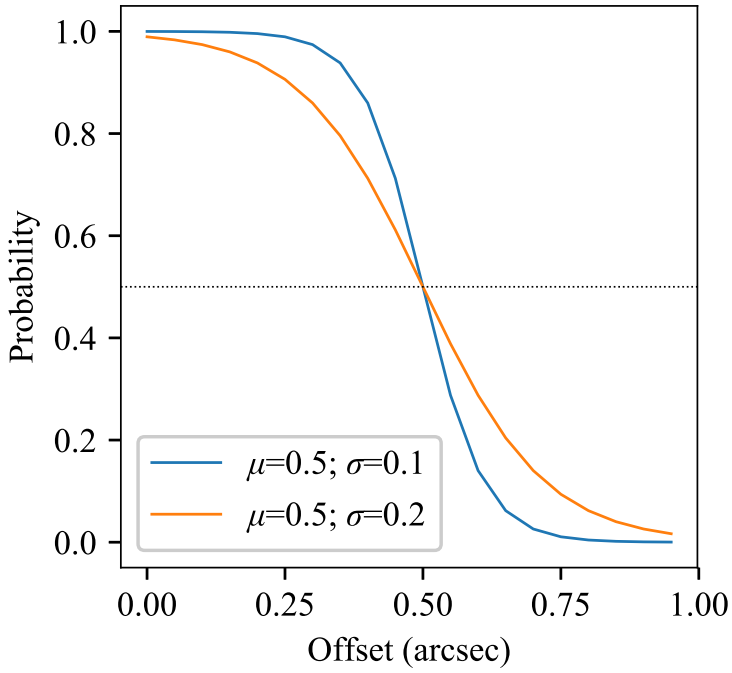

Figure 4.11: Sigmoid functions with μ=0.5 but different scale parameter s.

The first four parameters have been used in iPTF TDE candidate selection while the last two parameters are specific to ZTF. Even with better astrometry in ZTF, we still suffer from serious contamination from nuclear SN Ia. While we can achieve spectroscopic completeness with SED machine down to ∼18.5 mag for nuclear transients, we have to carefully curate sources between 18.5 <m< 20. Our strategy is to look for sources with a long rise time or wait until the transient is post maximum light, when the color in SN Ia starts to redden (e.g. Figure 4.12).

We grade each source by summing up the probabilities for these conditions with weights w =[3.0, 1.0, 2.0, 3.0, 1.0, 2.0]. Null values could appear when, for example, transient color $g-r$ is not available due to scheduling. The null values in these parameters, if present, are replaced with p =0.5. We run the ranking algorithm

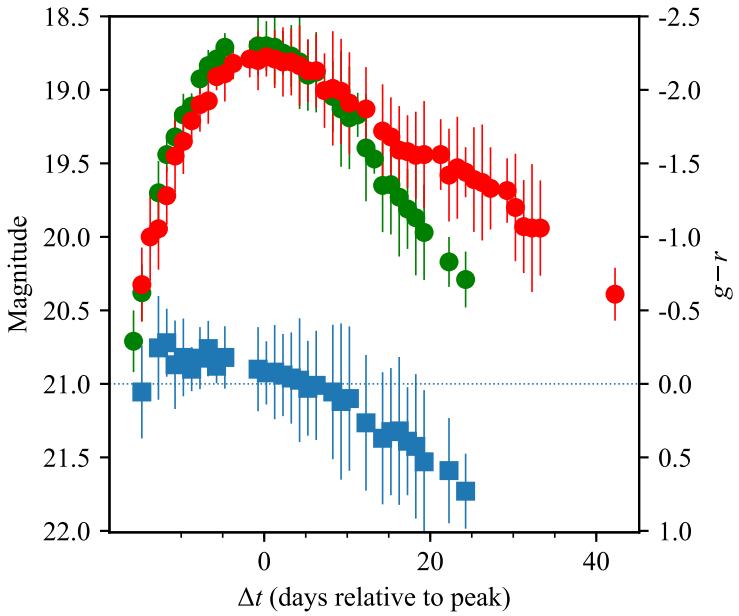

Figure 4.12: Light curves and $g-r$ color evolution of ZTF18aaxwjmp, a known SN Ia. The green and red dots are the ZTF light curves of ZTF18aaxwjmp in g and r bands, respectively. The blue squares show the $g-r$ colors from observations in the same nights. Many SN Ia have $g-r$ color evolution similar to this object, where $g-r$ remains negative until roughly 1 week post peak.

to generate a list of candidates for SEDm daily. The score calculation is only run on sources with a recent photometry observed within the past 24 hours that is brighter than 19th mag.

The first TDE seen by ZTF, AT2018zr, was deteced during the ZTF commissioning phase when same night $g-r$ was not available. However, this source would have passed most of the above criteria: it has a Δm_{var} of -2.2 mag, a host $g-r$ of 0.88 mag, and a separation of $0.11'' \pm 0.14''$.

4.6 The First ZTF TDE: AT2018zr

AT2018zr is a tidal disruption event discovered by Pan-STARRS1 on UT2018 Mar 02 (Tucker et al. 2018). The first ZTF alert on this source was independently generated at r =18.06 mag on UT2018 Mar 06. The source was flagged as a nuclear transient by our pipeline due to its small offset ($0.1''$) from the nucleus of the quiescent galaxy SDSS J075654.53+341543.6. Manual re-inspection of previous P48 images of the field obtained in early February suggest that the source was caught in an early rising phase, with r$\sim$21 mag at this time (van Velzen et al. in prep).

AT2018zr was bright in the UV before it became sun-constrained in early June. The UV/optical SEDs of this source can be fitted by a blackbody with a temperature of 1.8×10^4 K that varies little with time. Analyses on the broadband multi-wavelength (UV/optical/X-ray/radio) properties of this source will be submitted soon (van Velzen et al. in prep). UV and optical spectroscopy will be presented in a separate paper (Hung et al. in prep). Here, we present preliminary analysis on

the optical spectra of AT2018zr obtained from 2018 Apr to 2018 May.

4.6.1 Optical spectra

All the spectra presented here have been corrected for Milky Way extinction using the Schlafly & Finkbeiner (2011) dust map. Assuming a Cardelli et al. (1989) extinction curve with $R_{\rm C} = 3.1$, an E(B−V) of 0.0404±0.0006 at this position corresponds to a Galactic visual extinction ($A_{\rm V}$) of 0.124 mag.

We obtained a total of 13 optical spectra of AT2018zr. The observing configuration for each spectrum is detailed in Table 4.3. We compile a montage of the flux-calibrated spectra in Figure 4.13. The flux is normalized to the 5500 – 6000Å region in rest wavelength and offset from each other for better visualization.

4.7 Analysis

We identify the broad Hα and Hβ lines in these spectra, which are shown to have become stronger over time. Unlike some of the other TDEs (e.g. PS1-10jh Gezari et al. (2012)), there is no trace of broad HeIIλ4686 emission line at any of the observing epoch. This absence of HeIIλ4686 line resembles what was observed in the early optical spectra of ASASSN-14ae (Figure 3.12), which only developed a broad HeIIλ4686 line ∼4 months after discovery.

We perform spectral line fitting to the broad Hα and Hβ lines. In our initial attempt to fit these lines with a single gaussian function, we noticed that the line profiles of Hα and Hβ are more flat-topped than a gaussian and have asymmetric

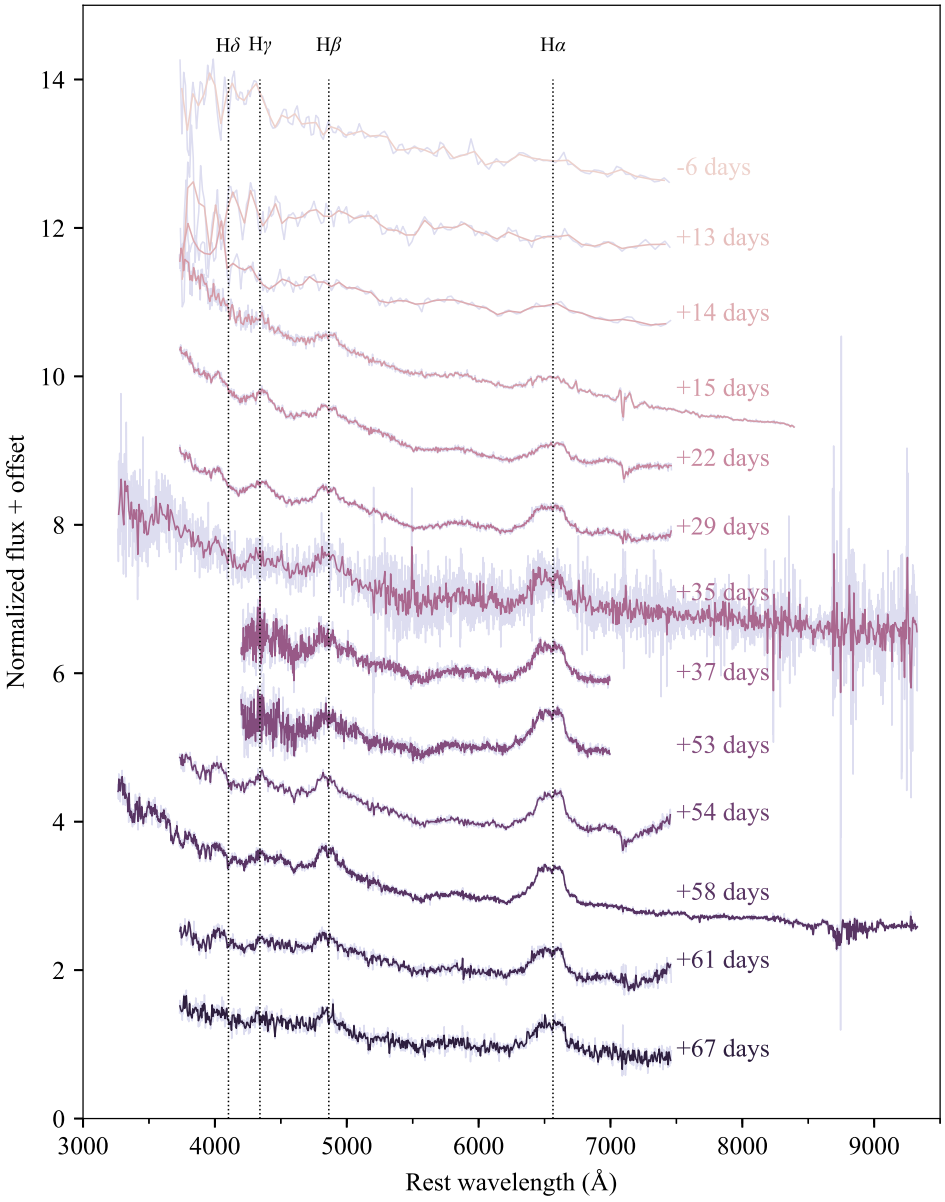

Figure 4.13: All 13 optical spectra of AT2018zr color coded by observation date. The telescope and instrument that each spectrum was taken with is listed in Table 4.3. The original data is plotted in pale grey under the smoothed spectra. All the spectra are smoothed with a binning factor of 3 except for the Apr 17 2018 Keck spectrum, which is binned every 5 pixels. The corresponding phase is indicated on the right of each spectrum.

wings (Figure 4.14). Therefore, we choose to fit each Balmer line simultaneously with two gaussians instead. We first normalize the region enclosing the lines (4630–5150 Å for Hβ and 5950–6950 Å for Hα) to the local continuum. The continuum is determined from fitting the region bracketing the line with a quadratic function. We then mask the pixels contaminated by stellar absorption with a 20Å-wide box. In the two-component fit, we allow the center, linewidth, and amplitude of the gaussian functions to vary freely. We show the zoom-in view on Hα and Hβ for each spectrum along with our fit in Figure 4.15. We also measure the equivalent width (EW) for both Hα and Hβ by integrating the normalized flux relative to the continuum along the wavelength. We present our best-fit parameters along with the equivalent width of the emission line in Table 4.4 and Table 4.5.

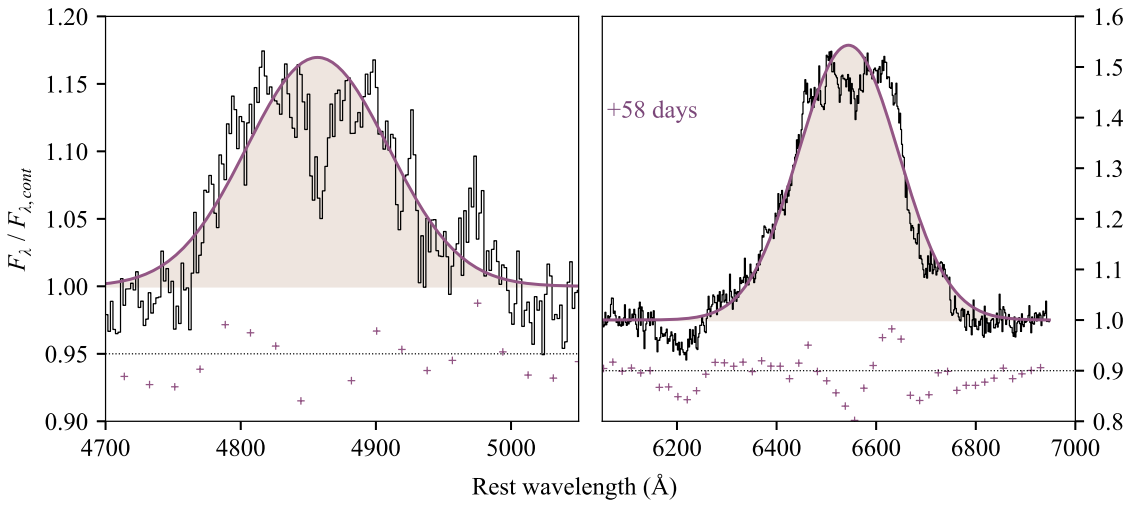

Figure 4.14: Single gaussian fit to Hα (right) and Hβ (left) with the May Keck LRIS spectrum. Residual is offset to the dotted line and is shown by the plus sign. Both lines show flat-topped profile that cannot be fitted well by a single gaussian. While the the red wing in Hβ seems less obvious, the blue wing in Hα is harder to dismiss.

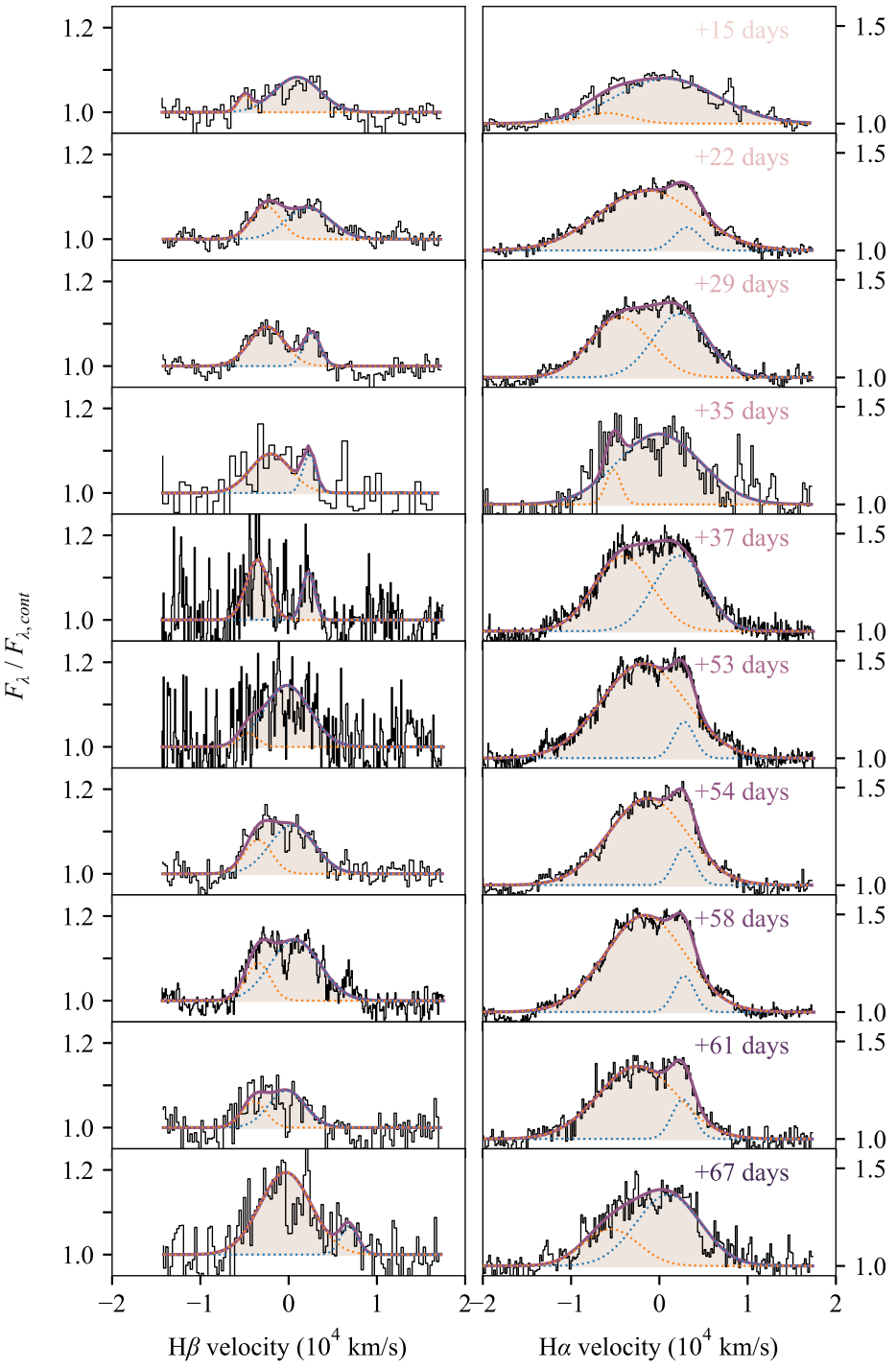

Figure 4.15: Zoom-in view on Hα and Hβ. The two-component fit has a total of 6 free parameters, which are listed in Table 4.4 and Table 4.5.

4.8 Discussion

4.8.1 Linewidth

In Figure 4.16, we show the full width at half-maximum (FWHM) of Hα and Hβ measured with the best-fit double-gaussian model. The linewidths of Hα and Hβ vary in the same trend and exhibit decline over time. AT2018zr has broad Balmer lines: its Hα line is comparable to ASASSN-14ae, and broader by a factor of $\sim$30% than the other TDEs. We noticed that the linewidth narrows over time for all the TDEs in Figure 4.16 (last epoch of iPTF16axa has low S/N), contrary to the behavior seen in the reverberation mapping of quasars (Holoien et al. 2016b).

4.8.2 Asymmetric wings

The asymmetry in Hα and Hβ becomes significant after the first epoch Δt=15 days. However, the line profiles of Hα and Hβ seem to skew toward different sides. The red peak in Hα appears more prominent while the blue peak is relatively stronger in Hα. We discuss a few possible scenarios that can produce line asymmetry. However, wavelength-dependent factors, such as extinction or contamination from neighboring lines, will be important to shape the opposite skewness in Hα and Hβ.

We first consider the flat-topped line profile to be caused by the orbital motion of a Keplerian disk. Double-peaked emission lines have been observed in many AGNs, which are believed to originate from the outer part of an accretion disk at

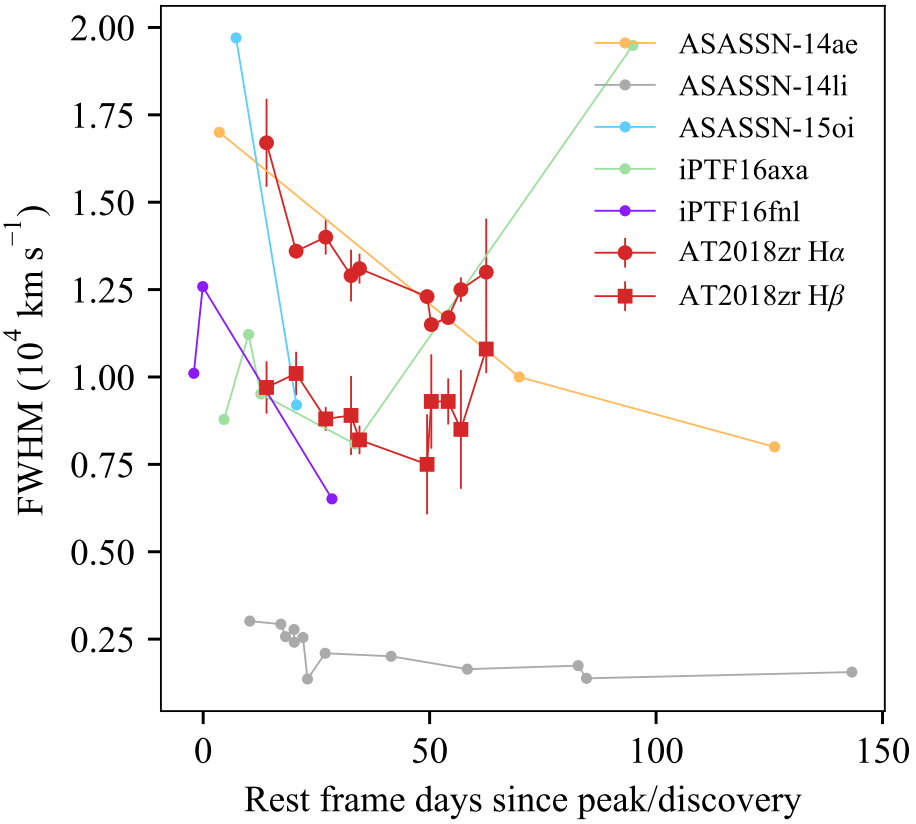

Figure 4.16: Evolution of the FWHM of Hα and Hβ for AT2018zr compared with the FWHM evolution of Hα of other well-studied TDEs. The linewidth of AT2018zr is similar to ASASSN-14ae and broader than the rest of the TDEs. The linewidths narrow with time like in other TDEs.

$\approx 1000 r_g$ (e.g. Chen et al. 1989; Eracleous & Halpern 1994; Strateva et al. 2003) illuminated by a central ionizing source. In addition to Doppler broadening, relativistic effects are incorporated to model the asymmetries seen in the double-peaked emission lines. For example, a circular relativistic disk model (Chen et al. 1989) is often employed to explain AGN spectra where the emission lines have a double-peaked shape with a stronger red peak. The opposite case in which the blue peak is stronger could be achieved with a elliptical disk (Eracleous et al. 1995).

In a recent paper by Liu et al. (2017), the authors fitted a Hα line with a second bump redshifted to 3.5×10^4 km s^{-1} in a TDE candidate, PTF09djl (Arcavi et al. 2014), with a highly eccentric elliptical disk with a large inclination angle (88 deg). Since The FWHM of Hα and Hβ in AT2018zr is small compared to PTF09djl, we should derive a moderate inclination angle when fitting the lines. We plan to perform line fitting with the elliptical disk model in (Eracleous et al. 1995) and compare the best-fit parameters with circularization characteristics.

Another scenario that can produce a blueshifted emission peak is when the line-emitting gas is outflowing. Roth & Kasen (2018) demonstrated that, optically thick TDE outflows can produce pure emission of Hα and HeIIλ4686 instead of a P-Cygni line profile due to the high excitation temperature of the lines. This scenario is plausible since radio observations in some TDEs have shown evidence of non-relativistic outflows (e.g. Alexander et al. 2016).

Table 4.1. Top-level ZTF alert contents

Field	Type	Contents
`schemavsn`	string	schema version used
`publisher`	string	origin of alert packet
`objectId`	long	unique identifier for this object
`candid`	long	unique identifier for the subtraction candidate
`candidate`	`ztf.alert.candidate`	candidate record
`prv_candidates`	array of `ztf.alert.prv_candidate` or null	candidate records for 30 days' past history
`cutoutScience`	`ztf.alert.cutout` or null	cutout of the science image
`cutoutTemplate`	`ztf.alert.cutout` or null	cutout of the coadded reference image
`cutoutDifference`	`ztf.alert.cutout` or null	cutout of the resulting difference image

Table 4.2. ZTF.alert.candidate schema

Field	Type	Contents
`jd`	double	Observation Julian date at start of exposure [days]
`fid`	int	Filter ID (1=g; 2=r; 3=i)
`pid`	long	Processing ID for image
`diffmaglim`	[float, null], default: null	5-sigma mag limit in difference image based on PSF-fit photometry [mag]
`pdiffimfilename`	[string, null], default: null	filename of positive (sci minus ref) difference image
`programpi`	[string, null], default: null	Principal investigator attached to program ID
`programid`	int	Program ID: encodes either public, collab, or caltech mode
`candid`	long	Candidate ID from operations DB
`isdiffpos`	string	t or 1: candidate is from positive (sci minus ref) subtraction;
		f or 0: candidate is from negative (ref minus sci) subtraction
`field`	[int, null], default: null	ZTF field ID
`xpos`	[float, null], default: null	x-image position of candidate [pixels]

Table 4.2 (cont'd)

Field	Type	Contents
ypos	[float, null], default: null	y-image position of candidate [pixels]
ra	double	Right Ascension of candidate; J2000 [deg]
dec	double	Declination of candidate; J2000 [deg]
magpsf	float	magnitude from PSF-fit photometry [mag]
sigmapsf	float	1-sigma uncertainty in magpsf [mag]
chipsf	[float, null], default: null	Reduced chi-square for PSF-fit
magap	[float, null], default: null	Aperture mag using 8 pixel diameter aperture [mag]
sigmagap	[float, null], default: null	1-sigma uncertainty in magap [mag]
distnr	[float, null], default: null	distance to nearest source in reference image PSF-catalog within 30 arcsec [pixels]
magnr	[float, null], default: null	magnitude of nearest source in reference image PSF-catalog within 30 arcsec [mag]
sigmagnr	[float, null], default: null	1-sigma uncertainty in magnr within 30 arcsec [mag]
		image PSF-catalog within 30 arcsec

Table 4.2 (cont'd)

Field	Type	Contents
		image PSF-catalog within 30 arcsec
sky	[float, null], default: null	Local sky background estimate [DN]
magdiff	[float, null], default: null	Difference: magap - magpsf [mag]
fwhm	[float, null], default: null	Full Width Half Max assuming a Gaussian core, from SExtractor [pixels]
rb	[float, null], default: null	RealBogus quality score; range is 0 to 1 where closer to 1 is more reliable
rbversion	string	version of RealBogus model/classifier used to assign rb quality score
		set to -999.0 if none [mag]
ranr	double	Right Ascension of nearest source in reference image PSF-catalog; J2000 [deg]
decnr	double	Declination of nearest source in reference image PSF-catalog; J2000 [deg]
objectidps1	[long, null], default: null	Object ID of closest source from PS1 catalog; if exists within 30 arcsec
sgmag1	[float, null], default: null	g-band PSF magnitude of closest source from PS1 catalog; if exists within 30 arcsec [mag]
srmag1	[float, null], default: null	r-band PSF magnitude of closest source from PS1 catalog; if exists within 30 arcsec [mag]

Table 4.2 (cont'd)

Field	Type	Contents
simag1	[float, null], default: null	i-band PSF magnitude of closest source from PS1 catalog; if exists within 30 arcsec [mag]
szmag1	[float, null], default: null	z-band PSF magnitude of closest source from PS1 catalog; if exists within 30 arcsec [mag]
sgscore1	[float, null], default: null	Star/Galaxy score of closest source from PS1 catalog 0<=sgscore<=1 where closer to 1 implies higher likelihood of being a star
distpsnr1	[float, null], default: null	Distance of closest source from PS1 catalog; if exists within 30 arcsec [arcsec]

Table 4.3. Observing details of the optical spectra of AT2018zr

Observation Date	Phase (days)	Telescope + Instrument	Slit Width	Grating	Exp Time (s)
2018-03-07	-6	P60 + SEDm	3.0″	none	900
2018-03-26	13	P60 + SEDm	3.0″	none	900
2018-03-27	14	P60 + SEDm	3.0″	none	900
2018-03-28	15	WHT + ACAM	1.0″	V400	1600
2018-04-04	22	DCT + DeVeny	1.5″	300g/mm	2400
2018-04-11	29	DCT + DeVeny	1.5″	300g/mm	2400
2018-04-17	35	Keck1 + LRIS	1.0″	400/3400+400/8500	1250
2018-04-19	37	Gemini + GMOS-N	1.0″	B600	600
2018-05-05	53	Gemini + GMOS-N	1.0″	B600	600
2018-05-06	54	DCT + DeVeny	1.5″	300g/mm	3000
2018-05-10	58	Keck1 + LRIS	1.0″	400/3400+400/8500	1250
2018-05-13	61	DCT + DeVeny	1.5″	300g/mm	1800

Table 4.3 (cont'd)

Observation Date	Phase (days)	Telescope + Instrument	Slit Width	Grating	Exp Time (s)
2018-05-19	67	DCT + DeVeny	1.5″	300g/mm	900

Table 4.4. Best-fit parameters of Hα for the optical spectra of AT2018zr

		Hα component 1			Hα component 2		
Phase (days)	Amplitude	x_0 ($\times 10^4$ kms^{-1})	FWHM ($\times 10^4$ kms^{-1})	Amp	x_0 ($\times 10^4$ kms^{-1})	FWHM ($\times 10^4$ kms^{-1})	EQW (Å)
15	0.23	0.08	1.35	0.05	-0.60	0.65	80
22	0.12	0.31	0.36	0.31	-0.14	1.31	103
29	0.33	0.23	0.72	0.31	-0.44	0.80	110
35	0.36	-0.01	1.10	0.18	-0.52	0.20	90
37	0.39	0.23	0.69	0.39	-0.41	0.77	128
53	0.19	0.28	0.28	0.48	-0.18	1.12	136
54	0.19	0.29	0.28	0.44	-0.13	1.04	115
58	0.18	0.28	0.28	0.50	-0.16	1.06	130
61	0.20	0.27	0.30	0.37	-0.25	1.05	101
67	0.37	0.10	0.86	0.19	-0.55	0.73	103

Table 4.5. Best-fit parameters of Hβ for the optical spectra of AT2018zr

		Hβ component 1			Hβ component 2		
Phase (days)	Amplitude	x_0 ($\times 10^4$ kms^{-1})	FWHM ($\times 10^4$ kms^{-1})	Amp	x_0 ($\times 10^4$ kms^{-1})	FWHM ($\times 10^4$ kms^{-1})	EQW (Å)
15	0.08	0.10	0.60	0.04	-0.50	0.17	6
22	0.07	0.22	0.59	0.08	-0.25	0.39	13
29	0.08	0.26	0.22	0.09	-0.25	0.47	8
35	0.10	0.23	0.16	0.09	-0.21	0.53	8
37	0.11	0.23	0.17	0.14	-0.35	0.30	9
53	0.15	-0.02	0.61	0.03	-0.46	0.25	15
54	0.11	0.04	0.59	0.08	-0.34	0.37	16
58	0.14	0.07	0.66	0.09	-0.35	0.32	19
61	0.09	-0.02	0.49	0.06	-0.39	0.33	6
67	0.07	0.68	0.23	0.19	-0.03	0.68	21

Chapter 5: Summary and Future Work

This thesis has explored the selection of TDEs in groud-based optical time domain surveys as well as the properties of optically-selected TDEs. We began by examining our systematic TDE selection strategy in a wide-area (4800 deg^2), $g + R$ iPTF experiment in Chapter 2, where we targeted typical optically-selected TDEs: bright (>60% ux increase) and blue transients residing in the center of red quiescent galaxies.

In our initial selection criteria, we have mined a sample of 26 candidates from a total of 493 nuclear transients. We then used follow-up UV imaging with the Neil Gehrels Swift Telescope, ground-based optical spectroscopy, and light curve fitting to classify them as 14 SNe Ia, 9 highly variable AGNs, 2 confirmed TDEs (iPTF16axa and iPTF16fnl), and 1 potential core-collapse supernova. We find it possible to filter AGNs by employing a more stringent transient color cut ($g - r < -0.2$ mag); further, UV imaging is the best discriminator for filtering SNe, since SNe Ia can appear as blue, optically, as TDEs in their early phases. However, when UV-optical color is unavailable, higher precision astrometry can also effectively reduce SNe contamination in the optical. Our most stringent optical photometric selection criteria yields a 4.5:1 contamination rate, allowing for a manageable number of TDE

candidates for complete spectroscopic follow-up and real-time classification in the ZTF era. We measure a TDE per galaxy rate of $1.7\ ^{+2.9}_{-1.3}\ \times 10^{-4}$ TDEs gal^{-1} yr^{-1} (90% CL in Poisson statistics).

In Chapter 3, we presented results from a multi-wavelength study of iPTF16axa, which is one of the two TDEs discovered in the iPTF experiment in Chapter 2. We estimated the luminosity, blackbody temperature, and photospheric radius of iPTF16axa from multi-epoch UV-optical SEDs and measured the time evolution of the broad HeII and Hα lines from its optical spectra.

We compared the photometric and spectroscopic properties of iPTF16axa with 11 other candidates in the literature (including iPTF16fnl) with well-sampled optical light curves. Based on a single-temperature fit to the optical and near-UV photometry, most of these TDE candidates have peak luminosities confined between log(L [erg s^{-1}]) = 43.4-44.4, with constant temperatures of a few $\times 10^4$ K during their power-law declines, implying blackbody radii on the order of ten times the tidal disruption radius, that decrease monotonically with time. For TDE candidates with hydrogen and helium emission, the high helium-to-hydrogen ratios suggest that the emission arises from high-density gas, where nebular arguments break down. We find no correlation between the peak luminosity and the black hole mass, contrary to the expectations for TDEs to have $\dot{M} \propto M_{\rm BH}^{-1/2}$.

Finally, we have investigated the data from the first 3 months of ZTF operation in Chapter 4. Using classification from spectroscopy and cross-matching to AGN catalogues, we re-examined our selection criteria for TDE candidates by comparing several parameter distributions for different transient types. We verified that using

a smaller host seperation cut (d <0.5″) can help remove SNe Ia while preserving most (>90%) of the nuclear transients. We also noticed that almost all SNe Ia have a rise-time of < 20 days, which is considerably shorter than that for TDEs ($t_{rise} \gtrsim$ 40 days).

We presented analysis on the optical spectra of AT2018zr, the first ZTF TDE discovered in 2018 March. We find that the emission line-profiles of AT2018zr are more flat-topped than gaussian. The linewidths are on the wider end among optically-selected TDEs, but are similar to that in ASASSN-14ae. The absence of HeII emission also resembles ASASSN-14ae in the early epochs.

5.1 Selection biases

The entire TDE population is still far from fully mapped. Therefore, the search presented in this work is not sensitive to TDEs with properties outside our selection criteria. First of all, our selection for "nuclear" transients prevented us from catching events near dwarf galaxies that could be hosting low-mass black holes. For example, a white dwarf can only be disrupted by black holes with $M_{\rm BH} < 10^5 M_\odot$ (MacLeod et al. 2016) and would have been missed by our selection.

Secondly, we applied selection on galaxy morphology, where all point-like sources, including stars and QSOs, were eliminated. Generally speaking, QSOs are at larger cosmological distances than AGNs in resolved galaxies and therefore we are biased against more luminous TDEs at higher redshift.

Thirdly, our selection on host galaxy color is biased against blue galaxies,

which are mostly made up of disk-dominated galaxies with ongoing star formation that do not follow a tight M–σ correlation like the bulge-dominated galaxies. We also eliminated galaxies with active nuclei and have missed transients like PS16dtm, which was found to have a higher accretion efficiency than most TDEs in quiescent galaxies (Blanchard et al. 2017).

Finally, our selection of high-contrast TDEs ($|\Delta m_{\rm PSF}| > 0.5$ mag) would have missed TDEs that are fainter relative to their host galaxies and the transient color cut ($g - r < 0$) could mask out TDEs that are highly extincted by dust.

5.2 Searching for TDEs with ZTF and LSST

The development of the optimal selection for TDE candidates in ZTF data is still an ongoing work. The main issue with the ZTF data is the short baseline (<3 months) in the construction of reference images, which could have caught transients in the references. Immediate consequences of this include having (1) off-nucleus supernovae falsely showing small separation from the host since the centroid is determined from the reference images and (2) slow transients like AGNs and TDEs getting deprioritized in follow-up observations by the Δm_{var} cut, or staying undetected if the reference images happened to capture the high-state. Fortunately, this problem will be alleviated as the survey moves along and gathers more data.

Going forward, we hope to achieve a more robust selection of TDEs by searching outside the parameter spaces defined in Chapter 2. By extending our search of TDEs toward all host galaxy types, we hope to uncover more subtypes of TDEs and

investigate whether there exists a correlation between TDE rate/properties, host galaxy properties (e.g. TDE rise time vs black hole mass), and accretion efficiency (L_{Edd}).

Meanwhile, it will be crucial to continue observing newly-discovered TDEs at all wavelengths. This is especially important in the UV since the energetics of optically-selected TDEs are dominated by their UV emission. In addition, multi-epoch UV spectroscopy will be the key to understanding the the kinematic structure and evolution as well as the ionization states in TDEs since more strong atomic transitions occur at UV wavelengths (e.g. C, N, Si...etc). Finally, in the era of LSST, survey depth is expected to reach $\sim$23 magnitude in a single exposure. Understanding the UV emission in TDEs will be important for identifying high-redshift TDEs observed by LSST.

Bibliography

Alexander, K. D., Berger, E., Guillochon, J., Zauderer, B. A., & Williams, P. K. G. 2016, ApJ, 819, L25

Arcavi, I., Gal-Yam, A., Sullivan, M., et al. 2014, ApJ, 793, 38

Bade, N., Komossa, S., & Dahlem, M. 1996, A&A, 309, L35

Blagorodnova, N., Gezari, S., Hung, T., et al. 2017a, ApJ, 844, 46

Blagorodnova, N., Neill, J. D., Walters, R., et al. 2017b, ArXiv e-prints, arXiv:1710.02917

Blanchard, P. K., Nicholl, M., Berger, E., et al. 2017, ApJ, 843, 106

Blanton, M. R., Dalcanton, J., Eisenstein, D., et al. 2001, AJ, 121, 2358

Blondin, S., & Tonry, J. L. 2007, ApJ, 666, 1024

Bloom, J. S., Giannios, D., Metzger, B. D., et al. 2011, Science, 333, 203

Bogdanović, T., Eracleous, M., Mahadevan, S., Sigurdsson, S., & Laguna, P. 2004, ApJ, 610, 707

Bonnerot, C., Rossi, E. M., & Lodato, G. 2017, MNRAS, 464, 2816

Brandt, W. N., Pounds, K. A., & Fink, H. 1995, MNRAS, 273, L47

Bruzual, G., & Charlot, S. 2003, MNRAS, 344, 1000

Burrows, D. N., Hill, J. E., Nousek, J. A., et al. 2005, Space Sci. Rev., 120, 165

Burrows, D. N., Kennea, J. A., Ghisellini, G., et al. 2011, Nature, 476, 421

Cao, Y., Nugent, P. E., & Kasliwal, M. M. 2016, PASP, 128, 114502

Cappellari, M. 2017, MNRAS, 466, 798

Cardelli, J. A., Clayton, G. C., & Mathis, J. S. 1989, ApJ, 345, 245

Chen, K., Halpern, J. P., & Filippenko, A. V. 1989, ApJ, 339, 742

Chornock, R., Berger, E., Gezari, S., et al. 2014, ApJ, 780, 44

Cid Fernandes, R., Stasińska, G., Schlickmann, M. S., et al. 2010, MNRAS, 403, 1036

Cutri, R. M., & et al. 2013, VizieR Online Data Catalog, 2328

Dai, L., McKinney, J. C., & Miller, M. C. 2015, ApJ, 812, L39

Dilday, B., Smith, M., Bassett, B., et al. 2010, ApJ, 713, 1026

Dong, S., Shappee, B. J., Prieto, J. L., et al. 2016, Science, 351, 257

Donley, J. L., Brandt, W. N., Eracleous, M., & Boller, T. 2002, AJ, 124, 1308

Drake, A. J., Djorgovski, S. G., Mahabal, A., et al. 2011, ApJ, 735, 106

Drout, M. R., Chornock, R., Soderberg, A. M., et al. 2014, ApJ, 794, 23

Eracleous, M., & Halpern, J. P. 1994, ApJS, 90, 1

Eracleous, M., Livio, M., Halpern, J. P., & Storchi-Bergmann, T. 1995, ApJ, 438, 610

Esquej, P., Saxton, R. D., Freyberg, M. J., et al. 2007, A&A, 462, L49

Esquej, P., Saxton, R. D., Komossa, S., et al. 2008, A&A, 489, 543

Evans, C. R., & Kochanek, C. S. 1989, ApJ, 346, L13

Evans, P. A., Beardmore, A. P., Page, K. L., et al. 2009, MNRAS, 397, 1177

Flesch, E. W. 2017, VizieR Online Data Catalog, 7277

Foreman-Mackey, D., Hogg, D. W., Lang, D., & Goodman, J. 2013, PASP, 125, 306

Fremling, C., Sollerman, J., Taddia, F., et al. 2016, A&A, 593, A68

French, K. D., Arcavi, I., & Zabludoff, A. 2016, ApJ, 818, L21

Frohmaier, C., Sullivan, M., Nugent, P. E., Goldstein, D. A., & DeRose, J. 2017, ApJS, 230, 4

Gaia Collaboration, Brown, A. G. A., Vallenari, A., et al. 2016, A&A, 595, A2

Gaskell, C. M., & Rojas Lobos, P. A. 2014, MNRAS, 438, L36

Gehrels, N., Chincarini, G., Giommi, P., et al. 2004, ApJ, 611, 1005

Gezari, S., Cenko, S. B., & Arcavi, I. 2017a, ApJ, 851, L47

Gezari, S., Chornock, R., Lawrence, A., et al. 2015, ApJ, 815, L5

Gezari, S., Basa, S., Martin, D. C., et al. 2008, ApJ, 676, 944

Gezari, S., Heckman, T., Cenko, S. B., et al. 2009, ApJ, 698, 1367

Gezari, S., Chornock, R., Rest, A., et al. 2012, Nature, 485, 217

Gezari, S., Hung, T., Cenko, S. B., et al. 2017b, ApJ, 835, 144

—. 2017c, ApJ, 835, 144

Graur, O., French, K. D., Zahid, H. J., et al. 2017, ArXiv e-prints, arXiv:1707.02986

Greiner, J., Schwarz, R., Zharikov, S., & Orio, M. 2000, A&A, 362, L25

Grupe, D., Beuermann, K., Mannheim, K., et al. 1995, A&A, 299, L5

Guillochon, J., Manukian, H., & Ramirez-Ruiz, E. 2014, ApJ, 783, 23

Guillochon, J., & Ramirez-Ruiz, E. 2013, ApJ, 767, 25

Hao, L., Strauss, M. A., Tremonti, C. A., et al. 2005, AJ, 129, 1783

Hills, J. G. 1975, Nature, 254, 295

Holoien, T. W.-S., Prieto, J. L., Bersier, D., et al. 2014, MNRAS, 445, 3263

Holoien, T. W.-S., Kochanek, C. S., Prieto, J. L., et al. 2016a, ArXiv e-prints, arXiv:1602.01088

—. 2016b, MNRAS, 455, 2918

Hook, I. M., McMahon, R. G., Boyle, B. J., & Irwin, M. J. 1994, MNRAS, 268, 305

Hung, T., Gezari, S., Jones, D. O., et al. 2016, ApJ, 833, 226

Hung, T., Gezari, S., Blagorodnova, N., et al. 2017a, ApJ, 842, 29

Hung, T., Gezari, S., Cenko, S. B., et al. 2017b, ArXiv e-prints, arXiv:1712.04936

Jiang, Y.-F., Guillochon, J., & Loeb, A. 2016, ApJ, 830, 125

Kauffmann, G., Heckman, T. M., Tremonti, C., et al. 2003, MNRAS, 346, 1055

Kelly, P. L., & Kirshner, R. P. 2012, ApJ, 759, 107

Kewley, L. J., Dopita, M. A., Sutherland, R. S., Heisler, C. A., & Trevena, J. 2001, ApJ, 556, 121

Kochanek, C. S. 1994, ApJ, 422, 508

Komossa, S. 2015, Journal of High Energy Astrophysics, 7, 148

Komossa, S., & Bade, N. 1999, A&A, 343, 775

Komossa, S., & Greiner, J. 1999, A&A, 349, L45

Kriek, M., van Dokkum, P. G., Labbé, I., et al. 2009, ApJ, 700, 221

Kumar, S., Gezari, S., Heinis, S., et al. 2015, ApJ, 802, 27

Laher, R. R., Surace, J., Grillmair, C. J., et al. 2014, PASP, 126, 674

LaMassa, S. M., Cales, S., Moran, E. C., et al. 2015, ApJ, 800, 144

Law-Smith, J., MacLeod, M., Guillochon, J., Macias, P., & Ramirez-Ruiz, E. 2017a, ApJ, 841, 132

Law-Smith, J., Ramirez-Ruiz, E., Ellison, S. L., & Foley, R. J. 2017b, ArXiv e-prints, arXiv:1707.01559

Leloudas, G., Fraser, M., Stone, N. C., et al. 2016, Nature Astronomy, 1, 0002

Levan, A. J., Tanvir, N. R., Cenko, S. B., et al. 2011, Science, 333, 199

Liu, F. K., Zhou, Z. Q., Cao, R., Ho, L. C., & Komossa, S. 2017, MNRAS, 472, L99

Lodato, G., King, A. R., & Pringle, J. E. 2009, MNRAS, 392, 332

Lodato, G., & Rossi, E. M. 2011, MNRAS, 410, 359

Loeb, A., & Ulmer, A. 1997, ApJ, 489, 573

MacLeod, C. L., Ross, N. P., Lawrence, A., et al. 2016, MNRAS, 457, 389

Magorrian, J., & Tremaine, S. 1999, MNRAS, 309, 447

Masci, F. J., Laher, R. R., Rebbapragada, U. D., et al. 2017, PASP, 129, 014002

McConnell, N. J., & Ma, C.-P. 2013, ApJ, 764, 184

McElroy, R. E., Husemann, B., Croom, S. M., et al. 2016, A&A, 593, L8

Metzger, B. D., & Stone, N. C. 2016, MNRAS, 461, 948

Miller, A. A., Kasliwal, M. M., Cao, Y., et al. 2017, ApJ, 848, 59

Miller, M. C. 2015, ApJ, 805, 83

Oke, J. B., Cohen, J. G., Carr, M., et al. 1994, in Proc. SPIE, Vol. 2198, Instrumentation in Astronomy VIII, ed. D. L. Crawford & E. R. Craine, 178–184

Pereyra, N. A., Vanden Berk, D. E., Turnshek, D. A., et al. 2006, ApJ, 642, 87

Phillips, M. M. 1993, ApJ, 413, L105

Phinney, E. S. 1989, in IAU Symposium, Vol. 136, The Center of the Galaxy, ed. M. Morris, 543

Piran, T., Svirski, G., Krolik, J., Cheng, R. M., & Shiokawa, H. 2015, ApJ, 806, 164

Rees, M. J. 1988, Nature, 333, 523

Roming, P. W. A., Kennedy, T. E., Mason, K. O., et al. 2005, Space Sci. Rev., 120, 95

Roth, N., & Kasen, D. 2018, ApJ, 855, 54

Roth, N., Kasen, D., Guillochon, J., & Ramirez-Ruiz, E. 2016, ApJ, 827, 3

Ruan, J. J., Anderson, S. F., Cales, S. L., et al. 2016, ApJ, 826, 188

Saxton, C. J., Perets, H. B., & Baskin, A. 2016, ArXiv e-prints, arXiv:1612.08093

Saxton, R. D., Read, A. M., Esquej, P., et al. 2012, A&A, 541, A106

Schlafly, E. F., & Finkbeiner, D. P. 2011, ApJ, 737, 103

Serenelli, A. M., & Basu, S. 2010, ApJ, 719, 865

Sesar, B., Ivezić, Ž., Lupton, R. H., et al. 2007, AJ, 134, 2236

Shappee, B. J., Prieto, J. L., Grupe, D., et al. 2014, ApJ, 788, 48

Shiokawa, H., Krolik, J. H., Cheng, R. M., Piran, T., & Noble, S. C. 2015, ApJ, 804, 85

Stern, D., Assef, R. J., Benford, D. J., et al. 2012, ApJ, 753, 30

Stone, N. C., & Metzger, B. D. 2016, MNRAS, 455, 859

Stone, N. C., & van Velzen, S. 2016, ApJ, 825, L14

Strateva, I. V., Strauss, M. A., Hao, L., et al. 2003, AJ, 126, 1720

Strubbe, L. E., & Murray, N. 2015, MNRAS, 454, 2321

Strubbe, L. E., & Quataert, E. 2009, MNRAS, 400, 2070

Svirski, G., Piran, T., & Krolik, J. 2017, MNRAS, doi:10.1093/mnras/stx117

Tucker, M. A., Huber, M., Shappee, B. J., et al. 2018, The Astronomer's Telegram, 11473

Tundo, E., Bernardi, M., Hyde, J. B., Sheth, R. K., & Pizzella, A. 2007, ApJ, 663, 53

Ulmer, A. 1999, ApJ, 514, 180

van Velzen, S. 2017, ArXiv e-prints, arXiv:1707.03458

van Velzen, S., & Farrar, G. R. 2014, ApJ, 792, 53

van Velzen, S., Mendez, A. J., Krolik, J. H., & Gorjian, V. 2016a, ApJ, 829, 19

van Velzen, S., Farrar, G. R., Gezari, S., et al. 2011, ApJ, 741, 73

van Velzen, S., Anderson, G. E., Stone, N. C., et al. 2016b, Science, 351, 62

Vanden Berk, D. E., Wilhite, B. C., Kron, R. G., et al. 2004, ApJ, 601, 692

Véron-Cetty, M.-P., & Véron, P. 2010, A&A, 518, A10

Wang, J., & Merritt, D. 2004, ApJ, 600, 149

Wilhite, B. C., Vanden Berk, D. E., Kron, R. G., et al. 2005, ApJ, 633, 638

Wyrzykowski, Ł., Zieliński, M., Kostrzewa-Rutkowska, Z., et al. 2016, ArXiv e-prints, arXiv:1606.03125

Yaron, O., & Gal-Yam, A. 2012, PASP, 124, 668

Zackay, B., Ofek, E. O., & Gal-Yam, A. 2016, ApJ, 830, 27

Zauderer, B. A., Berger, E., Soderberg, A. M., et al. 2011, Nature, 476, 425